Beyond Mean-field Dynamics in Closed and Open Bosonic Systems

A dissertation

by

M.Sc. Georgios Kordas

December 2013

Dissertation

submitted to the

Combined Faculties of Natural Sciences and Mathematics

of the Ruperto-Carola-University of Heidelberg, Germany

and the

Department of Physics

of the National and Kapodistrian University of Athens, Greece

Put forward by

M.Sc. Georgios Kordas

born in: Athens, Greece

Oral examination: 5. December 2013

Beyond Mean-Field Dynamics in Closed and Open Bosonic Systems

Referees: PD Dr. Sandro Wimberger
As. Prof. Dr. Alexandros Karanikas

Περίληψη

Η παρούσα διδακτορική διατριβή πραγματεύεται τη μελέτη της δυναμικής ανοικτών ή κλειστών μποζονικών συστημάτων πολλών σωμάτων, με τη χρήση μεθόδων πέραν της προσέγγισης μέσου πεδίου.

Στο πρώτο μέρος, εμπνεόμαστε από τα πειράματα αιχμής και μελετάμε τη δυναμική ενός συμπυκνώματος Bose-Einstein παγιδευμένο σε ένα οπτικό πλέγμα που υπόκεινται σε εντοπισμένες απώλειες μεμονωμένων ατόμων. Αποδεικνύεται ότι οι συγκεκριμένου τύπου απώλειες μπορούν να μας βοηθήσουν να ελέγξουμε τη δυναμική πολλών σωμάτων, αφού επιτρέπουν τον τοπικό έλεγχο της συνεκτικότητας του συστήματος και δημιουργούν ελκτικά σημεία στον κλασσικό χώρο φάσεων. Χρησιμοποιούμαι αυτό το μηχανισμό για να δημιουργήσουμε εντοπισμένες μη γραμμικές δομές όπως φωτεινά και σκοτεινά διακριτά σολιτόνια. Επιπλέον, για συγκεκριμένες αρχικές καταστάσεις, το σύστημα παράγει εναγκαλισμένες μακρόβιες καταστάσεις, εξαιρετικής σημασίας για πρακτικές εφαρμογές. Το πρώτο μέρος τελειώνει με τη μελέτη της εκτός ισορροπίας μεταφοράς μποζονίων σε ένα οπτικό πλέγμα.

Στο δεύτερο μέρος παρουσιάζουμε τεχνικές ολοκληρωμάτων διαδρομών που επιτρέπουν τη μελέτη μποζονικών συστημάτων. Αναλύουμε το φαινόμενο της συμπύκνωσης Bose-Einstein χρησιμοποιώντας εργαλεία από την κβαντική θεωρία πεδίου και τη θεωρία της κβαντικής πληροφορίας. Η εργασία καταλήγει με την εισαγωγή ενός φορμαλισμού ολοκληρωμάτων διαδρομών συνεκτικών καταστάσεων στο συνεχές που επιτρέπει τη συστηματική ανάπτυξη προσεγγιστικών μεθόδων για τη μελέτη μποζονίων παγιδευμένων σε οπτικά πλέγματα.

Zusammenfassung

Diese Arbeit widmet sich der Dynamik in offenen und geschlossenen bosonschen Vielteilchensystemen. Dabei werden Methoden benutzt, die über die Molekularfeldnäherung hinausgehen.

Im ersten Teil untersuchen wir – angeregt durch aktuelle Experimente – die Dynamik eines Bose-Einstein-Kondensates in einem optischen Gitter mit lokalen Verlustkanälen für die Atome. Wir zeigen, dass unsere spezielle Form der Dissipation helfen kann, die Vielteilchendynamik zu kontrollieren. Sie erlaubt die lokale Manipulierung der Kohärenzeigenschaften des Systems und erzeugt attraktive Fixpunkte im klassischen Phasenraum (der durch die Molekularfeldnäherung festgelegt wird). Wir sagen die dynamische Erzeugung stabiler nichtlinearer Strukturen vorher, wie zum Beispiel diskreter heller und dunkler Solitonen. Für bestimmte Anfangszustände geht das System ferner in hochverschränkte und langlebige Zustände über, die für die Anwendung von großer Relevanz sind. Der erste Teil der Arbeit endet mit der Untersuchung des Nichtgleichwichtstransports von Bosonen über optische eindimensionale Gitter.

Im zweiten Teil präsentieren wir Methoden zur Beschreibung von bosonschen Vielteichensystemen, die auf Pfadintegralen basieren. Wir analysieren das Phänomen der Bose-Kondensation mittels Handswerkzeugen aus der Quanteninformationstheorie und der Feldtheorie. Zu guter Letzt führen wir einen Pfadintegralformalismus im Kontinuum ein, der uns die systematische Entwicklung von Näherungsmethoden für Bosonen in optischen Gittern erlaubt.

Abstract

The present thesis is devoted to the dynamics in open or closed many-body bosonic systems, with the use of beyond mean-field methods.

In the first part, inspired by the state-of-the-art experiments, we study the dynamics of a Bose-Einstein condensation which is loaded in an optical lattice with localized loss channels for the atoms. We prove that the particular form of the dissipation can help us to control the many-body dynamics. The loss allows the local manipulation of the system's coherence properties and creates attractive fixed points in the classical (mean-field) phase space. We predict the dynamical creation of stable nonlinear structures like discrete bright and dark solitons. Furthermore, for specific initial states, the systems produces highly entangled and long-living states, which are of high relevance for practical applications. The first part of this thesis ends with the study of non-equilibrium bosonic transport across optical one-dimensional lattices.

In the second part, we present techniques for bosonic many-body systems which are based on path integrals. We analyze the Bose-Einstein condensation phenomenon by using tools from quantum information theory and field theory. Finally, we introduce a coherent state path integral formalism in the continuum, which allows us the systematic development of approximate methods for the study of bosons in optical lattices.

Contents

Chapter 1

Introduction

This introductory chapter is mainly a review of the theory and the experiments pertaining the Bose-Einstein condensation and ultracold atoms in optical lattices. The Bose-Einstein condensation (or BEC) phenomenon is explained in section 1.1 for an ideal bosonic gas. Furthermore we discuss some important approximations for the theoretical description of BECs in the presence of interparticle interactions. In section 1.2 we briefly review the experimental techniques to prepare and manipulate BECs. Section 1.3 gives some important results about the physics in periodic potentials and we further introduce the Bose-Hubbard model. Open bosonic systems will be the subject of the main part of this thesis, so in the last section we present the so-called Master equation formalism. For more details about the topics covered in this chapter can be found in [4, 17, 18] and [22, 23].

1.1 Bose-Einstein Condensation

In this section we present a brief introduction to the Bose-Einstein condensation phenomenon. First we introduce the phenomenon using an ideal gas of bosons and then we discuss what happens in the presence of interparticle interactions. Finally, we give a general definition of the Bose-Einstein condensation by introducing the so-called single particle density matrix.

1.1.1 Condensation of an Ideal Gas of Bosons in a Box

The phenomenon of Bose-Einstein condensation was already known since 1924-1925, when it was predicted by Bose [1] and Einstein [2]. Let us present this phenomenon for a simple model system: a gas of N non-interacting bosons in a three-dimensional box of volume $V = L^3$. In this case, due to

the boundary conditions, the single particle energy is quantized

$$\varepsilon_k = \frac{\hbar^2 \vec{k}^2}{2m},\tag{1.1}$$

where

$$\vec{k} = \frac{2\pi}{L}\vec{n}, \ \ \vec{n} \in \mathbb{Z}^3,\tag{1.2}$$

and m is the mass of the particle. In the grand canonical ensemble, the occupation number of a quantum state with wave-number $\vec{k}$ is given by

$$N_k = \frac{1}{e^{\beta(\varepsilon_k - \mu)} - 1},\tag{1.3}$$

where $\beta = 1/k_B T$ is the inverse temperature. To assure the convergence in the derivation of the equation (1.3), the chemical potential must be zero or negative, $\mu \leq 0$. This also, assures that the occupation number cannot be negative. Now, the total particle number is obtained by summing (1.3) over all $\vec{k}$:

$$N = \sum_{\vec{k}} \frac{1}{e^{\beta(\varepsilon_k - \mu)} - 1}.\tag{1.4}$$

In order to perform the sum in the above equation, we wish to replace the sum over $\vec{k}$ with an integral over $\vec{k}$, namely:

$$\sum_{\vec{k}} f_{\vec{k}} = V \int \frac{d^3 k}{(2\pi)^3} f_{\vec{k}}.\tag{1.5}$$

This replacement assumes that the function $f_{\vec{k}}$ is a smooth function of $\vec{k}$. If the replacement of the sum by the integral is valid, then the integral over $\vec{k}$ can be transformed to an integral over energy using the definition of the density of states. In the case of the spherically symmetric relation between the single particle energy ε_k, such as (1.1), the density of states can be calculated from the equation

$$V \frac{d^3}{(2\pi)^3} = g(\varepsilon) d\varepsilon.\tag{1.6}$$

It is, now, easy to find that

$$g(\varepsilon) = \frac{2\pi V}{h^3} (2m)^{3/2} \sqrt{\varepsilon}.\tag{1.7}$$
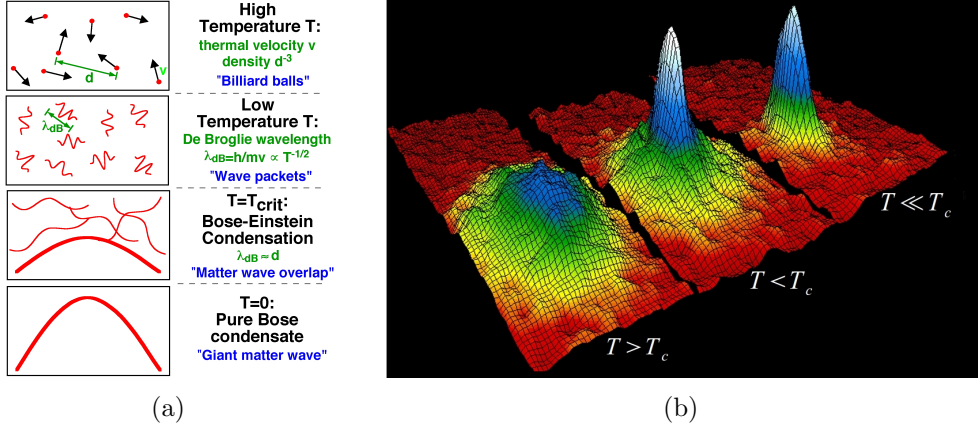
Figure 1.1: (a) *Schematic illustration of BEC. Reprinted figure with permission from* [7]. *Copyright (2002) by the American Physical Society.* (b) *Velocity distribution of the first BEC* [8, 10]. *The left frame shows the velocity distribution just before the appearance of the BEC ; the center frame, just after the appearance of the condensate; the right frame, after further cooling we have a sample of nearly pure condensate.*

However, the above approximation is not entirely correct, since it does not take into account the particles in the ground state, $\varepsilon = 0$. So, when we approximate the sum by an integral we must add the following term

$$N_0 = \frac{1}{e^{-\beta\mu} - 1}, \tag{1.8}$$

where N_0 is the occupation number of the ground state. This yields, to the result

$$N = \frac{z}{z - 1} + \frac{2\pi V}{h^3}(2m)^{3/2} \int_0^\infty \frac{\varepsilon^{1/2} d\varepsilon}{z^{-1}e^{\beta\varepsilon} - 1} = N_0 + N_e, \tag{1.9}$$

with $z \equiv \exp(\beta\mu)$ the fugasity and N_e are the number of particles in the exited states.

The integral in equation (1.9) can be written in terms of a generalized ζ-function or Bose-Einstein function, that can be expanded into a Taylor series [6],

$$g_\nu(z) := \frac{1}{\Gamma(\nu)} \int_0^\infty \frac{x^{\nu-1} dx}{z^{-1}e^x - 1} = \sum_j \frac{z^j}{j^\nu}. \tag{1.10}$$

The Bose-Einstein function converges for $0 \leq z < 1$, whereas the behavior for $z \to 1$ depends crucially on ν. So, the number of particles in the exited

states is given from the expression

$$N_e = V \frac{(2\pi m k T)^{3/2}}{h^3} g_{3/2}(z).$$ (1.11)

The Bose-Einstein function $g_{3/2}(z)$ increases monotonically with z in the interval $0 \leq z < 1$ and it has an upper bound for $z = 1$:

$$g_{3/2}(z) \leq g_{3/2}(1) = \zeta(3/2) \approx 2.612.$$ (1.12)

Thus, the number of particles in the excited states is also bounded,

$$N_e \leq N_e^{\max} = V \frac{(2\pi m k T)^{3/2}}{h^3} \zeta(3/2).$$ (1.13)

Now, if the particle number N exceeds this value, then the excited states can only receive a maximum number of particles, while the ground state will be occupied by all the remaining particles. This sudden macroscopic occupation of the ground state is known as Bose-Einstein condensation. The critical density for the onset of Bose-Einstein condensation is given by the relation

$$\frac{N}{V} > \frac{(2\pi m k T)^{3/2}}{h^3} \zeta(3/2).$$ (1.14)

Or in terms of critical temperature

$$T < T_c = \frac{h^2}{2\pi m k_B} \left[\frac{N}{V \zeta(3/2)} \right]^{2/3}.$$ (1.15)

Below the critical temperature T_c, the system can be regarded as a mixture of a normal phase and a Bose-Einstein condensed phase, consisting of

$$N_0 = N - N_e^{\max} = N \left[1 - \left(\frac{T}{T_c} \right)^{3/2} \right]$$ (1.16)

particles in the ground state. In experiments one observes a bimodal momentum distribution showing a broad thermal cloud and a narrow peak of the condensed fraction.

Here we must notice that the number of particles in the excited states N_e, is not bounded for two-dimensional volume. The corresponding Bose-Einstein function diverge for $z \to 1$. So, in these case there is Bose-Einstein condensation at zero temperature. However, if the Bose gas is confined by a harmonic-oscillator potential then the bosons can condensate at non-zero temperature even in two-dimensions.

1.1.2 Dilute Interacting Bose Gases

In the previous section we have summarized the statistical theory for an ideal bosonic gas: A quantum gas of non-interacting bosons. However, this is not the case in the experiments. The interactions between the bosons must be taken into account, so the dynamics of a Bose-Einstein condensation is a many-particle problem. The Hamiltonian for a Bose-Einstein condensation in an external potential $V_{\text{ext.}}(\vec{r})$, can be written in the following general form

$$\hat{H} = \sum_{i=1}^{N} \left[\frac{\hat{\vec{p}}_i^2}{2m} + V_{\text{ext.}}(\hat{\vec{r}}_i) \right] + \sum_{i<j} \hat{U}(\vec{r}_j - \vec{r}_i), \tag{1.17}$$

where $U(\vec{r}_j, \vec{r}_i)$ is the interaction potential between two bosons. In this expression, we have ignored the three- and higher-body interactions, because the mean interparticle distance in all experiments is much larger than the characteristic length scales of the interaction potential $U(\vec{r}_j, \vec{r}_i)$. Moreover, as we are going to see, since the atoms have low energies, we can approximate this interaction potential by a much simpler model potential, which is proportional to the scattering length, that gives the same asymptotic scattering wave function.

Let us see in more detail the scattering of two atoms in a Bose-Einstein condensation. In the center of mass system, the dynamics of the atoms is described by the Hamiltonian

$$\hat{H} = \frac{\hat{\vec{p}}^2}{2m_{\text{r}}} + \hat{U}(\vec{r}), \tag{1.18}$$

where m_{r} is the reduced mass of the atoms, $\vec{r}$ is the distance of the atoms and $\vec{p}$ is the momentum of the relative motion. For simplicity, we assume that the interaction potential has finite range b. However, all results hold for potential of the form $1/r^n$ with $n > 3$ [12]. In order to describe the scattering process, one writes the wave function for the relative motion as the sum of an incoming plane wave, with wave vector $\vec{k}$ and a scattered wave,

$$\psi = e^{i\vec{k}\cdot\vec{r}} + \psi_{\text{s}}(\vec{r}). \tag{1.19}$$

Now, at large interatomic separations the scattered wave is an outcoming spherical wave

$$\psi_{\text{s}}(\vec{r}) \simeq f(\vec{k}') \frac{e^{ikr}}{r}, \tag{1.20}$$

where $f(\vec{k}')$ is the scattering amplitude and $\vec{k}'$ specifies the wave vector of the scattered wave, which has magnitude k. Assuming a spherically symmetric

interaction between the atoms, the scattering amplitude f depends on the direction only through the scattering angle θ, which is the angle between the directions of the relative momentum of the atoms before and after the scattering. Now, if we choose the relative velocity of the incoming wave to be in the z-direction, the wave function for large r is written

$$\psi = e^{ikz} + f_k(\theta)\frac{e^{ikr}}{r}. \tag{1.21}$$

The scattering amplitude f depends on θ and on the magnitude k of the wave vector of the incoming wave. The energy of the state is given by the relation

$$E = \frac{\hbar^2 k^2}{2m_r}. \tag{1.22}$$

In a Bose-Einstein condensation, the scattering takes place only at very low energy and thus very small momentum. If $kb << 1$ is fulfilled, one can see that the scattering amplitude does not depend on θ any longer. Thus, the whole scattering problem is characterized by the value of f_k only. In the limit of very small momentum, $k \to 0$, one can show that the scattering amplitude converges to a fixed value,

$$\alpha_{\mathrm{s}} = \lim_{k \to 0} f_k, \tag{1.23}$$

the so-called s-wave scattering length. This quantity is sufficient to describe the interaction between bosons at very low energies. So, we can use a simple model potential which yields the same s-wave scattering length:

$$U(\vec{r}, \vec{r}\,') = \frac{4\pi\hbar\alpha_{\mathrm{s}}}{m_r}\delta(\vec{r} - \vec{r}\,') \equiv U_0\delta(\vec{r} - \vec{r}\,'). \tag{1.24}$$

Finally, we can write the Hamiltonian (1.17) in the following effective form

$$\hat{H} = \sum_{i=1}^{N} \left[\frac{\hat{\vec{p}}_i^2}{2m} + V_{\mathrm{ext.}}(\hat{\vec{r}}_i) \right] + U_0 \sum_{i<j} \delta(\vec{r}_j - \vec{r}_i). \tag{1.25}$$

1.1.3 The Single Particle Density Matrix

In section 1.1.1 we saw that below a critical temperature the atoms of an ideal gas tend to occupy the single particle ground state, a phenomenon that is known as "Bose-Einstein condensation". Let us give now a more general and formal definition for the Bose-Einstein condensation, a definition that holds even for interacting open many-body Bose systems. The definition we are going to give was introduced by O. Penrose and L. Onsager [3], and uses the so-called *single particle density matrix* (SPDM).

The SPDM is defined as follows

$$\sigma(\vec{r}, \vec{r}\,'; t) = N \int \Phi^*(\vec{r}, \vec{r}_2, ..., \vec{r}_N; t) \Phi(\vec{r}\,', \vec{r}_2, ..., \vec{r}_N; t) \, d\vec{r}_2...d\vec{r}_N, \qquad (1.26)$$

where Φ is the symmetrized full many-body bosonic wavefunction and N is the number of bosons. So the SPDM describes one boson in the presence of the environment that create the other $N - 1$ bosons.

Now we write the SPDM in the following form

$$\sigma(\vec{r}, \vec{r}\,', t) = \sum_k \lambda_k \phi_k^*(\vec{r}, t) \phi_k(\vec{r}\,', t), \qquad (1.27)$$

where λ_k are the eigenvalues and ϕ_k are the eigenfunctions of the SPDM. λ_k and ϕ_k are also known as natural occupation numbers and natural orbitals, respectively. Why we wrote the SPDM in this form we can understand if we consider the noninteracting case:

$$\hat{H} = \sum_{i=1}^{N} \left[\frac{\hat{\vec{p}}_i^2}{2m} + V_{\text{ext.}}(\hat{\vec{r}}_i) \right] \equiv \sum_{i=1}^{N} \hat{h}_i. \qquad (1.28)$$

For such a system below the critical temperature the bosons will macroscopically occupy the ground state ϕ_0 of the one-particle Hamiltonian $\hat{h}_i$. So the SPDM (1.26) can be written

$$\begin{aligned} \sigma(\vec{r}, \vec{r}\,') &\approx N\phi_0^*(\vec{r})\phi_0(\vec{r}\,') \int \prod_{j=2}^{N} \phi_0^*(\vec{r}_j)\phi_0(\vec{r}_j) \, d\vec{r}_j \\ &= N\phi_0^*(\vec{r})\phi_0(\vec{r}\,'). \end{aligned} \qquad (1.29)$$

This observation help us to formulate the following general definition for the BEC: A system shows Bose-Einstein condensation if one of the eigenvalues is of order N. Moreover the leading eigenvalue of the SPDM gives the number of atoms condensed in the ground state ϕ_0.

In the second quantization formalism the above definition takes the form

$$\sigma(\vec{r}, \vec{r}\,'; t) = \langle \hat{\psi}^\dagger(\vec{r}; t) \hat{\psi}(\vec{r}\,'; t) \rangle, \qquad (1.30)$$

where $\hat{\psi}^\dagger(\vec{r}; t)$ and $\hat{\psi}(\vec{r}; t)$ are the bosonic creation and annihilation operators at position $\vec{r}$, respectively. The averaging $\langle \dots \rangle$ indicates the usual quantum mechanical expectation value with respect to the state of the system.

1.2 Experiments with BEC

Although the prediction of the Bose-Einstein phenomenon was known since 1924 the experimental realization came decades later. The reason was that the stable phase of all interacting quantum systems at very low temperatures is a solid or a liquid and not a BEC. One can overcome this problem by using extremely dilute gases[1]. The condensation of a pair of atoms to a bound state requires three-body scattering events, to conserve the momentum and energy, while the thermalization of an atomic gas requires only two-body scattering. However, at very low densities, quantum phenomena can be observed at very low temperatures: the critical temperature for BEC formation decreases with the density. For Rubidium gas with density $N/V = 10^{15} \text{cm}^{-3}$, equation (1.15) predicts a critical temperature of $T_\text{c} = 1.85 \mu K$. These temperatures became feasible only in the 1980s with the development of laser cooling and magneto-optical traps (MOT) for neutral atoms. In 1995 the groups of Wieman and Cornell at JILA and of Ketterle at MIT combined optical and evaporating cooling in order to achieve the critical temperature for BEC in a gas of Rubidium or Sodium atoms, respectively [8,9]. In the next subsection we briefly discuss the experimental techniques used to produce a BEC in a dilute gas of Alkali atoms.

1.2.1 Realizing the Bose-Einstein Condensation

The Alkali atoms are vaporized by electric heating from a dispenser in an ultrahigh vacuum chamber. The atoms are captured in a MOT where they are precooled to temperatures of milli-Kelvins. The critical temperature is achieved by the combination of laser-cooling in the MOT and evaporative cooling, which is usually realized in a purely magnetic trap. Next we discuss the necessary ingredients of the above procedure: magnetic and magneto-optical traps, Doppler and evaporative cooling.

Magnetic traps use the forses which applied on magnetic dipoles when they are in inhomogeneous fields. An atom in a weak magnetic field, $\vec{B}(\vec{r})$, experiences an energy shift due to Zeeman effect:

$$\Delta E(\vec{r}) = g_L \mu_B m_F |\vec{B}(\vec{r})|, \qquad (1.31)$$

where g_L is the Landé factor, μ_B is Bohr's magneton and m_F is the magnetic quantum number. Atoms can be trapped by magnetic fields if the potential (1.31) has a local minimum, which is only possible if $m_F > 0$, since $|\vec{B}(\vec{r})|$

---

[1]The particle density at the center of a BEC atomic cloud is typically 10^{13}-10^{15}cm^{-3}.
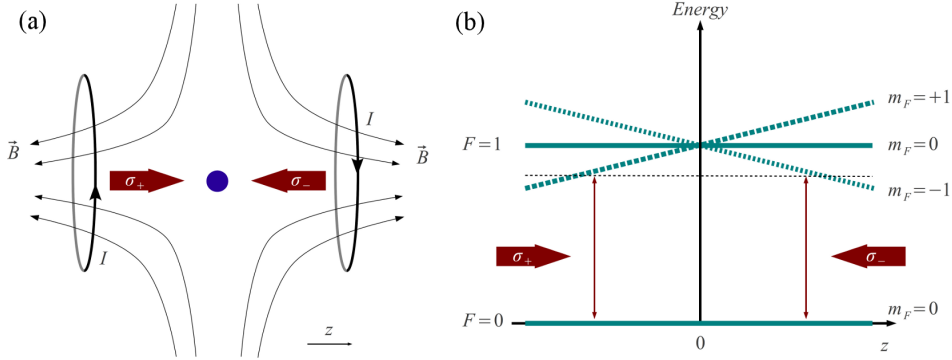
Figure 1.2: *Schematic of a magneto-optical trap* (a), *and the atomic level scheme* (b).

can assume a minimum but not a maximum [11]. Indeed we have

$$
\begin{aligned}
\nabla \times (\nabla \times \vec{B}) &= 0 \Rightarrow \\
\nabla \cdot (\nabla \cdot \vec{B}) - \nabla^2 \vec{B} &= 0 \Rightarrow \\
\nabla^2 \vec{B} &= 0,
\end{aligned}
\tag{1.32}
$$

so the components of the magnetic field is a harmonic function which cannot have a local extremum. Thus $\vec{B}^2(\vec{r})$ cannot assume a local maximum but it can assume a minimum, for example at the zeros of the magnetic field $\vec{B}(\vec{r}_0) = 0$.

The majority of experiments use magneto-optical traps, see figure 1.2. In this setup along the axis $x = y = 0$, the quadrupole magnetic field varies linearly in z:

$$
\vec{B}(z) = B_0 \frac{z}{z_0} \vec{e}_z.
\tag{1.33}
$$

In figure 1.2 (b) we have the energy levels of an atom in such a trap, where F is the angular momentum. The magnetic quantum number m_F is given with respect to the z-axis. The magnetic field traps the atoms with $m_F = +1$ traveling to the right and the $m_F = -1$ atoms traveling to the left. In the opposite directions the atoms are trapped by the radiation pressure of laser beams. At the position $z = +z'$ the $m_F = -1$ atoms get into resonance with the σ_- laser beam. Photons are absorbed and spontaneously reemitted into random direction. Effectively each absorption-emission cycle leads transfer momentum of $p_{\text{recoil}} = -\hbar k$ (here k is the wave number of the laser beam), leading to an effective force into the $-z$-direction. A similar force is created by the σ_+ laser beam in the $+z$-direction around $z = -z'$. The MOT setup is also used for Doppler cooling of the atoms. Indeed, the frequency of the laser

beams is shifted in the rest frame of the atoms due to the Doppler effect. So the radiation pressure force does not only depends on the position but also on the velocity of the atoms [13]

$$F \approx 2\hbar k \Gamma \Omega^2 \frac{\Delta(\vec{k} \cdot \vec{z}) + \beta z}{[\Delta^2 + (\Gamma/2)^2]^2},$$ (1.34)

where Γ is the width of the atomic transition, Ω is the Rabi frequency and Δ is the detuning. Thus, in addition to the conservative force term which traps the atoms, there is also a friction term which Doppler cooling them. The temperature that we can achive is given in [13] by

$$k_B T_{\text{Dop.}} \approx \frac{\hbar \Gamma}{4},$$ (1.35)

so, for example, for Rubidium atoms we have a minimum temperature of $T_{\text{Dop.}} \approx 143 \mu K$.

Finally, the desired temperature for the creation of a BEC can be achieved with evaporative cooling. We lower the trapping potential so the atoms with highest energy escape from the trap. The rest of the atoms thermalize at a lower temperature by elastic collisions.

1.2.2 Optical Lattices

After the BEC is prepared, it can be adiabatically transfered to another trapping potential to perform variety of experiments. Here we discuss such a trapping potential the optical lattice, since is the setup we use in the main part of this thesis. Such a potential for neutral atoms is generated by a laser beam which is far detuned from an atomic resonance. We assume that the laser couples only the ground state $|g\rangle$ and the first excited state $|e\rangle$ so the atom can be described by a two-level system, as it is illustrated in figure 1.3. The Hamiltonians that describe the atoms and the electromagnetic field are given by

$$\hat{H}_{\text{atom}} = \hbar \omega_0 |e\rangle\langle e|,$$ (1.36)

$$\hat{H}_{\text{EM}} = \hbar \omega \left(\hat{a}^\dagger \hat{a} + \frac{1}{2} \right),$$ (1.37)

where $\hat{a}$ is the photon annihilation operator. If the detuning of the laser from the atomic transition, $\Delta = \omega - \omega_0$, is small $|\Delta| \ll \omega_0$ then the state with the atom in the ground state and N photons in the field, $|0\rangle \equiv |g\rangle \otimes |N\rangle$ has similar energy to the state with the atom in excited state and $N - 1$
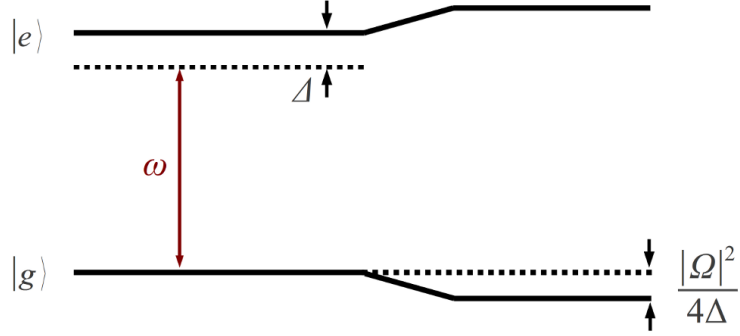
Figure 1.3: *AC Stark shift induced by atom-light interaction. The laser fre-
quency is ω which is detuned from the atomic resonance by Δ.*

photons, $|1\rangle \equiv |e\rangle \otimes |N-1\rangle$, $E_1 - E_0 = -\hbar\Delta$. The interactions couple
these two states. We will use the dipole approximation which assumes that
the spatial variation of the electromagnetic field is small compared with the
atomic wave function, so the coupling Hamiltonian in the interaction picture
takes the form

$$\hat{H}_c = -\vec{d}\cdot\vec{E}$$
$$= \left(|e\rangle\langle g|e^{i\omega_0 t} + |g\rangle\langle e|e^{-i\omega_0 t}\right)\left(\frac{\hbar}{2}\Omega^*(\vec{r})\hat{a}^\dagger e^{i\omega t} + \frac{\hbar}{2}\Omega(\vec{r})\hat{a}e^{-i\omega t}\right)(1.38)$$

where Ω is the Rabi frequency. Now we use the rotating wave approximation,
which is valid when $|\Delta| << \omega_0$, so we neglect the rapidly oscillating phases,
$\exp\{\pm i(\omega + \omega_0)t\}$, and we keep only processes near the resonant frequency.
Thus the coupling Hamiltonian (1.38) becomes

$$\hat{H}_c \approx \left(\frac{\hbar}{2}\Omega(\vec{r})|e\rangle\langle g|\ \hat{a}\ e^{-i\Delta t} + \frac{\hbar}{2}\Omega^*(\vec{r})|g\rangle\langle e|\ \hat{a}^\dagger e^{i\Delta t}\right). \qquad (1.39)$$

The resonant process correspond to either the relaxation of the atom with
absorption of a photon or the excitation of the atom with the emission of a
photon.

If the detuning is large compared to the Rabi frequency, $\Delta \gg \Omega$ the effect
of the coupling between the states $|0\rangle$ and $|1\rangle$ can be determined with the
help of second order perturbation theory. So the energy shift is given by

$$E_{0,1}^{(2)} = \pm\frac{|\langle 1|\hat{H}_c|0\rangle|^2}{\hbar\Delta} = \pm\hbar\frac{|\Omega(\vec{r})|^2}{4\Delta}, \qquad (1.40)$$

with $+$ and $-$ for the $|0\rangle$ and $|1\rangle$ states respectively. This energy shift is
the so-called AC Stark shift. The atoms are practically always in the ground

state, so the atoms experience the optical potential $V_{\text{opt.}}(\vec{r}) = |\Omega(\vec{r})|^2/4\Delta$. For $\Delta > 0$ (blue detuning) the potential is repulsive and for $\Delta < 0$ (red detuning) the potential is attractive.

A more detailed analysis shows that there is an additional dissipative force which acts on the atoms, caused by the absorption and subsequent spontaneous emission of a photon. However, the rate of spontaneous emission scales as $|\Omega|^2/\Delta^2$, so for far detuned laser beam it can be neglected.

An important application is the realization of periodic potentials for ultracold atoms. A stabilized laser is reflected so that the counterpropagating beams form a standing wave. The laser intensity is periodically modulated with period $\lambda/2$, generating the potential

$$
\begin{aligned}
V_{\text{opt.}}(\vec{r}) &\sim \langle (\vec{E}\cos(\omega t - kx) + \vec{E}\cos(\omega t + kx))^2 \rangle \\
&\sim |\vec{E}|^2(1 + \cos(2kx)),
\end{aligned}
\tag{1.41}
$$

where $k = 2\pi/\lambda$ and $\langle \cdot \rangle$ denotes the time average over rapidly rotating terms, $\langle \cos^2(\omega t) \rangle = 1/2$.

1.3   Lattices and the Bose-Hubbard Model

In this thesis we study the dynamics of a Bose-Einstein condensation which is loaded into a one dimensional optical lattice. As we discussed in subsection 1.2.2, such a lattice is created by retroreflecting a laser beam. The atoms interacts with the electromagnetic field of the laser, so they feel a periodic potential which has wells separated by a distance of the order of the laser wavelength. This optical potential has the form

$$
V_{\text{lat.}}(x) = V_0 \sin^2(kx),
\tag{1.42}
$$

where $k = 2\pi/\lambda$ is the absolute value of the wave vector of the laser light and V_0 is four times the width of a single laser beam without the reflection, due to the constructive interference of the lasers.

Ultracold atoms in an optical lattice is a system with the remarkable property that experimental parameters can be tuned to almost arbitrary values. For example the interactions between the atoms can be accurately controlled by tunning a Feshbach resonance [5]. This property makes these systems an ideal model systems for a variety of physical disciplines from condensed matter to nonlinear dynamics.

In the following subsection we briefly present the physics of a particle in one dimensional periodic potential and we derive the band structure for the potential (1.42). Finally, we derive the Bose-Hubbard model, a simple

theoretical model which became very popular due to the enormous progress in the experiments with ultracold atoms in optical lattices.

1.3.1 Periodic Potentials

A fundamental property of a periodic potential is the band structure. Suppose one particle with mass m in an one dimensional periodic potential with period α: $V_{\text{lat.}}(x) = V_{\text{lat.}}(x + \alpha)$. Such a system is described by the Hamiltonian

$$\hat{H} = \frac{\hat{p}^2}{2m} + V_{\text{lat.}}(\hat{x}). \tag{1.43}$$

Bloch's theorem states that the eigenstates $\varphi_q^n(x)$ of the Hamiltonian (1.43) can be written in the following special form:

$$\varphi_q^n(x) = e^{iqx} u_q^n(x), \tag{1.44}$$

where the functions $u_q^n(x)$ have the same periodicity as the potential $V_{\text{lat.}}$. If we substitute equation (1.43) into the time independent Schrödinger equation, $\hat{H}\varphi_q^n(x) = E_q^n \varphi_q^n(x)$, we obtain the following equation for the functions $u_q^n(x)$:

$$\left[\frac{(\hat{p} + \hbar q)^2}{2m} + V_{\text{lat.}}(x) \right] u_q^n(x) = E_q^n u_q^n(x). \tag{1.45}$$

The quantity, that was introduced in (1.44), $\hbar q$ is called quasi-momentum and could be understood as the characteristic quantum number of the translational symmetry of the periodic potential $V_{\text{lat.}}$. The wave vector q is confined to the first Brillouin zone: $-\pi/\alpha < q \leqslant \pi/\alpha$. Finally, the index n, in the previous equations, labels the discrete energy levels for a fixed quasi-momentum q.

We can easily find the band structure for a simple periodic potential, like the sinusoidal: $V_{\text{lat.}}(x) = V_0 \sin^2(kx)$. In this case the time independent Schrödinger equation takes the form

$$-\frac{d^2}{dy^2}\varphi_q^n(y) + \frac{V_0}{4E_R}(2 - 2\cos(2y))\varphi_q^n(y) = \frac{E_q^n}{E_R}\varphi_q^n(y), \tag{1.46}$$

where $E_R = \hbar^2 k^2/2m$ is the atomic recoil energy and $y = kx$. Equation (1.46) is in fact a Mathieu equation [21]

$$\frac{d^2z}{dy^2} + (t + 2s\cos(2y))z = 0, \tag{1.47}$$

with $s = V_0/4E_R$ and $t = E_q^n/E_R - V_0/E_R$. The Mathieu equation has a solution of the Floquet form $e^{iqx}P(x)$, where $P(x)$ is a periodic function.
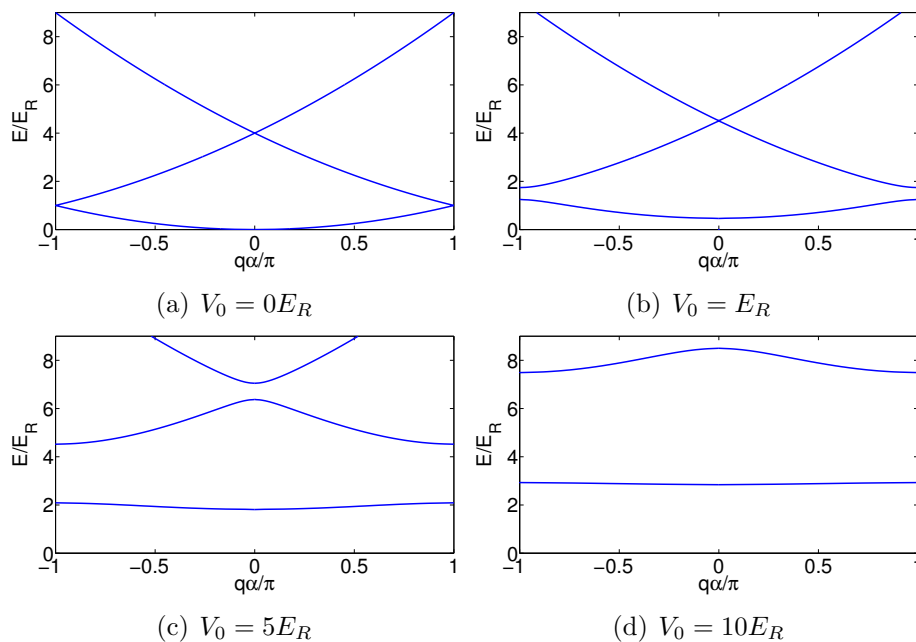
Figure 1.4: *Band structure of a periodic potential with period α.*

The parameter q (the wave-number in the lattice language) is the so-called characteristic exponent and $t = t(q, s)$ is the characteristic parameter which is a complicated function of its arguments.

In figure 1.4 the band structure for the sinusoidal potential is depicted. In figure 1.4 (a) $V_0 = 0$ so the particle is free and the spectrum is quadratic in q. As we start to turn on the periodic potential, figure 1.4 (b), we observe a gap at the edge of the Brillouin zone ($q\alpha \pm \pi$). Thus the band structure appears. As the depth further increases the band gap increases also, while the band width decreases. For very deep lattices, figure 1.4 (d), the ground band becomes almost flat and the bands are separated by a very large gap.

1.3.2 The Bose-Hubbard Model

In this subsection we derive the so-called Bose-Hubbard model. This model describes, in a simplified way, the many-body dynamics of ultracold Bosons in a deep optical lattice: it takes into account the competition between the kinetic energy and the interaction energy of the system.

In order to derive this model we begin from the second quantized version

of Hamiltonian (1.25) in the presence of a periodic optical lattice

$$\hat{H} = \int d\vec{r}\,\hat{\Psi}^\dagger(\vec{r})\left[-\frac{\hbar^2}{2m}\nabla^2 + V_{\text{lat.}}(\vec{r}) + V_{\text{trap.}}(\vec{r})\right]\hat{\Psi}(\vec{r}) +$$
$$+\frac{U_0}{2}\int d\vec{r}\,\hat{\Psi}^\dagger(\vec{r})\hat{\Psi}^\dagger(\vec{r})\hat{\Psi}(\vec{r})\hat{\Psi}(\vec{r}), \tag{1.48}$$

where the operators $\hat{\Psi}^\dagger(\vec{r})$ and $\hat{\Psi}(\vec{r})$ create and annihilate a boson at the position $\vec{r}$, respectively. In Hamiltonian (1.48) we have assumed that except the periodic potential there is also an overall trapping potential $V_{\text{trap.}}(\vec{r})$. We are interested to study the dynamics in a deep optical lattice, so it is natural to choose a basis where the eigenfunctions of the Hamiltonian are localized. This basis is constructed by the well-known Wannier functions

$$w_n(\vec{r} - \vec{r}_i) = \frac{1}{M}\sum_{\vec{q}}\text{e}^{-i\vec{q}\cdot\vec{r}_i}\varphi_{\vec{q}}^n(\vec{r}), \tag{1.49}$$

where the summation is over the quasi-momentum $\vec{q}$ in the first Brillouin zone and M is the number of lattice sites.

We now assume that the potential is deep so the energy gap between the bands is very large if we compare it with the chemical potential, the interaction energy and the kinetic energy. This assures that all the particles will stay in the ground band

$$\hat{\Psi}(\vec{r}) = \sum_{j=1}^{M} w_0(\vec{r} - \vec{r}_j)\hat{\alpha}_j, \tag{1.50}$$

where $\hat{\alpha}_j$ annihilates a boson at site j. Now if we insert equation (1.50) into the Hamiltonian (1.48) we obtain the Bose-Hubbard Hamiltonian [14]

$$\hat{H} = \sum_{j=1}^{M}\varepsilon_j\,\hat{\alpha}_j^\dagger\hat{\alpha}_j - \sum_{\langle i,j\rangle}J_{ij}\,\hat{\alpha}_i^\dagger\hat{\alpha}_j + \frac{1}{2}\sum_{j=1}^{M}U_j\,\hat{\alpha}_j^\dagger\hat{\alpha}_j^\dagger\hat{\alpha}_j\hat{\alpha}_j \tag{1.51}$$

where the summation in the first term is over adjacent lattice sites $i = j \pm 1$. In the above equation we have defined the following parameters

$$\varepsilon_j = \int d\vec{r}\,V_{\text{trap.}}(\vec{r})|w_0(\vec{r} - \vec{r}_j)|^2, \tag{1.52}$$

$$J_{ij} = \int d\vec{r}\,w_0^*(\vec{r} - \vec{r}_j)\left[-\frac{\hbar^2}{2m}\nabla^2 + V_{\text{lat.}}(\vec{r})\right]w_0(\vec{r} - \vec{r}_{i=j\pm1}), \tag{1.53}$$

$$U_j = \frac{4\pi\alpha_{\text{s}}\hbar^2}{m}\int d\vec{r}\,|w_0(\vec{r} - \vec{r}_j)|^4. \tag{1.54}$$

From the above expressions we can easily understand their physical meaning: ε_j is the on-site potential, J_{ij} is connected to the kinetic energy, so it parametrizes the tunneling between adjacent sites and U_j is the on-site interaction strength.

Here we must note that in the derivation of the Bose-Hubbard Hamiltonian (1.51) we have used the fact that the lattice is deep so we have neglected terms of the form

$$\int d\vec{r}|w_0(\vec{r} - \vec{r}_i)|^2|w_0(\vec{r} - \vec{r}_j)|^2 \approx 0, \tag{1.55}$$

for $i \neq j$. Moreover, we have used the tight-binding approximation and we have omitted terms of the type

$$\int d\vec{r}w_0^*(\vec{r} - \vec{r}_j) \left[-\frac{\hbar^2}{2m}\nabla^2 + V_{\text{lat.}}(\vec{r}) \right] w_0(\vec{r} - \vec{r}_{i=j\pm2,3,\dots}) \approx 0. \tag{1.56}$$

Finally, if the global trapping potential is present but much weaker than the lattice potential, $V_{\text{trap}} \ll V_{\text{lat.}}$, then we can take for the value of the interaction strength at each lattice site, $U_j = U$, and also the same tunneling strength $J_{ij} = J$. After this assumption we can write the Bose-Hubbard Hamiltonian in the following well-known form

$$\hat{H} = \sum_{j=1}^{M}\varepsilon_j \; \hat{\alpha}_j^\dagger\hat{\alpha}_j - J\sum_{j}^{M-1}(\hat{\alpha}_{j+1}^\dagger\hat{\alpha}_j + \hat{\alpha}_j^\dagger\hat{\alpha}_{j+1}) + \frac{U}{2}\sum_{j=1}^{M}\hat{\alpha}_j^\dagger\hat{\alpha}_j^\dagger\hat{\alpha}_j\hat{\alpha}_j. \tag{1.57}$$

Before we close the discussion about the Bose-Hubbard model we will define the SPDM, we introduced in subsection 1.1.3, for a lattice system. In this case it takes the following simple form

$$\sigma_{j,k} = \langle\hat{\alpha}_j^\dagger\hat{\alpha}_k\rangle, \quad j,k = 1,2,\dots M. \tag{1.58}$$

The diagonals of the SPDM give the population in each lattice site, while the off-diagonals give the coherences between the lattice sites.

1.4 The Master Equation for Open Quantum Systems

In the main part of this thesis we deal with open quantum systems. In order to study the dynamics of such a system we are going to use the Master equation formalism. Generally speaking, an open quantum system is a
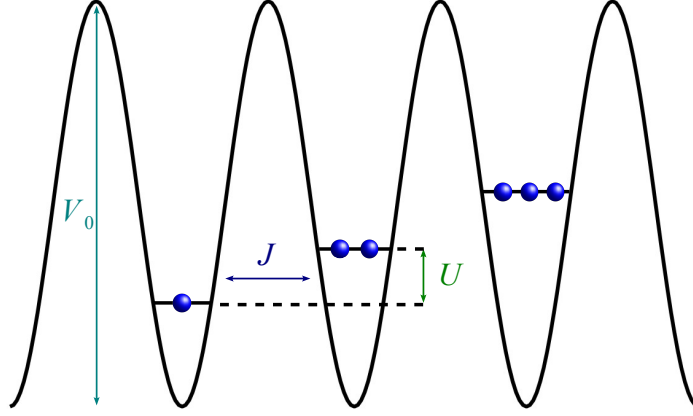
Figure 1.5: *Sketch of an one dimensional optical lattice described by a Bose-Hubbard Hamiltonian.*

system which is coupled to an environment. With the term environment we mean another quantum (or even classical) system which we cannot control or we don't care to investigate. Now, the Master equation formalism tells us that the evolution of the reduced density matrix of our system σ, is given by an equation of the general form [22, 23]

$$\frac{d}{dt}\hat{\sigma}(t) = -i[\hat{H}_{\mathrm{s}}, \hat{\sigma}(t)] - \sum_j \frac{\gamma_j}{2} \left(\hat{L}_j^\dagger \hat{L}_j \hat{\sigma}(t) + \hat{\sigma}(t) \hat{L}_j^\dagger \hat{L}_j - 2\hat{L}_j \hat{\sigma}(t) \hat{L}_j^\dagger \right), \ (1.59)$$

where the first term, in the right hand side, gives the unitary evolution ($\hat{H}_{\mathrm{s}}$ is the Hamiltonian of the system), while the second one gives the non-unitary contribution to the evolution. The Master equation (1.59) is of the Lindblad form. One can write it in a more general form, but this would be out of the purpose of this presentation. The operators $\hat{L}_j$ are called Lindblad operators and they constitute a basis in the space of operators for the system.

In order to derive such an equation, one should do several assumptions and approximations. The core of the derivation is the so-called Born-Markov approximation. This approximation states that the correlation functions of the environment must decay much faster than the characteristic time which is defined by the interaction between system and environment. In other words, the environment should have very "weak memory". In order to present the main steps of such a derivation, in the following subsection we derive a Master equation for a very simple case, a single non-interacting site which is coupled to a bosonic reservoir at the grand canonical ensemble.

1.4.1 A Single Site Coupled to a Bosonic Reservoir

Let us study a simple system which consists of a single noninteracting site coupled to a bosonic reservoir at some temperature T and chemical potential μ. We will trace over the reservoir degrees of freedom, using the well-known Born-Markov elimination method [22, 23]. The Hamiltonian for this system is given by the following expression:

$$\hat{H} = \hat{H}_{\mathrm{s}} + \hat{H}_{\mathrm{r}} + \hat{H}_{\mathrm{c}}, \tag{1.60}$$

where

$$\hat{H}_{\mathrm{s}} = E\hat{\alpha}^{\dagger}\hat{\alpha}, \tag{1.61}$$

$$\hat{H}_{\mathrm{r}} = \sum_{\kappa} \varepsilon_{\kappa} \hat{R}_{\kappa}^{\dagger}\hat{R}_{\kappa}, \tag{1.62}$$

$$\hat{H}_{\mathrm{c}} = \sum_{\kappa} (\gamma_{\kappa} \hat{R}_{\kappa}\hat{\alpha}^{\dagger} + \gamma_{\kappa}^{*}\hat{R}_{\kappa}^{\dagger}\hat{\alpha}), \tag{1.63}$$

are the Hamiltonian for the single site, the bosonic reservoir and the site-reservoir coupling term respectively. The evolution of our system is described by the Heisenberg equation of motion

$$i\frac{d}{dt}\hat{\rho}(t) = -[\hat{H}_{\mathrm{s}} + \hat{H}_{\mathrm{r}} + \hat{H}_{\mathrm{c}}, \hat{\rho}(t)] \tag{1.64}$$

It is more convenient to rewrite the previous equation in the interaction picture

$$i\frac{d}{dt}\hat{\rho}_{\mathrm{i}}(t) = [\mathcal{H}_{\mathrm{c}}(t), \hat{\rho}_{\mathrm{i}}(t)] \tag{1.65}$$

where

$$\hat{\rho}_{\mathrm{i}}(t) = \exp\{i(\hat{H}_{\mathrm{s}} + \hat{H}_{\mathrm{r}})t\}\hat{\rho}(t)\exp\{-i(\hat{H}_{\mathrm{s}} + \hat{H}_{\mathrm{r}})t\} \tag{1.66}$$

and

$$\mathcal{H}_{\mathrm{c}}(t) = \exp\{i(\hat{H}_{\mathrm{s}} + \hat{H}_{\mathrm{r}})t\}\hat{H}_{\mathrm{c}}\exp\{-i(\hat{H}_{\mathrm{s}} + \hat{H}_{\mathrm{r}})t\}. \tag{1.67}$$

Formal integration of equation(1.65), from $t = -\infty$ when the coupling was turned on, gives the expression

$$\hat{\rho}_{\mathrm{i}}(t) = \hat{\rho}_{\mathrm{i}}(-\infty) + \frac{1}{i}\int_{-\infty}^{t} dt'[\mathcal{H}_{\mathrm{c}}(t'), \hat{\rho}_{\mathrm{i}}(t')]. \tag{1.68}$$

Iterating to second order in interaction Hamiltonian, we have

$$\begin{aligned}
\hat{\rho}_{\mathrm{i}}(t) =\ & \hat{\rho}_{\mathrm{i}}(-\infty) + \frac{1}{i}\int_{-\infty}^{t} dt'[\mathcal{H}_{\mathrm{c}}(t'), \hat{\rho}_{\mathrm{i}}(-\infty)] + \\
& + \left(\frac{1}{i}\right)^{2}\int_{-\infty}^{t} dt''\int_{\infty}^{t''} dt'[\mathcal{H}_{\mathrm{c}}(t''), [\mathcal{H}_{\mathrm{c}}(t'), \hat{\rho}_{\mathrm{i}}(t')]].
\end{aligned} \tag{1.69}$$

By differentiating with respect to t we obtain

$$\frac{d}{dt}\hat{\rho}_\text{i}(t) = \frac{1}{i}[\mathcal{H}_\text{c}(t), \hat{\rho}_I(-\infty)] + \left(\frac{1}{i}\right)^2 \int_{-\infty}^t dt'[\mathcal{H}_\text{c}(t), [\mathcal{H}_\text{c}(t'), \hat{\rho}_\text{i}(t')]]. \quad (1.70)$$

We trace equation (1.70) over the reservoir degrees of freedom

$$\frac{d}{dt}\hat{\sigma}_\text{i}(t) = \left(\frac{1}{i}\right)^2 \int_{-\infty}^t dt' \text{Tr}_\text{r}[\mathcal{H}_\text{c}(t), [\mathcal{H}_\text{c}(t'), \hat{\rho}_\text{i}(t')]], \quad (1.71)$$

with

$$\hat{\sigma}_\text{i} = \text{Tr}_\text{r}\hat{\rho}_\text{i} \quad (1.72)$$

that is the reduced density matrix that describes the quantum dot and we have used that

$$Tr_\text{r}[\mathcal{H}_\text{c}(t), \hat{\rho}_\text{i}(-\infty)] = 0. \quad (1.73)$$

The last relation is true since $\mathcal{H}_\text{c}$ has no diagonal elements in the basis where $\hat{H}_\text{r}$ is diagonal and the initial density matrix is assumed that it can be written as a tensor product:

$$\hat{\rho}_\text{i}(-\infty) = \hat{\sigma}_\text{i}(-\infty) \otimes \hat{\varrho}_\text{i}^\text{r}(-\infty), \quad (1.74)$$

where $\hat{\varrho}^\text{r}$ is the reduced density matrix of the reservoir.

Equation 1.71 contains the density matrix of the total system, $\hat{\rho}_\text{i}(t)$, on the right hand side. In order to write a closed evolution equation for the reduced density matrix, $\hat{\sigma}_\text{i}(t)$, we use the Born-Markov approximation. The Born approximation assumes that the coupling between the dot and the reservoir is weak, so the influence of the dot on the reservoir is small. Thus, the density matrix of the reservoir is almost not affected at any time t and the total density matrix can be written as a tensor product

$$\hat{\rho}_\text{i}(t) = \hat{\sigma}_\text{i}(t) \otimes \hat{\varrho}_\text{i}^\text{r}. \quad (1.75)$$

Inserting (1.75) into the exact expression (1.71) we have a closed integro-differential equation for the reduced density matrix

$$\frac{d}{dt}\hat{\sigma}_\text{i}(t) = \left(\frac{1}{i}\right)^2 \int_{-\infty}^t dt' \text{Tr}_\text{r}[\mathcal{H}_\text{c}(t), [\mathcal{H}_\text{c}(t'), \hat{\sigma}_\text{i}(t') \otimes \hat{\varrho}_\text{i}^\text{r}]]. \quad (1.76)$$

Further, the Markov approximation assumes that σ depends only on the present and not on the past, this simply means that we replace $\sigma(t')$ in equation (1.76) by $\hat{\sigma}(t)$:

$$\frac{d}{dt}\hat{\sigma}_\text{i}(t) = \left(\frac{1}{i}\right)^2 \int_{-\infty}^t dt' \text{Tr}_\text{r}[\mathcal{H}_\text{c}(t), [\mathcal{H}_\text{c}(t'), \hat{\sigma}_\text{i}(t) \otimes \hat{\varrho}_\text{i}^\text{r}]]. \quad (1.77)$$

Let us go back to the interaction term (1.67). As one can easily see that the operators $\hat{\alpha}, \hat{\alpha}^\dagger$ are eigenoperators of the Hamiltonian $\hat{H}_\mathrm{s}$

$$[\hat{H}_\mathrm{s}, \hat{\alpha}^\dagger] = E\hat{\alpha}^\dagger,$$

$$[\hat{H}_\mathrm{s}, \hat{\alpha}] = -E\hat{\alpha},$$

so we can write the corresponding interaction picture operators in the form

$$e^{i\hat{H}_\mathrm{s}t}\hat{\alpha}e^{-i\hat{H}_\mathrm{s}t} = e^{iEt}\hat{\alpha}, \tag{1.78}$$

$$e^{i\hat{H}_\mathrm{s}t}\hat{\alpha}^\dagger e^{-i\hat{H}_\mathrm{s}t} = e^{-iEt}\hat{\alpha}^\dagger. \tag{1.79}$$

The above two equations allows as to write the interaction term (1.67) in the following simple form

$$\mathcal{H}_\mathrm{c}(t) = \sum_\kappa (\gamma_\kappa \hat{R}_\kappa \hat{\alpha}^\dagger e^{-i(\varepsilon_\kappa - E)t} + \gamma_\kappa^* \hat{R}_\kappa^\dagger \hat{\alpha} e^{i(\varepsilon_\kappa - E)t}). \tag{1.80}$$

We assume that the reservoir is a heat bath in equilibrium, at temperature T and chemical potential μ

$$\hat{\varrho}^\mathrm{r} = \frac{e^{-(\hat{H}_R - \mu\hat{N})/kT}}{\mathrm{Tr}_\mathrm{r}\{e^{-(\hat{H}_R - \mu\hat{N})/kT}\}}, \tag{1.81}$$

where k is the Boltzmann constant. This allows as to calculate the following averages

$$\mathrm{Tr}_\mathrm{r}\{\hat{R}_\kappa \hat{R}_\lambda \hat{\varrho}^\mathrm{r}\} = Tr_\mathrm{r}\{\hat{R}_\kappa^\dagger \hat{R}_\lambda^\dagger \hat{\varrho}^\mathrm{r}\} = 0, \tag{1.82}$$

$$\mathrm{Tr}_\mathrm{r}\{\hat{R}_\kappa^\dagger \hat{R}_\lambda \hat{\varrho}^\mathrm{r}\} = \frac{\delta_{\kappa\lambda}}{e^{(\varepsilon_\lambda - \mu)/kT} - 1}, \tag{1.83}$$

$$\mathrm{Tr}_\mathrm{r}\{\hat{R}_\kappa \hat{R}_\lambda^\dagger \hat{\varrho}^\mathrm{r}\} = \left(1 + \frac{1}{e^{(\varepsilon_\lambda - \mu)/kT} - 1}\right)\delta_{\kappa\lambda}. \tag{1.84}$$

Using equations (1.80),(1.82)-(1.84), the equation (1.77) becomes

$$\frac{d}{dt}\hat{\sigma}_\mathrm{i}(t) = -\sum_\kappa |\gamma_\kappa|^2 \int_{-\infty}^t dt'[\{(1 + \langle n_\kappa\rangle)\hat{\alpha}^\dagger\hat{\alpha}\hat{\sigma}_\mathrm{i}(t) - \langle n_\kappa\rangle\hat{\alpha}^\dagger\hat{\sigma}_\mathrm{i}(t)\hat{\alpha} -$$

$$-(1 + \langle n_\kappa\rangle)\hat{\alpha}\hat{\sigma}_\mathrm{i}(t)\hat{\alpha}^\dagger + \langle n_\kappa\rangle\hat{\sigma}_\mathrm{i}(t)\hat{\alpha}\hat{\alpha}^\dagger\}e^{-i(\varepsilon_\kappa - E)(t-t')} + \{\langle n_\kappa\rangle\hat{\alpha}\hat{\alpha}^\dagger\hat{\sigma}_\mathrm{i}(t) -$$

$$-(1+\langle n_\kappa\rangle)\hat{\alpha}\hat{\sigma}_\mathrm{i}(t)\hat{\alpha}^\dagger - \langle n_\kappa\rangle\hat{\alpha}^\dagger\hat{\sigma}_\mathrm{i}(t)\hat{\alpha} + (1+\langle n_\kappa\rangle)\hat{\sigma}_\mathrm{i}(t)\hat{\alpha}^\dagger\hat{\alpha}\}e^{i(\varepsilon_\kappa - E)(t-t')}], \tag{1.85}$$

where

$$\langle n_\kappa\rangle = \frac{1}{e^{(\varepsilon_\kappa - \mu)/kT} - 1} \tag{1.86}$$

is the Bose occupation distribution. The next step is to use the following relation

$$\int_0^\infty e^{\pm ixy} dy = \pi \delta(x) \pm iP\frac{1}{x}, \tag{1.87}$$

where P is the Cauchy principal part, and replace the sum over κ with a weighting factor the density of states $g(\varepsilon_\kappa)$. After this we have

$$\frac{d}{dt}\hat{\sigma}_{\mathrm{i}}(t) = -\frac{\Gamma}{2}[(1 + \langle n \rangle)\hat{\alpha}^\dagger \hat{\alpha}\hat{\sigma}_{\mathrm{i}}(t) - 2\langle n \rangle \hat{\alpha}^\dagger \hat{\sigma}_{\mathrm{i}}(t)\hat{\alpha} - 2(1 + \langle n \rangle)\hat{\alpha}\hat{\sigma}_{\mathrm{i}}(t)\hat{\alpha}^\dagger +$$

$$+ \langle n \rangle \hat{\sigma}_{\mathrm{i}}(t)\hat{\alpha}\hat{\alpha}^\dagger + \langle n \rangle \hat{\alpha}\hat{\alpha}^\dagger \hat{\sigma}_{\mathrm{i}}(t) + (1 + \langle n \rangle)\hat{\sigma}_{\mathrm{i}}(t)\hat{\alpha}^\dagger \hat{\alpha}] +$$

$$iP \int d\varepsilon_\kappa \frac{g(\varepsilon_\kappa)|\gamma(\varepsilon_\kappa)|^2}{\varepsilon_\kappa - E}\{(1 + \langle n_\kappa \rangle)[\hat{\alpha}^\dagger \hat{\alpha}, \hat{\sigma}_{\mathrm{i}}(t)] + \langle n_\kappa \rangle[\hat{\sigma}_{\mathrm{i}}(t), \hat{\alpha}\hat{\alpha}^\dagger]\}, \tag{1.88}$$

with

$$\langle n \rangle = \frac{1}{e^{(E-\mu)/kT} - 1} \tag{1.89}$$

and $\Gamma = 2\pi g(E)|\gamma(E)|^2$.

Finally, we transform the Master equation (1.88) back to the Schrödinger picture

$$\sigma(t) = e^{-i\hat{H}_{\mathrm{s}}t}\hat{\sigma}_{\mathrm{i}}(t)e^{i\hat{H}_{\mathrm{s}}t}, \tag{1.90}$$

so we obtain the following equation

$$\frac{d}{dt}\hat{\sigma}(t) = -i\epsilon[\hat{\alpha}^\dagger \hat{\alpha}, \hat{\sigma}(t)] - \frac{\Gamma(1 + \langle n \rangle)}{2}[\hat{\alpha}^\dagger \hat{\alpha}\hat{\sigma}(t) + \hat{\sigma}(t)\hat{\alpha}^\dagger \hat{\alpha} - 2\hat{\alpha}\hat{\sigma}(t)\hat{\alpha}^\dagger] -$$

$$-\frac{\Gamma\langle n \rangle}{2}[\hat{\alpha}\hat{\alpha}^\dagger \hat{\sigma}(t) + \hat{\sigma}(t)\hat{\alpha}\hat{\alpha}^\dagger - 2\hat{\alpha}^\dagger \hat{\sigma}(t)\hat{\alpha}], \tag{1.91}$$

where

$$\epsilon = E - P \int \frac{g(\varepsilon_\kappa)|\gamma(\varepsilon_\kappa)|^2}{\varepsilon_\kappa - E} d\varepsilon_\kappa. \tag{1.92}$$

is the renormalized energy level of the site induced by the site-reservoir coupling.

Now, using the Master equation (1.91) we can calculate, for example, the evolution of the population in the site

$$\frac{d}{dt}\langle \hat{\alpha}^\dagger \hat{\alpha} \rangle \equiv \mathrm{Tr}_{\mathrm{s}}\{\hat{\alpha}^\dagger \hat{\alpha}\dot{\hat{\sigma}}\} = -\frac{\Gamma}{2}\langle \hat{\alpha}^\dagger \hat{\alpha} \rangle + \frac{\Gamma}{2}\langle n \rangle. \tag{1.93}$$

Assuming that initially the population in the dot was $\langle \hat{\alpha}^\dagger \hat{\alpha} \rangle_{t=0} = N$ then we have the following analytical solution

$$\langle \hat{\alpha}^\dagger \hat{\alpha} \rangle_t = (N - \langle n \rangle)e^{-\frac{\Gamma}{2}t} + \langle n \rangle. \tag{1.94}$$

The result (1.94) tell us that finally the dot will relax to an equilibrium state with the same temperature T and chemical potential μ as the reservoir:

$$\langle \hat{\alpha}^\dagger \hat{\alpha} \rangle_{t \to \infty} = \langle n \rangle = \frac{1}{e^{(E-\mu)/kT} - 1}. \tag{1.95}$$

We finish this subsection with an observation. In the Master equation (1.91) we can identify two types of Lindblad operators $\hat{L}_1 = \hat{\alpha}$ (second term in the right hand side) and $\hat{L}_2 = \hat{\alpha}^\dagger$ (third term in the right hand side). The physical meaning of these terms is simple. The second term in the right hand side of (1.91) destroys bosons with rate $\gamma_1 = \Gamma(1 + \langle n \rangle)$ while the third one creates bosons with rate $\gamma_2 = \Gamma \langle n \rangle$. The result of these two terms is the equilibrium state with $\langle n \rangle$ particles in our system.

Chapter 2

Open Optical Lattices: The Mean-Field Approximation and Beyond

Nowadays the experiments with Bose-Einstein condensation loaded in optical lattices can offer a remarkable level of control and single site manipulation. These advances open also new roads for theoretical investigation of systems that previously seemed unrealistic. In this chapter we introduce such a system, a one dimensional optical lattice filled with BEC that is subject to localized single particle losses.

This chapter is organized as follows. First, in section 2.1 we discuss a state of the art experiment that allows accurate control of single particle losses with single site resolution. In section 2.2 we introduce a theoretical model, based on the Master equation formalism, which can describe very well the experimental situation. Next, in section 2.3, we derive a mean-field approximation for the Master equation and we discuss the predictions for the dissipative double-well. Finally, in section 2.4, we introduce the Bogoliubov backreaction (BBR) method for open systems and we discuss its limits of validity. This method allows to study the dynamics of an open lattice beyond the mean-field approximation.

2.1 Experimental Motivation

The last decade the experimental control of ultracold atomic gases in optical lattices has made significant progress. The experimental parameters, such as the interatomic interactions and the tunneling between the sites, can be tuned to almost arbitrary values and also any dimensionality of the lattice
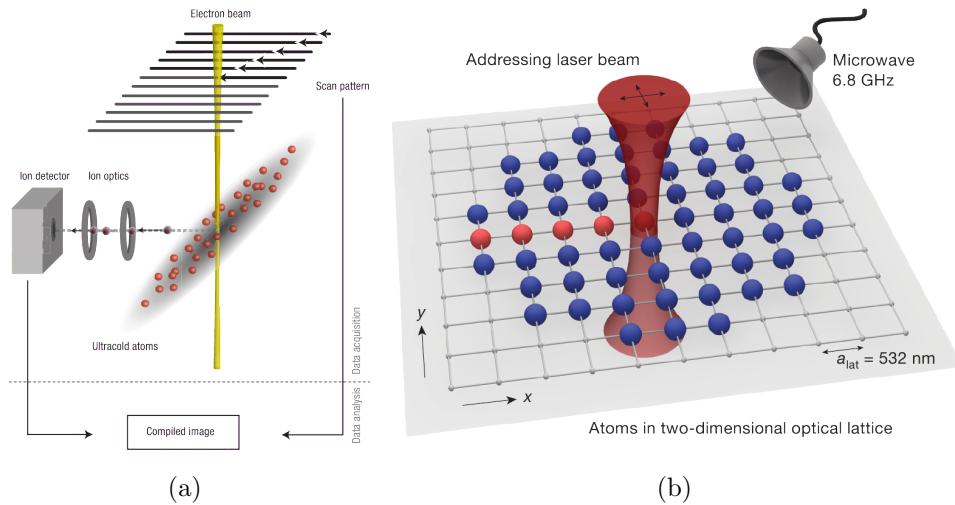
Figure 2.1: (a) *A strongly focused laser beam ionizes the atoms of a cloud. The ions are extracted by using ion optics and they are detected by an ion detector. Reprinted by permission from Macmillan Publishers Ltd:* [27], *copyright (2008).* (b) *Single site manipulation of atoms by using an off-resonant laser beam. Reprinted by permission from Macmillan Publishers Ltd:* [30], *copyright (2011).*

is possible. All these make the Bose-Hubbard model a powerful theoretical tool to describe real experiments. And indeed the theoretical prediction of the superfluid to Mott insulator quantum phase transition [15] has been experimentally achieved [16].

Recently, another interesting possibility became feasible: Local manipulation of individual lattice sites. Single-site access can be implemented optically either by increasing the lattice period [24, 25] or by a strongly focused laser beam [30] (for an illustration see figure 2.1 (b)). An even higher resolution can be achieved by a focused electron beam [26–28]. In the later case a focused electron beam locally produces ions in the atomic cloud, due to the electron-atom interaction. The produced ions are extracted and collected with the aid of ion optics and an ion detector (see figure 2.1 (a)). This detection procedure allows the reconstruction of the atoms position where the ionization occurred.

Let us discuss the electron microscopy case in more detail. In these experiment the vacuum chamber is equipted with an electron microscope, see figure 2.2 (a) and (b). After the preparation of a Bose-Einstein condensation the electron beam impact on it. The electron-atom collisions can ionize the atoms which subsequently are removed from the trap and detected by the ion
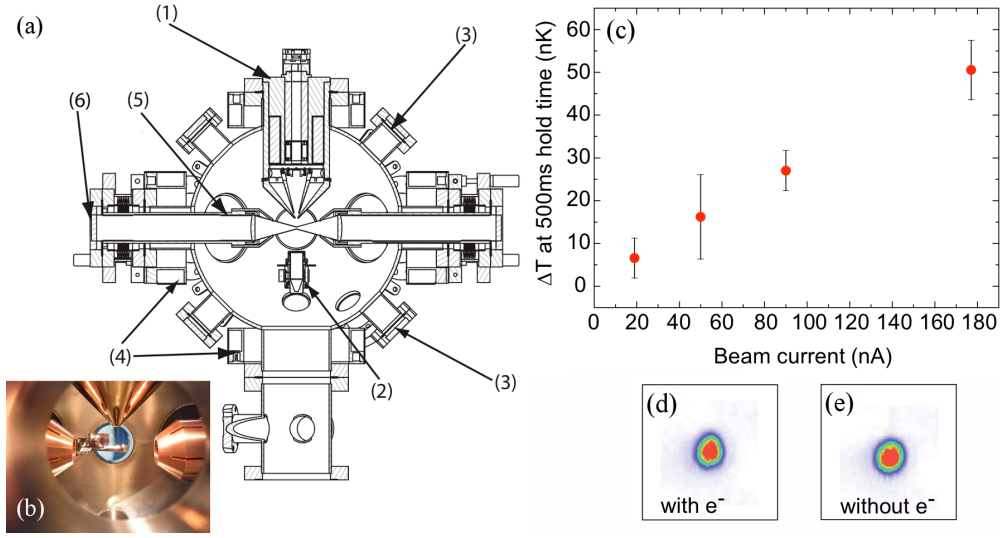
Figure 2.2: (a) *Sketch of the main experimental chamber as seen from the side, showing the electron column on top (1), as well as the Faraday cup (2) stopping the electron beam. Also, four of six viewports (3) and magnetic coils (4) forming the 3D-MOT are visible. Finally, the ZnSe-lens holders (5) and ZnSe-viewports (6) for the optical dipole trap are shown.* (b) *Photo of the main chamber's interior.* (c) *The temperature difference between an illuminated and a non-illuminated atom cloud after a holding time of 500 ms as a function of the electron beam current.* (d) *Absorption image of an illuminated BEC and* (e) *Absorption image of a BEC that has not been illuminated. Figure* (a) *is reprinted from* [26] *with kind permission from Springer Science and Business Media. Figures* (b)-(e) *are reprinted from* [28] *with the permission of Prof. Dr. Herwig Ott.*

detector. The ionized atoms are about 40% of all the scattered atoms. These ions, while leaving from the trap, can collide with other atoms producing more losses. We furthermore have about 55% inelastic scattering events and 5% elastic, which cannot produce a detectable signal.

As we described it above, we can say that this system is a *special* case of an open quantum system. It is an open system (since we lose atoms) in which we can accurately control the environment. We can remove single atoms from the position we want with the desired rate. This is already interesting since usually a dissipation process is connected with an uncontrollable environment, as we discussed in section 1.4. Furthermore, as we are going to argue, the "side effects" of the electron impact on the cloud are negligible. In figures 2.2 (c)-(e) we have experimental data [27], which show the effect of heating of the atomic cloud due to the impact of the electrons. Figure 2.2

(c) shows the temperature gained by the atomic cloud for different electron beam currents. As one can see, for an electron beam current of 20 nA the temperature of the sample increases only by 6 nK as compared to an initial temperature of typically around 100 nk. So in a very good approximation, the only effect of the electron beam on the Bose-Einstein condensation is the loss of atoms. This is further illustrated in figures 2.2 (d,e) where we have the absorption images of an illuminated atomic cloud, figure 2.2 (d), and a cloud that has not been illuminated, figure 2.2 (e). The only significant difference between the two images is that the atom number has been reduced by 7%.

2.2 The Dissipative Bose-Hubbard Model

The above discussion will help us to construct a realistic theoretical model which will describe the state of the art experiments. We want to study the dynamics of a Bose-Einstein condensation in an optical lattice which is subjected in localized single particle losses. We assume that the lattice is sufficiently deep, such that the dynamics takes place only in the lowest Bloch band, thus the assumptions for the Bose-Hubbard model hold. In section 2.1 we saw that the only important effect of the impact of the electron beam on the atomic gas is the single particle loss. The ionized atoms are leave the lattice and also subsequent particle losses are independent of each other. In other words we have the perfect Markovian environment, an environment without memory at all. These arguments leads us to write the following Master equation in Lindblad form [22, 62–67]

$$\frac{d}{dt}\hat{\rho}(t) = -i[\hat{H}, \hat{\rho}(t)] + \mathcal{L}_{\text{loss}}\hat{\rho}, \qquad (2.1)$$

where $\hat{H}$ is the Bose-Hubbard Hamiltonian (1.57) and have defined the Liouvillian

$$\mathcal{L}_{\text{loss}}\hat{\rho}(t) = -\sum_{j=1}^{M} \frac{\gamma_j}{2}(\hat{\alpha}_j^\dagger\hat{\alpha}_j\hat{\rho}(t) + \hat{\rho}(t)\hat{\alpha}_j^\dagger\hat{\alpha}_j - 2\hat{\alpha}_j\hat{\rho}(t)\hat{\alpha}_j^\dagger), \qquad (2.2)$$

with γ_j we have denoted the loss rate at site j, since the electron beam can be focused with single-site resolution [27].

In this model one can include also other terms that describe different dissipation processes, like two-body or three body losses [53, 60]. One important dissipation process is phase noise. Phase noise is the result of the elastic collisions of the atoms of the condensate with the atoms of the background gas [49–51] or the absorption and spontaneous emission of photons from the
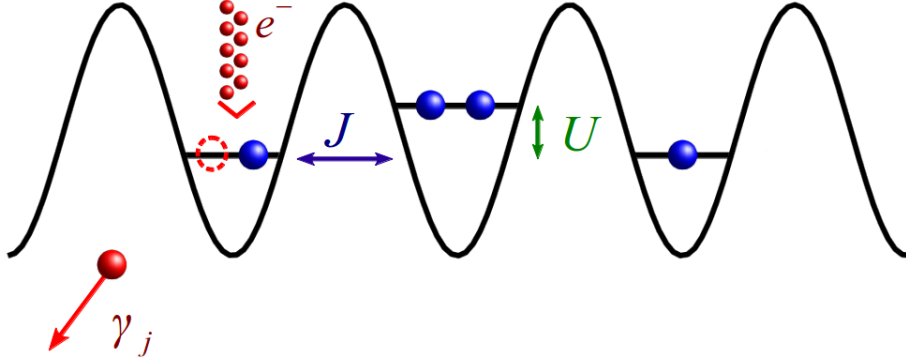
Figure 2.3: *Sketch of a dissipative Bose-Hubbard chain.*

lattice beams [52]. It effectively heats the system but leaves the particle number invariant. This process can be described by the following term in the Master equation

$$\mathcal{L}_{\text{noise}}\hat{\rho}(t) = -\frac{\kappa}{2}\sum_{j}(\hat{n}_j^2\hat{\rho}(t) + \hat{\rho}(t)\hat{n}_j^2 - 2\hat{n}_j\hat{\rho}(t)\hat{n}_j),\tag{2.3}$$

where $\hat{n}_j = \hat{\alpha}_j^\dagger\hat{\alpha}_j$ are the number operators and κ is the rate of phase noise. Phase noise is always present in the experiments, but can be made very small, e.g., by detuning the optical lattice far from the atomic resonance, so one can ignore it.

In order to understand better how single particle losses affects the dynamics of the system, we derive from the Master equation (2.1) the evolution equations for the single-particle density matrix elements $\sigma_{j,k} \equiv \langle\hat{\alpha}_j^\dagger\hat{\alpha}_k\rangle = \text{Tr}(\hat{\alpha}_j^\dagger\hat{\alpha}_k\hat{\rho})$:

$$\begin{aligned}
i\frac{d}{dt}\sigma_{j,k} &= \text{Tr}\{\hat{\alpha}_j^\dagger\hat{\alpha}_k[\hat{H},\hat{\rho}] + i\hat{\alpha}_j^\dagger\hat{\alpha}_k(\mathcal{L}_{\text{loss}} + \mathcal{L}_{\text{noise}})\hat{\rho}\}\\
&= (\varepsilon_k - \varepsilon_j)\sigma_{j,k} - J(\sigma_{j,k+1} + \sigma_{j,k-1} - \sigma_{j+1,k} - \sigma_{j-1,k})\\
&\quad + U(\sigma_{k,k}\sigma_{j,k} + \Delta_{jkkk} - \sigma_{j,j}\sigma_{j,k} - \Delta_{jjjk})\\
&\quad - i\frac{\gamma_j + \gamma_k}{2}\sigma_{j,k} - i\kappa(1 - \delta_{j,k})\sigma_{j,k},
\end{aligned}\tag{2.4}$$

where we have defined the variances

$$\Delta_{jk\ell m} = \langle\hat{\alpha}_j^\dagger\hat{\alpha}_k\hat{\alpha}_\ell^\dagger\hat{\alpha}_m\rangle - \langle\hat{\alpha}_j^\dagger\hat{\alpha}_k\rangle\langle\hat{\alpha}_\ell^\dagger\hat{\alpha}_m\rangle\tag{2.5}$$

and we have also included the phase noise term. The first and second term, in the right hand side of (2.4), are the tunneling and interaction terms respectively. The interaction term depends also on the four point correlation

functions, due to the due to the more than quadratic terms in the Hamiltonian. The final two terms are the dissipation terms. As one can easily see, the phase noise term (the last term) destroys all the coherences between the sites, $\langle \hat{\alpha}_j^\dagger \hat{\alpha}_k \rangle$, it is a decoherence process. From the other hand, the single-particle loss term does not reduce only the particle number in the leaky site $\langle \hat{\alpha}_j^\dagger \hat{\alpha}_j \rangle$, but also destroys all the coherences between the leaky site and the other sites. This allows us to use the localized single particle loss as a tool to control the coherences in our system. In the next chapters we discuss some interesting applications of this observation.

The Master equation (2.1) is a very hard problem to solve. Numerical exact solutions are only possible for small systems (see Appendix A), thus we need approximate methods. One well-known approximate method is the so-called truncated Wigner method, which we present in Appendix B. An equivalently hard problem to solve, as equation (2.1), is the system of equations (2.4). These equations are not forming a closed system of equations, due to the variances $\Delta_{jk\ell m}$, thus we have to include evolution equations for higher order correlations functions. In this way an infinite hierarchy of equations is formed, the so-called Bogoliubov-Born-Green-Kirkwood-Yvon (BBGKY) hierarchy

$$
\begin{aligned}
i\frac{d}{dt}\langle \hat{\alpha}_i^\dagger \hat{\alpha}_j \rangle &= f_1\left(\langle \hat{\alpha}_{i'}^\dagger \hat{\alpha}_{j'} \rangle, \langle \hat{\alpha}_{i'}^\dagger \hat{\alpha}_{j'} \hat{\alpha}_{k'}^\dagger \hat{\alpha}_{l'} \rangle \right) \\
i\frac{d}{dt}\langle \hat{\alpha}_i^\dagger \hat{\alpha}_j \hat{\alpha}_k^\dagger \hat{\alpha}_l \rangle &= f_2\left(\langle \hat{\alpha}_{i'}^\dagger \hat{\alpha}_{j'} \hat{\alpha}_{k'}^\dagger \hat{\alpha}_{l'} \rangle, \langle \hat{\alpha}_{i'}^\dagger \hat{\alpha}_{j'} \hat{\alpha}_{k'}^\dagger \hat{\alpha}_{l'} \hat{\alpha}_{m'}^\dagger \hat{\alpha}_{n'} \rangle \right) \qquad (2.6) \\
i\frac{d}{dt}\langle \hat{\alpha}_i^\dagger \hat{\alpha}_j \hat{\alpha}_k^\dagger \hat{\alpha}_l \hat{\alpha}_m^\dagger \hat{\alpha}_n \rangle &= f_3\left(\langle \hat{\alpha}_{i'}^\dagger \hat{\alpha}_{j'} \hat{\alpha}_{k'}^\dagger \hat{\alpha}_{l'} \hat{\alpha}_{m'}^\dagger \hat{\alpha}_{n'} \rangle, \langle \hat{\alpha}_{i'}^\dagger \hat{\alpha}_{j'} \hat{\alpha}_{k'}^\dagger \hat{\alpha}_{l'} \hat{\alpha}_{m'}^\dagger \hat{\alpha}_{n'} \hat{\alpha}_{e'}^\dagger \hat{\alpha}_{g'} \rangle \right) \\
&\vdots
\end{aligned}
$$

where f_1, f_2, f_3, ... are functions which increase in complexity with the order. An exact solution of the problem, in this form, is only possible when there are no interactions, otherwise we have to solve an infinite system of equation. However, equations (2.6) can be the starting point for approximations. In the next two sections we discuss how we can derive a mean-field approximation and how we can go beyond.

2.3 The Mean-Field Approximation

The mean-field approximation refers to the limit where $N \to \infty$ with $g = UN = $ const. In other words the nonlinearity must be negligible, thus the

four-point correlation functions can be written

$$\langle \hat{\alpha}_j^\dagger \hat{\alpha}_k \hat{\alpha}_\ell^\dagger \hat{\alpha}_m \rangle \approx \langle \hat{\alpha}_j^\dagger \hat{\alpha}_k \rangle \langle \hat{\alpha}_\ell^\dagger \hat{\alpha}_m \rangle \tag{2.7}$$

or

$$\Delta_{jk\ell m} \approx 0, \tag{2.8}$$

since the Hamiltonian will be approximately quadratic. With this assumption equations (2.4) can be written as a closed system [58, 59, 64, 65]

$$
\begin{aligned}
i\frac{d}{dt}\sigma_{j,k} &= (\varepsilon_k - \varepsilon_j)\sigma_{j,k} - J(\sigma_{j,k+1} + \sigma_{j,k-1} - \sigma_{j+1,k} - \sigma_{j-1,k}) \\
&\quad + U(\sigma_{k,k}\sigma_{j,k} - \sigma_{j,j}\sigma_{j,k}) \\
&\quad - i\frac{\gamma_j + \gamma_k}{2}\sigma_{j,k} - i\kappa(1 - \delta_{j,k})\sigma_{j,k}.
\end{aligned}
\tag{2.9}
$$

The above approximation is appropriate only for a pure condensate

$$|\Psi^{(N)}\rangle = \frac{1}{\sqrt{N!}} \left(\sum_{j=1}^M \psi_j \hat{\alpha}_j^\dagger \right)^N |0\rangle, \tag{2.10}$$

since the variances $\Delta_{jk\ell m}$ scale linearly with the particle number N, while the products $\sigma_{j,k}\sigma_{\ell,m}$ scale as N^2. Indeed the two-point correlation functions for the state (2.10) gives

$$\langle \hat{\alpha}_j^\dagger \hat{\alpha}_k \rangle = \langle \Psi^{(N)} | \hat{\alpha}_j^\dagger \hat{\alpha}_k | \Psi^{(N)} \rangle = N\psi_j^* \psi_k \tag{2.11}$$

while the four-point correlation functions

$$
\begin{aligned}
\langle \hat{\alpha}_j^\dagger \hat{\alpha}_k \hat{\alpha}_\ell^\dagger \hat{\alpha}_m \rangle &= \langle \Psi^{(N)} | \hat{\alpha}_j^\dagger \hat{\alpha}_k \hat{\alpha}_\ell^\dagger \hat{\alpha}_m | \Psi^{(N)} \rangle \\
&= N(N-1)\psi_j^* \psi_k \psi_\ell^* \psi_m + N\psi_j^* \psi_m \delta_{kl}.
\end{aligned}
\tag{2.12}
$$

If we neglect the phase noise term in (2.9), $\kappa = 0$, then these equations are equivalent to the non-Hermitian discrete nonlinear Schrödinger equation

$$i\frac{d}{dt}\psi_k = (\varepsilon_k - \varepsilon_j)\psi_k - J(\psi_{k+1} + \psi_{k-1}) + U|\psi_k|^2\psi_k - i\frac{\gamma_k}{2}\psi_k \tag{2.13}$$

by the identification $\sigma_{j,k} = \psi_j^* \psi_k$. In this way we derived the non-Hermitian Schrödinger equation which has previously been used heuristically [54–56].

2.3.1 The Double Well in the Mean-Field Approximation

$\mathcal{T}$he dissipative dynamics of a simple system, such as the leaky double well, already present a very interesting behavior. For this system, it is convenient to use the so-called Bloch representation

$$
\begin{aligned}
\hat{L}_x &= \frac{1}{2}(\hat{\alpha}_1^\dagger \hat{\alpha}_2 + \hat{\alpha}_2^\dagger \hat{\alpha}_1), \\
\hat{L}_y &= \frac{i}{2}(\hat{\alpha}_1^\dagger \hat{\alpha}_2 - \hat{\alpha}_2^\dagger \hat{\alpha}_1), \\
\hat{L}_z &= \frac{1}{2}(\hat{\alpha}_2^\dagger \hat{\alpha}_2 - \hat{\alpha}_1^\dagger \hat{\alpha}_1),
\end{aligned}
\tag{2.14}
$$

which form an angular-momentum algebra *SU(2)* with quantum number $\ell = N/2$ [37, 40, 41, 58, 59, 64, 65, 97, 98], with N the particle number. With the help of the above operators we can rewrite the Bose-Hubbard Hamiltonian (1.57) in the form

$$
\hat{H} = -2J\hat{L}_x + 2\varepsilon\hat{L}_z + U\hat{L}_z^2
\tag{2.15}
$$

up to terms only depending on the total particle number and we have defined the parameter $\varepsilon = \varepsilon_2 - \varepsilon_1$.

Now we can translate the mean-field equations (2.9), in equations for the expectation values of the angular-momentum operators $\mathbf{s} = (s_x, s_y, s_z) \equiv 2(\text{Tr}\{\hat{L}_x\hat{\rho}\}, \text{Tr}\{\hat{L}_y\hat{\rho}\}, \text{Tr}\{\hat{L}_z\hat{\rho}\})$ [64, 65]

$$
\begin{aligned}
\dot{s}_x &= -2\varepsilon s_y - U s_y s_z - \left(\frac{\gamma_1 + \gamma_2}{2} + \kappa\right) s_x, \\
\dot{s}_y &= 2J s_z + 2\varepsilon s_x + U s_x s_z - \left(\frac{\gamma_1 + \gamma_2}{2} + \kappa\right) s_y, \\
\dot{s}_z &= -2J s_y - \frac{\gamma_1 + \gamma_2}{2} s_z - \frac{\gamma_2 - \gamma_1}{2} n, \\
\dot{n} &= -\frac{\gamma_1 + \gamma_2}{2} n - \frac{\gamma_2 - \gamma_1}{2} s_z,
\end{aligned}
\tag{2.16}
$$

where $n = \text{Tr}\{(\hat{n}_1 + \hat{n}_2)\hat{\rho}\}$ is the total particle number. Moreover, we write the initial conditions (2.10) with the help of two parameters

$$
|\Psi^{(N)}\rangle = \frac{1}{\sqrt{N!}}\left(\sqrt{p}\,\hat{\alpha}_1^\dagger + \sqrt{1-p}\,e^{iq}\,\hat{\alpha}_2^\dagger\right)^N |0\rangle,
\tag{2.17}
$$

where p is the fraction of particles in the first well and q is the relative phase between the wells.

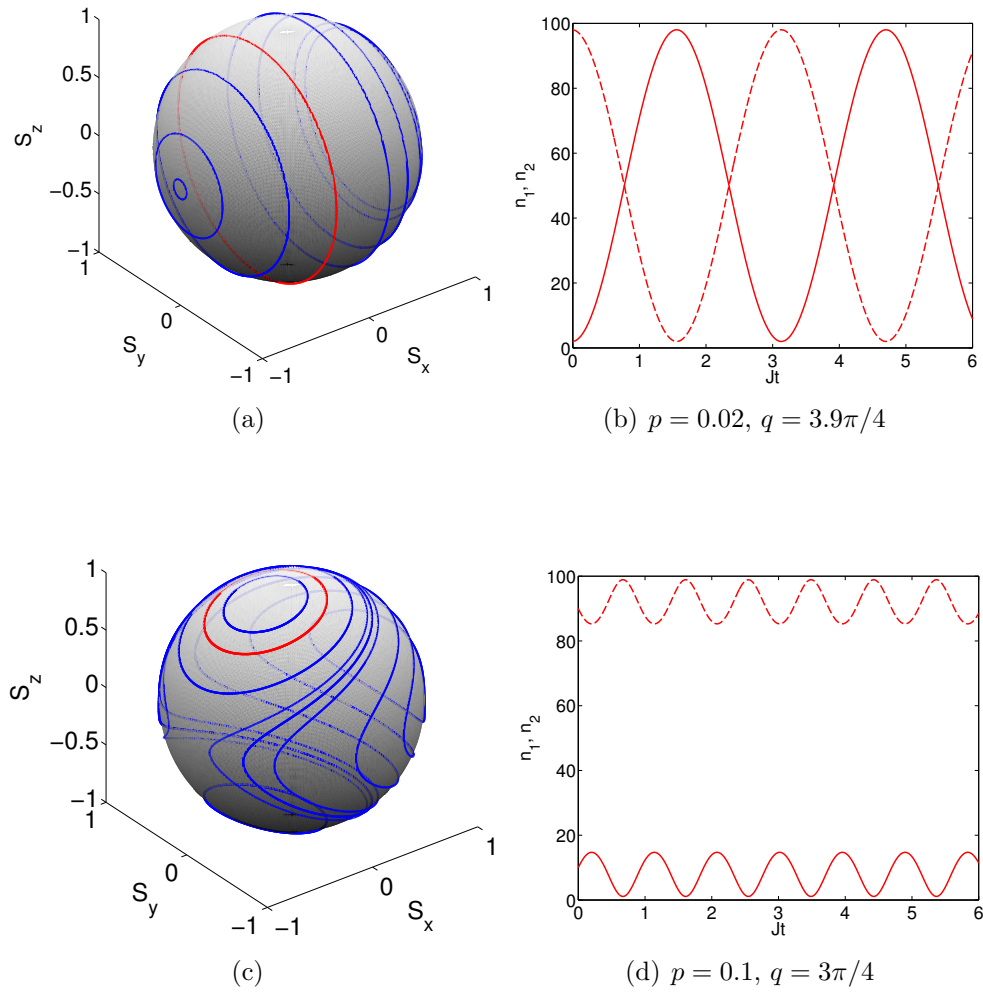Figure 2.4: *Non-dissipative Bloch sphere dynamics* (a) *in the noninteracting case and* (c) *in the strongly interacting case* $Un(0) = 8J$. *(b,d) Evolution of the particle number in the first (dashed line) and in the second (solid line) well which corresponds in the red line on the Bloch sphere. The blue lines in (a,c) correspond to trajectories of different initial states. The initial particle number is* $N = 100$.

The non-dissipative case [25, 37, 38], $\gamma_1 = \gamma_2 = \kappa = 0$, will help us to understand the physics for the open system. In figures 2.4 (a,b) we have plotted the dynamics of the Bloch vector $\mathbf{S} = \mathbf{s}/n$ and the population in each well for the noninteracting system, $U = 0$. In this case we observe the so-called Josephson oscillations. We have complete oscillations between the two wells. The structure of the Bloch sphere (which is the classical phase space for the system) is simple, two elliptic fixed points. From the other hand, in the strongly interacting case $Un(0) = 8J$, figures 2.4 (c,d), the coherent oscillations are significantly suppressed. This is the so-called self-trapping effect. An intuitive understanding can come from an energy argument: the well with the larger population has very high energy, in comparison with the other well, so the two sites are out of resonance. As a result the tunneling is suppressed. In the Bloch sphere we see that the one elliptic fixed point, of the noninteracting case, bifurcates in two elliptic and one saddle point.

The dynamics changes in the presence of particle losses. In figure 2.5 we have the dynamics in a double well with dissipation only in the first well $\gamma_1 = 1J$, for different initial conditions. The dynamics of the Bloch vector, figures 2.5 (a,c), shows that the trajectories from both up and down hemisphere are attracted by one fixed point. Figures 2.5 (b,d) depict the evolution of the populations in the two wells for the red trajectories on the Bloch spheres. For the trajectory which begins from the upper hemisphere ($n_1(0) = 20$ and $n_2(0) = 80$), we can see that the population in the second well initially oscillates but then it almost saturates ($n_2(t_{\text{fin.}}) \approx 80$), while the population in the first well goes to zero. From the other hand, the trajectory which begins from the lower hemisphere ($n_1(0) = 70$ and $n_2(0) = 30$), shows that the population in the second well increases and then saturates ($n_2(t_{\text{fin.}}) \approx 40$), while again the population in the first well goes to zero. In general, almost for all initial states the system ends up with an almost stable population in the second well and an empty first well. In other words, the upper elliptic fixed point in figure 2.4 (c) becomes attractive, while the lower becomes repulsive. Here we must note that one observes such behavior only if the interaction strength is strong enough to induce self-trapping.

Finally, in figure 2.6 we compare the mean-field approximation with exact numerical results. While the behavior of the occupation numbers, figure 2.6 (b), is well described by the mean-field approximation, one observes significant deviations from the exact results for the Bloch vector, $\mathbf{S}(t)$. The mean-field approximation overestimates the oscillations of the components of $\mathbf{S}(t)$, since it cannot take into account the decoherence of the BEC.

(a)

(b) $p = 0.2$, $q = 0.8\pi$

(c)

(d) $p = 0.7$, $q = 0.8\pi$

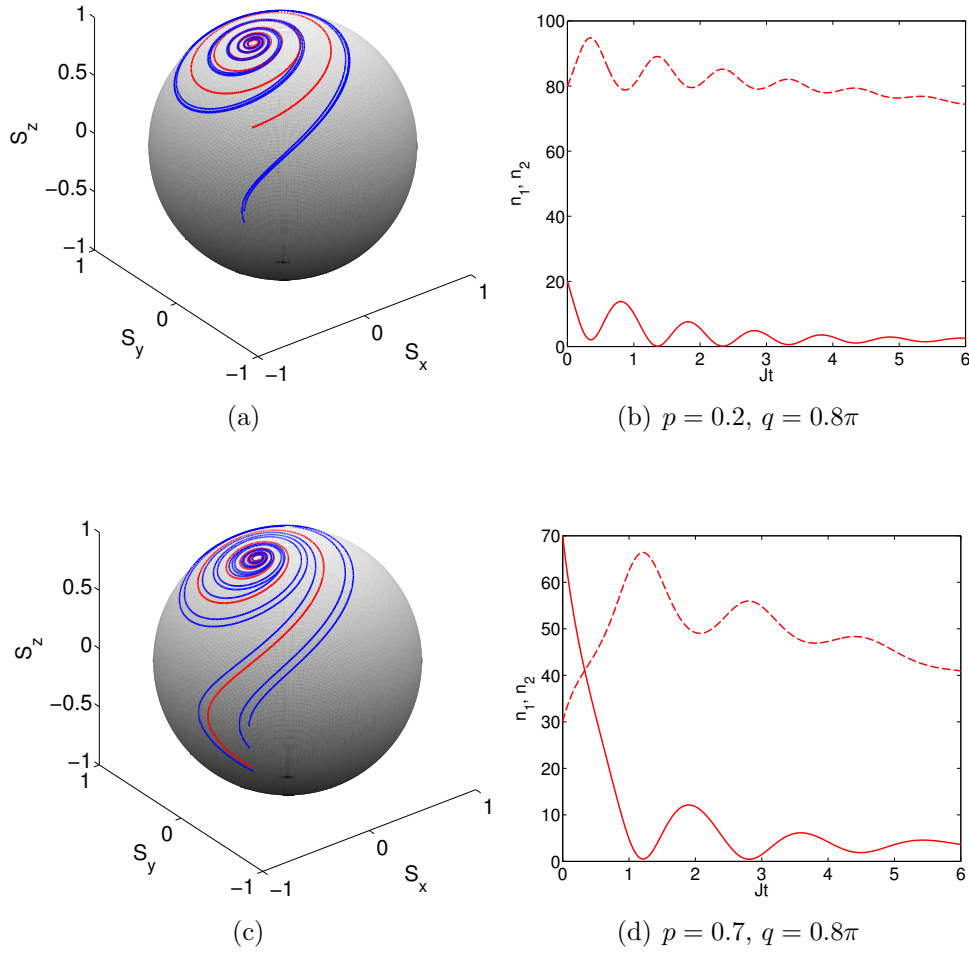Figure 2.5: (a), (c) *dissipative Bloch sphere dynamics in the strongly inter-acting case $Un(0) = 8J$ for $\gamma_1 = 1J$ and $\gamma_2 = 0$. (b,d) Evolution of the particle number in the first (dashed line) and in the second (solid line) well which corresponds in the red line on the Bloch sphere. The blue lines in (a,c) correspond to trajectories of different initial states. The initial particle number is $N = 100$.*
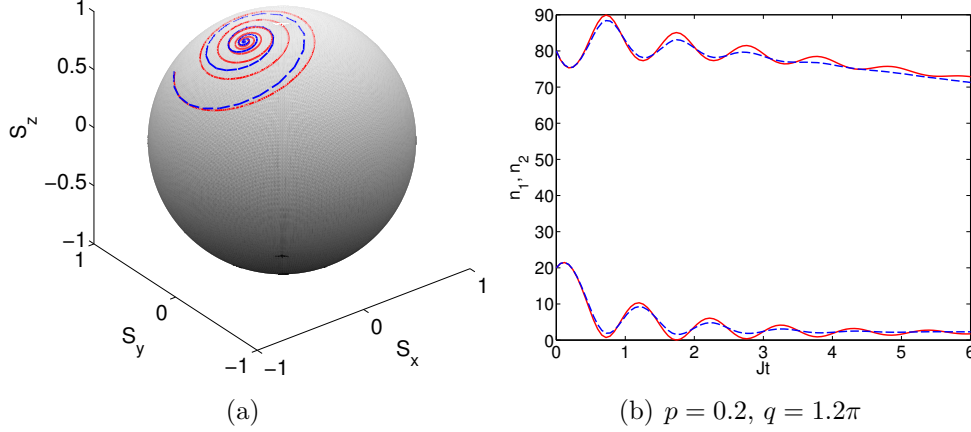
Figure 2.6: *Comparison between the mean-field approximation (red solid line) and the numerical exact quantum jump method (blue dashed line) averaging over 200 trajectories. Shown are* (a) *the Bloch vector dynamics and* (b) *the particle number in the first and second well. The parameters are* $Un(0) = 8J$, $\gamma_1 = 1J$, $\gamma_2 = 0$ *and* $\kappa = 0$. *The initial particle number is* $N = 100$.

2.4   The Generalized BBR method

The mean-field approximation assumes a pure condensate and is strictly valid in the limit $N \to \infty$. In order to explore many-body effects, like the depletion of the BEC, one should go beyond the mean-field limit. Here we generalize the Bogoliubov back-reaction (BBR) method [40, 41] to the dissipative case. In this approximation one takes into account also the four-point correlation functions, or equivalently the variances (2.5), explicitly. This method gives accurate predictions for large, but finite particle numbers, and for a system close to a pure BEC state.

Let us start with the coherent part of the evolution equations for the

four-point correlation functions

$$
\begin{aligned}
\frac{d}{dt}\langle\hat{\alpha}_j^\dagger\hat{\alpha}_k\hat{\alpha}_\ell^\dagger\hat{\alpha}_m\rangle =& \ \mathrm{Tr}\{\hat{\alpha}_j^\dagger\hat{\alpha}_k\hat{\alpha}_\ell^\dagger\hat{\alpha}_m[\hat{H},\hat{\rho}]\}\\
=& \ (\varepsilon_k+\varepsilon_m-\varepsilon_j-\varepsilon_\ell)\langle\hat{\alpha}_j^\dagger\hat{\alpha}_k\hat{\alpha}_\ell^\dagger\hat{\alpha}_m\rangle\\
& -J(\langle\hat{\alpha}_j^\dagger\hat{\alpha}_k\hat{\alpha}_\ell^\dagger\hat{\alpha}_{m+1}\rangle+\langle\hat{\alpha}_j^\dagger\hat{\alpha}_k\hat{\alpha}_\ell^\dagger\hat{\alpha}_{m-1}\rangle+\langle\hat{\alpha}_j^\dagger\hat{\alpha}_{k+1}\hat{\alpha}_\ell^\dagger\hat{\alpha}_m\rangle\\
& +\langle\hat{\alpha}_j^\dagger\hat{\alpha}_{k-1}\hat{\alpha}_\ell^\dagger\hat{\alpha}_m\rangle-\langle\hat{\alpha}_{j+1}^\dagger\hat{\alpha}_k\hat{\alpha}_\ell^\dagger\hat{\alpha}_m\rangle-\langle\hat{\alpha}_{j-1}^\dagger\hat{\alpha}_k\hat{\alpha}_\ell^\dagger\hat{\alpha}_m\rangle\\
& -\langle\hat{\alpha}_j^\dagger\hat{\alpha}_k\hat{\alpha}_{\ell+1}^\dagger\hat{\alpha}_m\rangle-\langle\hat{\alpha}_j^\dagger\hat{\alpha}_k\hat{\alpha}_{\ell-1}^\dagger\hat{\alpha}_m\rangle)\\
& +U(\langle\hat{\alpha}_j^\dagger\hat{\alpha}_k\hat{n}_k\hat{\alpha}_\ell^\dagger\hat{\alpha}_m\rangle+\langle\hat{\alpha}_j^\dagger\hat{\alpha}_k\hat{\alpha}_\ell^\dagger\hat{\alpha}_m\hat{n}_m\rangle\\
& -\langle\hat{n}_j\hat{\alpha}_j^\dagger\hat{\alpha}_k\hat{\alpha}_\ell^\dagger\hat{\alpha}_m\rangle-\langle\hat{\alpha}_j^\dagger\hat{\alpha}_k\hat{n}_\ell\hat{\alpha}_\ell^\dagger\hat{\alpha}_m\rangle) \qquad (2.18)
\end{aligned}
$$

The interaction term involves a six-point correlation function, so to obtain a closed set of equations we use the following truncation [39]

$$
\begin{aligned}
\langle\hat{\alpha}_j^\dagger\hat{\alpha}_k\hat{\alpha}_\ell^\dagger\hat{\alpha}_m\hat{\alpha}_r^\dagger\hat{\alpha}_s\rangle \approx& \ \langle\hat{\alpha}_j^\dagger\hat{\alpha}_k\hat{\alpha}_\ell^\dagger\hat{\alpha}_m\rangle\langle\hat{\alpha}_r^\dagger\hat{\alpha}_s\rangle+\langle\hat{\alpha}_j^\dagger\hat{\alpha}_k\hat{\alpha}_r^\dagger\hat{\alpha}_s\rangle\langle\hat{\alpha}_\ell^\dagger\hat{\alpha}_m\rangle \qquad (2.19)\\
& +\langle\hat{\alpha}_\ell^\dagger\hat{\alpha}_m\hat{\alpha}_r^\dagger\hat{\alpha}_s\rangle\langle\hat{\alpha}_j^\dagger\hat{\alpha}_k\rangle-2\langle\hat{\alpha}_j^\dagger\hat{\alpha}_k\rangle\langle\hat{\alpha}_\ell^\dagger\hat{\alpha}_m\rangle\langle\hat{\alpha}_r^\dagger\hat{\alpha}_s\rangle.
\end{aligned}
$$

For a pure Bose-Einstein condensation, described by the state (2.10), the six point correlation function scales as N^3, while the error introduced by the truncation (2.19) increases linearly with N. So the relative error induced by this truncation vanishes as $1/N^2$ with increasing particle number. Thus, the BBR method provides a better description of the many-body dynamics than the simple mean-field approximation, since it includes higher order correlation functions at least approximately.

However, there is an important restriction. The method works good only if we are close to a pure BEC state. If we have significant depletion of the condensate mode the method breaks down [41]. Indeed the hierarchy truncation we have done is a systematic perturbative approximation, but it is state dependent. That is, the perturbative parameter is small only for a special class of states. For the Bose-Einstein condensation case we can use as a small parameter the quantity $e = 1 - \lambda_0/n_{\mathrm{tot}}$, where λ_0 is the larger eigenvalue of the SPDM, since for a BEC we have $\lambda_0/n_{\mathrm{tot}} \approx 1$. To zeroth order the BEC is by definition pure, thus we obtain the mean field approximation we discussed in subsection 2.3.1. The next order in e can be achieved if we truncate the BBGKY hierarchy (2.7) at one order higher. We take

$$
\hat{\alpha}_j^\dagger\hat{\alpha}_k = \sigma_{j,k} + \hat{\delta}\sigma_{j,k}, \qquad (2.20)
$$

where $\sigma_{j,k}/n_{\mathrm{tot}}$ is $\mathcal{O}(1)$ and all the matrix elements of $\hat{\delta}\sigma_{j,k}/n_{\mathrm{tot}}$ remain smaller than $\mathcal{O}(e^{1/2})$. The variances $\Delta_{jk\ell m}/n_{\mathrm{tot}}^2$ will be of order e. Thus, when e becomes large the entire perturbation approach fails.

Using the truncation (2.19), the coherent part of the dynamics is given by

$$
\begin{aligned}
i\frac{d}{dt}\Delta_{jk\ell m} &= -J[\Delta_{j,k,\ell,m+1} + \Delta_{j,k,\ell,m-1} + \Delta_{j,k+1,\ell,m} + \Delta_{j,k-1,\ell,m} \\
&\quad -\Delta_{j,k,\ell+1,m} - \Delta_{j,k,\ell-1,m} - \Delta_{j+1,k,\ell,m} - \Delta_{j-1,k,\ell,m}] \\
&\quad +U[\Delta_{kk\ell m}\sigma_{jk} - \Delta_{jj\ell m}\sigma_{jk} + \Delta_{jkmm}\sigma_{\ell m} - \Delta_{jk\ell\ell}\sigma_{\ell m} \\
&\quad +\Delta_{jk\ell m}(\sigma_{kk} + \sigma_{mm} - \sigma_{\ell\ell} - \sigma_{jj})].
\end{aligned}
\tag{2.21}
$$

Particle loss and phase noise terms affect the dynamics of the four-point correlation function as follows

$$
\begin{aligned}
\frac{d}{dt}\langle \hat{\alpha}_j^\dagger \hat{\alpha}_k \hat{\alpha}_\ell^\dagger \hat{\alpha}_m \rangle &= \mathrm{Tr}\{\hat{\alpha}_j^\dagger \hat{\alpha}_k \hat{\alpha}_\ell^\dagger \hat{\alpha}_m (\mathcal{L}_{\mathrm{loss}} + \mathcal{L}_{\mathrm{noise}})\hat{\rho}\} \\
&= -\frac{\gamma_j + \gamma_k + \gamma_\ell + \gamma_m}{2}\langle \hat{\alpha}_j^\dagger \hat{\alpha}_k \hat{\alpha}_\ell^\dagger \hat{\alpha}_m \rangle + \gamma_k \langle \hat{\alpha}_j^\dagger \hat{\alpha}_m \rangle \delta_{k\ell} \\
&\quad -\kappa(2 + \delta_{km} + \delta_{j\ell} - \delta_{jk} - \delta_{jm} - \delta_{k\ell} - \delta_{\ell m}) \\
&\quad \times \langle \hat{\alpha}_j^\dagger \hat{\alpha}_k \hat{\alpha}_\ell^\dagger \hat{\alpha}_m \rangle.
\end{aligned}
\tag{2.22}
$$

In terms of the variances we have

$$
\begin{aligned}
\frac{d}{dt}\Delta_{jk\ell m} &= -\frac{\gamma_j + \gamma_k + \gamma_\ell + \gamma_m}{2}\Delta_{jk\ell m} + \gamma_k \sigma_{jm}\delta_{k\ell} \\
&\quad -\kappa(\delta_{km} + \delta_{j\ell} - \delta_{jm} - 2\delta_{k\ell})(\Delta_{jk\ell m} + \sigma_{jk}\sigma_{\ell m}) \\
&\quad -\kappa(2 - \delta_{jk} - \delta_{\ell m})\Delta_{jk\ell m}.
\end{aligned}
\tag{2.23}
$$

Although, the BBR method works if we are close to a pure BEC state, it can give very important informations about the system, which are not accessible by the mean-field approximation. In particular, it accurately predicts the onset of the depletion of the condensate mode. The number of atoms in this mode is given by the leading eigenvalue λ_0 of the SPDM σ_{jk}. The ratio $\lambda_0/n_{\mathrm{tot.}}$ is referred as the condensate fraction [4, 40, 41].

The validity of the BBR method has been already discussed in detail for closed systems [39]. Here we will test the method in the presence of dissipation. In figure 2.7 we have two examples of the dynamics of a BEC in a leaky double-well, comparing the BBR method (solid blue line) with numerical exact results of the quantum jump method (thick red line). As an initial state we have used a pure BEC with equal population and a phase of π between the wells. For strong dissipation, figure 2.7 (b), the BBR method predicts accurately the evolution of the total population $n_{tot} = \langle \hat{n}_1 + \hat{n}_2 \rangle$. Significant differences are observed for weak dissipation, figure 2.7 (a). In other words single particle losses improves the BBR method. This is further
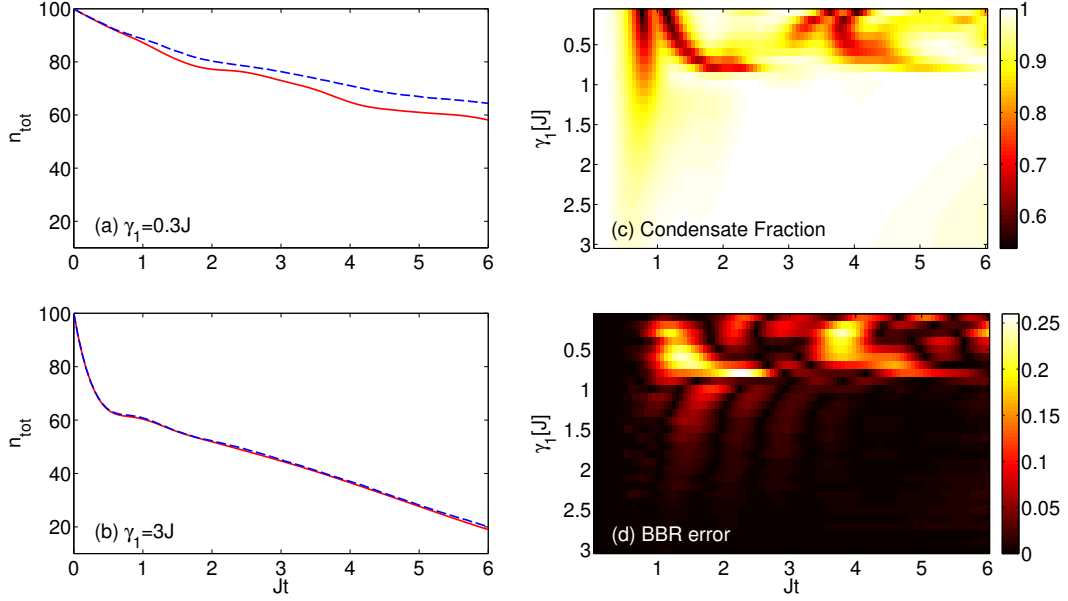
Figure 2.7: *Numerical test of the BBR method for a leaky double-well trap with loss in the first well. (a,b) Dynamics of the total particle number n_{tot} for two different values of the loss rate, comparing the BBR approximation (solid red line) with the quantum jump method (dashed blue line). (c) Condensate fraction, λ_0/n_{tot}, as a function of time and the loss rate, γ_1. (d) Trace distance (2.24) between the exact rescaled SPDM $\sigma(t)/n(t)$ and the respective BBR approximation. Initially we assume a pure BEC with equal population and phase difference of π between the sites. The remaining parameters are $U = 0.09J$, $\kappa = 0$ and $n(0) = 100$ atoms.*

illustrated in figure 2.7 (d), where we have plotted the trace distance of the exact rescaled SPDM and the rescaled SPDM obtained by the BBR method,

$$D := \frac{1}{2}\text{Tr}\left\{\left|\frac{\sigma_{\text{BBR}}}{n_{\text{BBR}}} - \frac{\sigma_{\text{ex.}}}{n_{\text{ex.}}}\right|\right\} \qquad (2.24)$$

as a function of time and for different dissipation rates γ_1. For sufficiently strong losses, we observe that D almost vanishes for all times. Thus in this regime the BBR method gives accurate predictions of the quantum dynamics. A hint why this happens we can see in figure 2.7 (c), where we have the condensate fraction as a function of time for different values of γ_1. As one can see the BEC tends to remain pure for strong losses for all times. However, this means that the performance of the BBR method is expected to be accurate.

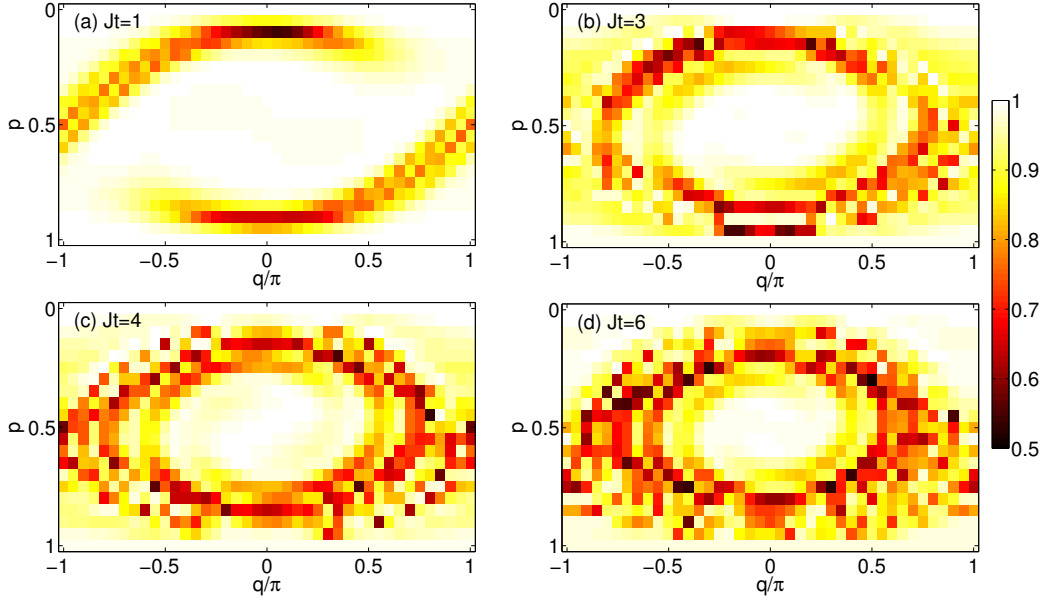The BBR method is a state depended perturbative approximation, so it

Figure 2.8: *The condensate fraction λ_0/n_{tot} at different time instants scanning the initial state's parameters p and q. The parameters are $U = 0.09J$, $\gamma_1 = 0.1J$, $\kappa = 0$ and $n(0) = 100$.*

is important to understand how the initial state affects the predictions of the method. In figure 2.8 we are scanning the initial state's parameters $p \in [0, 1]$ and $q \in [-\pi, \pi]$ and depict how the condensate fraction λ_0/n_{tot} behaves at different time instants. We have chosen weak particle losses, $\gamma_1 = 0.1J$, since the depletion of the condensate mode is expected to be more intense. As one can see in only three cases we have a pure BEC at all times: (i) around $p = 0.5$ and $q = 0$, (ii) for $p = 0$ and (iii) for $p = 1$. The later two cases are trivial since in case (ii) there are no particles in the first well, where losses occur, so the particles remain in the second due to the self trapping, and in case (iii) all the particles are in the first well so all of them will leave the trap. In case (i) we have initial states around the symmetric state

$$|\Psi^{(N)}\rangle = \frac{1}{\sqrt{N!}} \left(\hat{\alpha}_1^\dagger + \hat{\alpha}_2^\dagger \right)^N |0\rangle \qquad (2.25)$$

where we have equal populations in the two wells and zero phase difference between them. The symmetric state corresponds to an elliptic fixed point in the non-dissipative classical phase space on the Bloch sphere (see for example figure 2.4 (c)), that is why the BEC remains almost pure in the whole evolution. For the antisymmetric state, $p = 0.5$, $q = \pi$, we observe that we have a fast depletion of the BEC, which is expected since this state corresponds to

the saddle point on the Bloch sphere making the dynamics unstable. Thus, we can conclude that the BBR method will give good predictions even for weak dissipation as far as we start from a state in one of the above three cases. It is now easy to generalize the above results for an extended lattice. We expect that the method will break down if the initial state is dynamically unstable, that is when we are at the edge of the Brillouin zone [76].

2.5 Conclusions

In this chapter we have discussed a state of the art experimental setup. We have briefly presented the experiment of the Herwing Ott's group in which an electron beam can be focused with single site resolution and extract single atoms from an optical lattice. For one-dimensional lattice, we have modeled the system with a Master equation in which the unitary part uses the well-known Bose-Hubbard Hamiltonian. The mean-field approximation revealed a very interesting property of the system. The losses can create attractive fixed points in the classical phase space. This indicates that we can use dissipation in order to control the many-body dynamics. This is the subject of the next chapter.

In order to study many-body effects we have introduced the BBR approximation. The BBR method goes beyond the mean-field approximation and can describe many-body effects like quantum correlations and the depletion of the BEC mode. However, the method gives accurate predictions only when we are close to a pure BEC state. This constrain is easily fulfilled in the case of strong single particle losses. The method also works, even for strong interparticle interactions, when we are around a symmetric state for the double well or around the center of the Brillouin zone for extended lattices.

Chapter 3

Applications: Engineering Stable Nonlinear Structures

In the previous chapter we have briefly discussed how single particle losses can create attractive fixed points in the classical phase space (see subsection 2.3.1) and also how we can locally control the coherence of our system (see section 2.2). In this chapter we use these properties to create stable nonlinear structures, like discrete breathers and dark solitons [64,65]. As a tool to study the dynamics we will use the BBR method we have introduced in the previous chapter.

The present chapter is organized as follows. First, in section 3.1, we investigate a very important property of localized single particle losses, the inhibition of quantum tunneling. This effect can be used to coherently compress a BEC in an optical lattice. In section 3.2 we analyze the dynamics in a triple well trap with boundary losses. Strong interparticle interactions combined with dissipation create a stable discrete breather in the middle well. Localized losses together with phase engineering can be used to create a standing coherent dark soliton, which is discussed in section 3.3.

3.1 Inhibition of Quantum Tunneling

In section 2.2 we briefly saw that localized single particle losses does not only destroy particles, but also kills the coherences between the leaky well and the rest of the system. The cause of this observation is simple: the inhibition of quantum tunneling due to the dissipation. To focus on this effect we neglect the interparticle interactions, $U = 0$, which also means that our simulations are exact. It is also sufficient to study a small system: a three well trap with hard walls boundary conditions and with losses in the
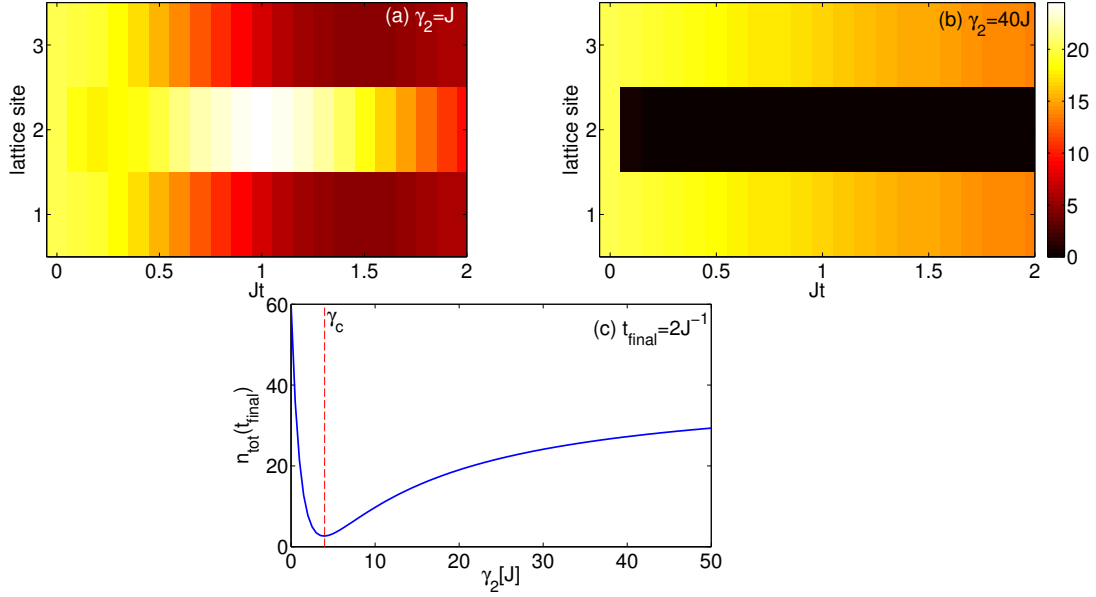
Figure 3.1: *Inhibition of quantum tunneling due to single particle losses, in a triple-well trap. (a), (b) Evolution of the atomic density $\langle \hat{n}_j \rangle$ for two different values of the loss rate. (c) Final value of the total particle number after fixed propagation time t_{final} as a function of the loss rate in the middle well, γ_2. The remaining parameters are $U = 0$ and $n_{\mathrm{tot}}(0) = 60$.*

middle well only. As an initial condition we use a pure homogeneous BEC.

In figures 3.1 (a,b) we have plotted the evolution of the atomic density, $\langle \hat{n}_j \rangle$, for weak, $\gamma_2 = 1J$, and strong, $\gamma_2 = 40J$, dissipation, respectively. For weak dissipation the atoms tunnels to the middle well where they are dissipated with rate, γ_2. From the other hand, strong losses lead to the formation of a stable vacancy. But here we can observe something interesting if we compare the two figures. In figure 3.1 (a) the particles tunnel back and forth to the leaky site, the well-known oscillations of the noninteracting BEC. In contrary, in figure 3.1 (b) we can see clearly that the particles have a difficulty to tunnel, they tend to remain in their original well. So the tunneling rate slows down and the particles that tunnel to the leaky site leave the system. Since we don't have interactions the only cause of this effect could be dissipation.

The situation becomes clearer in figure 3.1 (c), where we have plotted the total particle number after fixed propagation time, $t_{\mathrm{final}} = 2J^{-1}$, as a function of the loss rate, γ_2. As one can see, the residual atom number assumes a minimum for a finite loss rate γ_c. After this critical value, one faces the paradoxical situation that an increase of the loss rate can suppress

the decay of the BEC. We can estimate the critical loss rate, γ_c, by matching the time scale of dissipation $\tau_D = 2/\gamma_2$ and tunneling $\tau_J = 1/(2J)$, where in the later the factor $1/2$ accounts for atoms tunneling from two sites to the leaky site. Hence, the critical loss rate is estimated as $\gamma_c = 4J$. We find a good agreement of our qualitative estimate for γ_c (dashed red line in figure 3.1 (c)) with the dip in the total particle number.

The inhibition of the quantum tunneling to a leaky lattice site can be understood by simple analogy to wave optics: a large mismatch of the index of refraction leads to an almost complete reflection of a wave from a surface. This is true for real index of refraction just as well as for an imaginary index describing an absorbing material such as metal. Similarly, a large difference of the on-site potential, real or imaginary, prevents tunneling of the atoms to the respective lattice site. Another interpretation has been discussed in [65, 71, 72] in term of quantum Zeno effect. The particle losses can be viewed as a continuous measurement of the quantum state of the leaky lattice site. This measurement causes a Zeno effect which prevents the tunneling to the observed site. This interpretation is natural in the Herwig Ott's group experiments where the lost atoms (in the form ions) are actually measured from the ion detector.

3.1.1 Coherent Compression of a BEC

Strong particle losses do not only block the tunneling of the atoms to the leaky site but also repel them since this site behaves as a hard wall. We can use this observation to compress a BEC by slowly scan the losses through the lattice. The process is depicted in figure 3.2, where we have a lattice with 21 sites, which is loaded with a pure homogeneous BEC with initial average density of 100 atoms per site. The particle losses (for example an electron beam) induced in the 21st lattice site and is then slowly scanned through the lattice, such that loss occur at different sites as illustrated in figure 3.2 (b). In figure 3.2 (c) we have plotted the evolution of the total particle number. The total population drops fast to about 2000 atoms since the strong losses have destroyed all the population in the 21st site. However, after this the decay slows down and every time that the losses change site the decay is significantly smaller than the initial. At the end we have lost about 550 atoms, while one would naively expect to lose about 800 atoms. Thus we end up with an average density of 120 atoms per lattice site. This happens because the atoms are repelled from the leaky site, so the atomic density in the lower part of the lattice increases as shown in 3.2 (a). We can further improve the compression if we increase the losses. Finally, we must
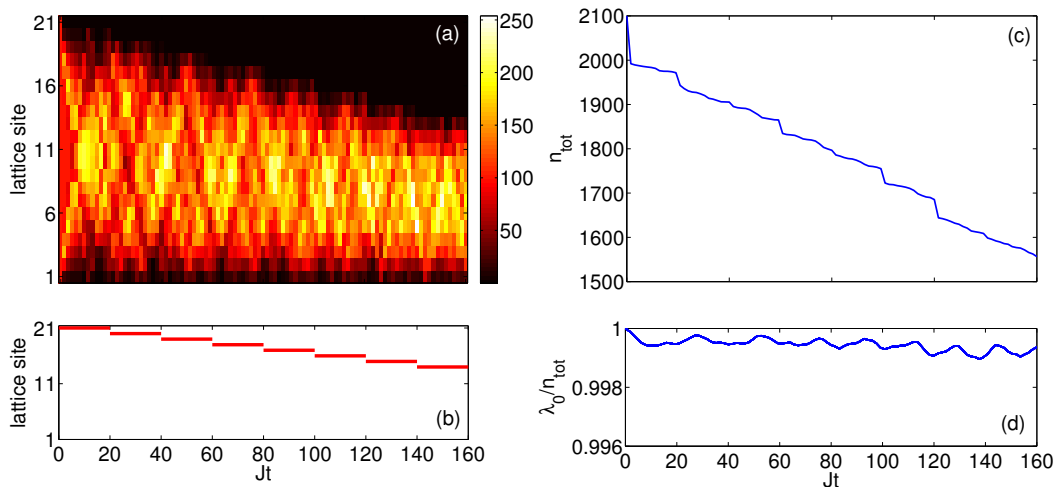
Figure 3.2: *Compressing a BEC by moving loss in a lattice with 21 sites.* (a) *Evolution of the atom density when strong moving losses are applied in one lattice site $\gamma = 400J$. The BEC is compressed in the lower part of the lattice although several atoms are lost.* (b) *The red lines indicate the position of the leaky site. Evolution of the total particle number n_{tot}* (c) *and of the condensate fraction λ_0/n_{tot}* (d). *The macroscopic interaction strength is $U n_{tot}(0) = 2.5J$, with $n_{tot}(0) = 2100$.*

note that the BEC remains practically completely pure in the whole process, as it is depicted in figure 3.2 (d).

3.2 Discrete Breathers

In this section we discuss how boundary particle losses can form and stabilize coherent discrete breathers. To this end we consider the dynamics of an initially pure and homogeneous BEC in a triple-well trap with particle losses only in the two boundary wells. For this small system exact simulations are still possible by using the quantum jump method, thus we will have the opportunity to test the BBR method once more. In figures 3.3 (a)-(d) we have the evolution of the atomic density, $\langle \hat{n}_j \rangle$, and of the condensate fraction, λ_0/n_{tot}, for weak ($U = 0.5J$) and strong interactions ($U = 6J$). In both cases, the population at the boundary wells rapidly decreases, but the similarities stop here. For weak interactions, figures 3.3 (a,b), the particles at the central well tunnels to the boundaries where they leaves the lattice. In the whole process the BEC remains almost pure, figure 3.3 (b) and the BBR method agrees well with the exact simulations. The behavior changes
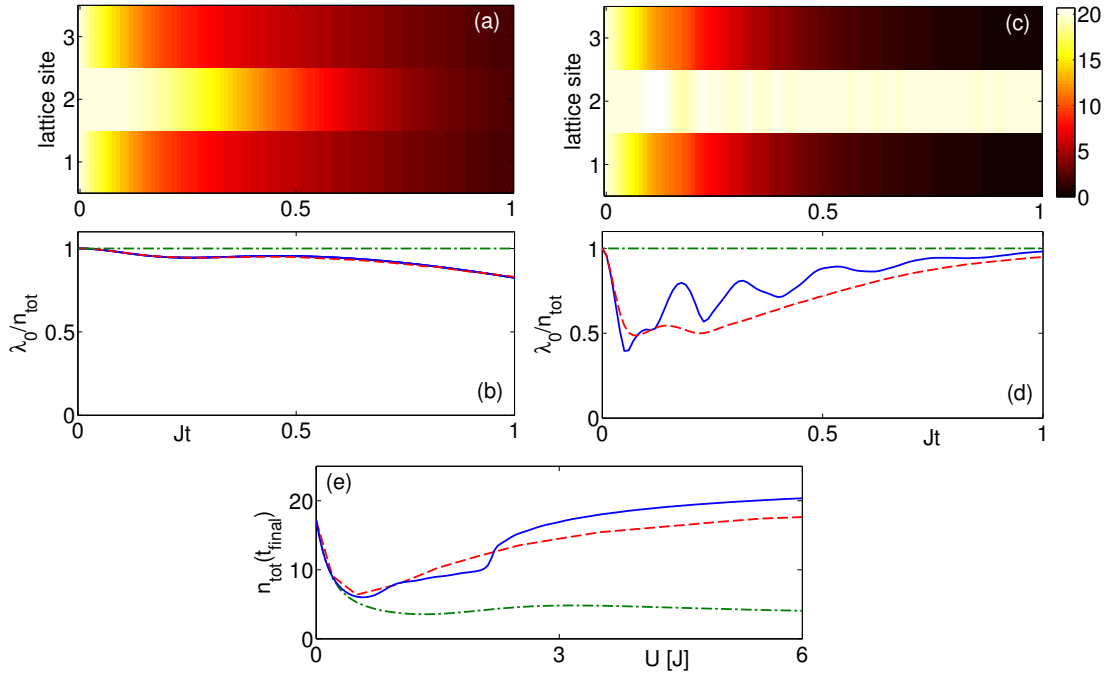
Figure 3.3: *Dynamics of a BEC in a triple-well trap with boundary dissipation. Evolution of the atomic density $\langle \hat{n}_j \rangle$ (a,c) and of the condensate fraction λ_0/n_{tot} (b,d) for $U = 0.5J$ and $U = 6J$, respectively. (e) Total particle number after a fixed propagation time $t_{\text{final}} = 1J^{-1}$ as a function of the interaction strength. The parameters are $\gamma_1 = \gamma_3 = 4J$, $\kappa = 0$ and $n_{\text{tot}}(0) = 60$. Mean-field (green dashed dotted line) and BBR (blue solid line) results are compared to numerically exact simulations with the quantum jump method, averaging over 200 trajectories (red dashed line).*

dramatically for strong interactions, figures 3.3 (c,d). The population in the central well remains remarkably stable, while for sort times we have a fast depletion of the BEC, figure 3.3 (d). More surprisingly for longer times we observe a repurification of the BEC.

In other words we have a stable population, which is about the one third of the initial total population, of pure BEC localized in the central site. This counterintuitive localization phenomenon in the presence of repulsive interactions is a consequence of the dynamical formation of a discrete breather centered in the middle site of the triple well trap. Generally, discrete breathers, also called, discrete solitons, are spatially localized stable (or at least long-lived) excitations in a periodic discrete system [46–48]. These nonlinear structures arise intrinsically from the combination of nonlinearity and discreteness of the system. In the presence of boundary particle losses this

excited state becomes an attractive fixed point in the classical phase space, so a wide class of initial states will converge to a pure BEC with a breather-like density. Once the discrete breather is formed, it remains stable also if the losses are switched off. The importance of strong interactions is depicted in figure 3.3 (e), where the residual total population after $t_{\text{final}} = 1J^{-1}$ of propagation is plotted as a function of the interaction strength. The total particle number increases for large values of U to $n_{\text{tot}}(Jt_{\text{final}}) \approx 20$ due to the breather formation.

Before we analyse further the discrete breather formation let us discuss the strength of the BBR predictions. First we observe that the mean-field approximation fails for strong interactions. This is apparent from figure 3.3 (e) where it strongly underestimates the residual particle number. It predicts the discrete breather formation only for stronger particle losses. From the other hand, the BBR method has a good agreement with the exact numerical simulations. This observation suggests that the quantum fluctuations facilitate the formation of repulsively bound structures. Furthermore, the mean-field approximation cannot predict genuine many-body features of the dynamics like the depletion and repurification of the BEC we discussed above. The BBR method faithfully reproduces the depletion and the repurification, but additionally predicts unphysical temporal revivals. However, this is expected since for intermediate times the system is far from a pure BEC state. This example thus demonstrates the strength but also the limitations of this approach.

In figure 3.4 we further analyse the formation and the decay of the discrete breather. The total particle number n_{tot} decreases rapidly until the breather formation at $t \approx 1J^{-1}$. After that time the decay is extremely slow, showing how stable the discrete breather is. We can analytically estimate the behavior of n_{tot} using the equation

$$\frac{d}{dt}n_{\text{tot}} \approx -\gamma_1 n_1 - \gamma_3 n_3 = \frac{2\gamma}{3}n_{\text{tot}}, \tag{3.1}$$

where $\gamma = \gamma_1 = \gamma_3$ and we have used the fact that the wells are initially homogeneously filled, $n_1 = n_3 = n_{\text{tot}}/3$. So for sort times the total particle decays as

$$n_{\text{tot}}(t) \approx n_{\text{tot}}(0) \exp\left\{-\frac{2\gamma}{3}t\right\}. \tag{3.2}$$

After the discrete breather is formed, the population of the outer wells is $n_1 = n_3 = J^2/(U^2 n_{\text{tot}})$, where we have used first order perurbation theory in J/U, since we are in the strongly interacting regime. Thus we can write

$$\frac{d}{dt}n_{\text{tot}} \approx -\gamma_1 n_1 - \gamma_3 n_3 = \frac{2\gamma J^2}{U^2}\frac{1}{n_{\text{tot}}}. \tag{3.3}$$
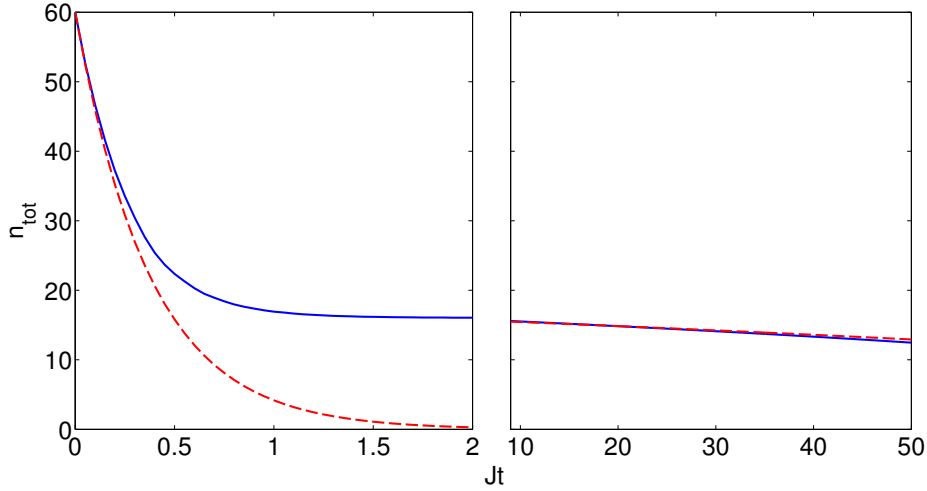
Figure 3.4: *Comparison between the BBR results (blue solid line) and the analytic estimates (3.2) and (3.4) (red dashed line). The parameters are $U = 3J$, $\gamma_1 = \gamma_3 = 4J$, $\kappa = 0$ and $n_{\text{tot}}(0) = 60$.*

Assuming that we have n_{db} atoms bound in the discrete breather state, the total population decays as

$$n_{\text{tot}}(t) \approx \sqrt{n_{\text{db}}^2 - \frac{4\gamma J^2}{U^2} t}. \tag{3.4}$$

The BBR approximation agrees with the above analytical estimates, as we observe in figure 3.4 for $n_{\text{db}} = 16$. For very sort times ($t \lesssim 0.2 J^{-1}$) we have an exponential decay, while we have an algebraic decay when the discrete breather is formed. The transition between the linear and nonlinear decay takes place at $t \approx 0.5 J^{-1}$. A deviation from the algebraic decay (3.4) for the discrete breather is observed only for very long times when the population is very small, so the simple perturbative estimate for n_1 and n_3 is no longer valid.

3.2.1 Spectrum Analysis

The quantum jump method is not just a powerful method to unravel a Master equation, but also gives an interesting interpretation of the dissipative dynamics. The continuous evolution of the system, which is described by a effective non-Hermitian Hamiltonian, is interrupted by stochastic quantum jumps (for more details see Appendix A). For the system at hand the effective
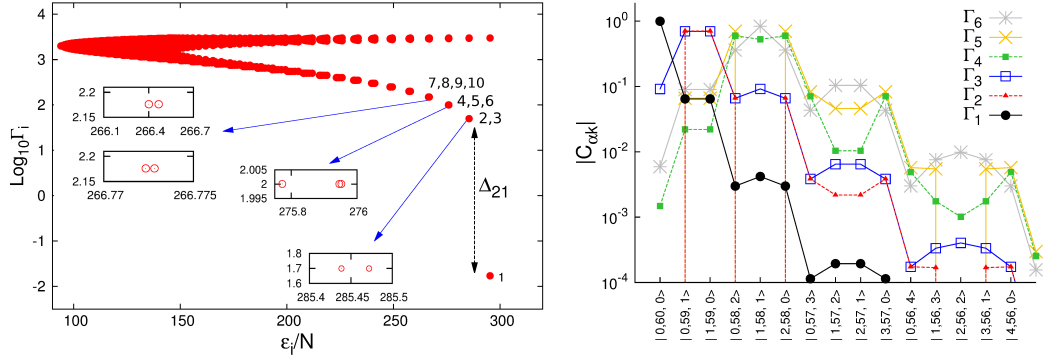
Figure 3.5: (Left) *The generalized spectrum of the effective Hamiltonian (3.5).* (Right) *The expansion coefficients $|C_{\alpha k}|$ for the first six stable states. Note that we have not plotted all the states but only the interesting ones. The parameters are $U = 2J$, $\gamma = 20J$ and $N = 60$.*

Hamiltonian is given by

$$\hat{H}_{\text{eff.}} = \hat{H} - i\frac{\gamma}{2}\hat{\alpha}_1^\dagger\hat{\alpha}_1 - i\frac{\gamma}{2}\hat{\alpha}_3^\dagger\hat{\alpha}_3, \tag{3.5}$$

where $\hat{H}$ is the Bose-Hubbard Hamiltonian for the trimer. The spectrum of this effective Hamiltonian can be used to extract useful informations about the stability of quantum states [68], like the discrete breather. Since, the Hamiltonian (3.5) is non-Hermitian, its eigenvalues are complex

$$\hat{H}_{\text{eff.}}|E_k\rangle = \left(\varepsilon_k - i\frac{\Gamma_k}{2}\right)|E_k\rangle \equiv E_k|E_k\rangle, \tag{3.6}$$

where the imaginary part of the generalized spectrum, Γ_k, gives the decay rate of the corresponding eigenstate.

In order to diagonalize[1] the Hamiltonian (3.5) we use the Fock basis, $|n_1, n_2, n_3\rangle$. The dimension of the Hilbert space is given by

$$D(\mathcal{H}) = \frac{(N + M - 1)!}{N!(M - 1)!}, \tag{3.7}$$

where N is the total particle number and M the number of lattice sites, here $M = 3$. The eigenstates of the Hamiltonian (3.5) can be expanded using the Fock basis

$$|E_k\rangle = \sum_\alpha C_{\alpha k}|n_1, n_2, n_3\rangle_\alpha, \tag{3.8}$$

---

[1]The numerical calculation was done with the help of Dr. Carlos Parra-Murillo, whom I deeply thank.
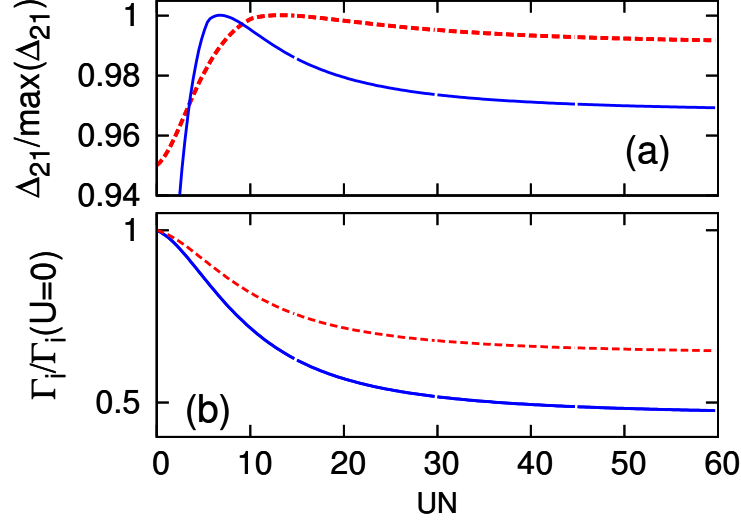
Figure 3.6: (a) *The normalized spectral gap* Δ_{21} *for* $\gamma = 10J$ *(solid blue line) and* $\gamma = 20J$ *(dashed red line) and* (b) *the normalized decay rates of the first three most stable states for* $\gamma = 20J$ *(blue solid line* Γ_1 *and red dashed line* $\Gamma_{2,3}$*), as a function of the macroscopic interaction strength* UN. *In both figures the particle number is fixed,* $N = 60$, *while the interaction strength* U *varies.*

where the coefficients $|C_{\alpha k}|$ will help us to recognize the structure of the eigenstates.

In the left panel of figure 3.5 we depict the spectrum of the effective Hamiltonian (3.5), Γ_k versus ε_k, for strong interparticle interactions. We can easily distinguish one state in the bottom-right corner of the graph. It is a very stable with high energy state. Furthermore, the coefficients $|C_{\alpha k}|$ reveals that the main contribution to the Fock expansion comes from the $|0, N, 0\rangle$ state, as it is illustrated in the right panel of figure 3.5. This state correspond to a stable breather localized in the second well. The next stable states are separated by a gap from the breather state and are degenerated, because of the spatial symmetry of the system. The projections in the Fock states is nearly given by the linear combination of the states

$$\begin{aligned}
|E_{k=2,3}\rangle &\rightarrow \{|1, N-1, 0\rangle, |0, N-1, 1\rangle\} \\
|E_{k=4,5,6}\rangle &\rightarrow \{|2, N-2, 0\rangle, |1, N-2, 1\rangle, |0, N-2, 2\rangle\} \\
|E_{k=7,8,9,10}\rangle &\rightarrow \{|3, N-3, 0\rangle, |1, N-3, 2\rangle, |2, N-3, 1\rangle, |0, N-3, 3\rangle\}.
\end{aligned} \tag{3.9}$$

The corresponding coefficients, $C_{\alpha k}$, are almost equal in magnitude in many of the cases and with normalization $\sum_\alpha |C_{\alpha k}|^2 \approx 1$. This is illustrated in
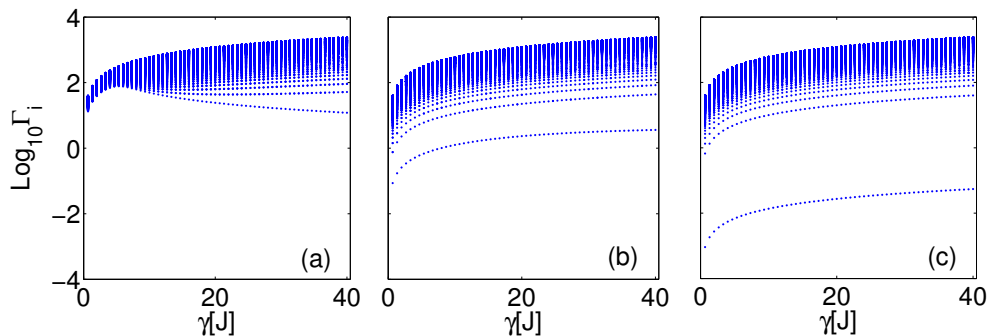
Figure 3.7: *The logarithm of the decay rate as a function of γ for three different interaction strengths:* (a) $U = 0$, (b) $U = 0.5J$ *and* (c) $U = 5J$. *The initial particle number is $N = 60$.*

the right panel of figure 3.5, where only the projections onto the Fock states with decreasing n_2 are shown, although we have used the complete Fock states. In the left panel of figure 3.5 we can also identify the two degenerate states in the upper-right corner has the same energy as the breather state but are highly unstable. This indicates that these states corresponds to a breather localized in the first or third well where the losses occur. The rest of the states, with large decay rates, are very leaky eigenstates since a large number of Fock states participate on the evolution, so it is easier to remove all the particles from the system.

The stability of the breather state is characterized by its decay rate Γ_1. So we can use the spectral gap $\Delta_{21} = \Gamma_2 - \Gamma_1$ as a criterion for the stability of the state with the smallest decay rate. The larger the gap is the more stable the state is. In figure 3.6 (a) we have plotted the gap as a function of the interaction strength UN, where the total particle number N is fixed. The gap increases, assumes a maximum and then saturates. The existence of the maximum is a consequence of the different decrease rates between the state with decay rate Γ_1 and the states with $\Gamma_{2,3}$, as it is depicted in figure 3.6 (b). In the same figure we observe that the Γ_1 tends to zero for strong interactions. Another interesting observation is that the spectral gap tends to be one for strong dissipation rate, independently of the interaction strength. The cause of this is the inhibition of the quantum tunneling we discussed in section 3.1.

Figures 3.7 also confirm the above discussion. Shown is the behavior of the decay rates Γ_i as a function of the dissipation rate γ, for three different interaction strengths. In all cases we observe that with increasing γ one state separates from the rest. These states have the lowest decay rate. The
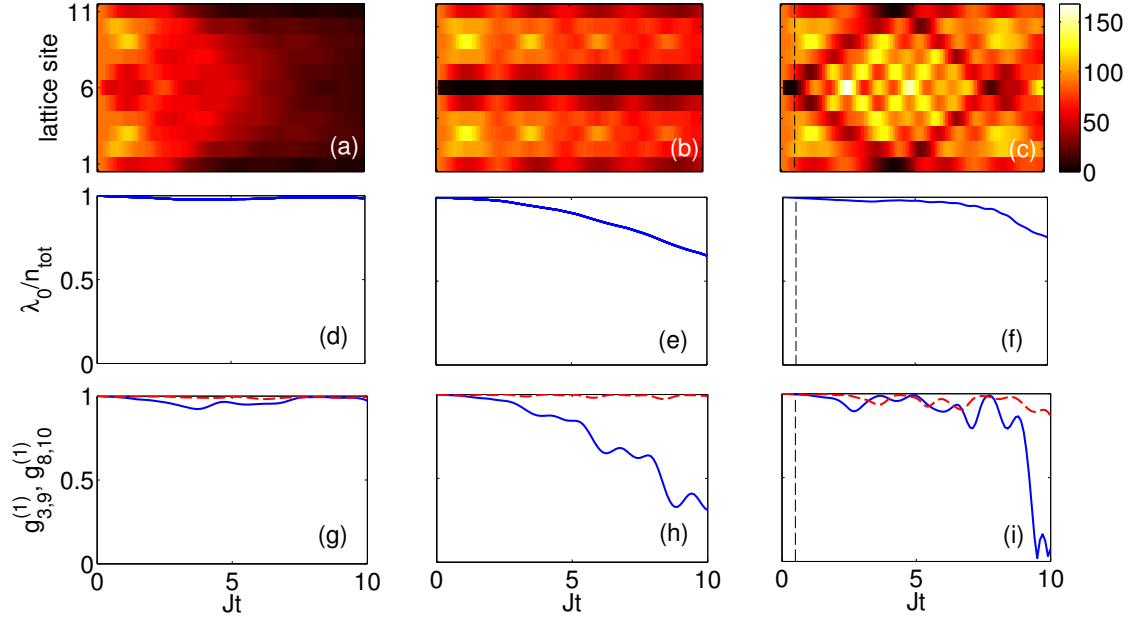
Figure 3.8: *Coherence of a vacancy generated by loss from the central site, for weak, $\gamma_6 = 2J$, (first column) and strong, $\gamma_6 = 20J$, (second and third columns) dissipation. In the third column the losses occur for times $t < 0.5J^{-1}$ only, indicated by the dashed black lines. Evolution of the particle density (a)-(c) of the condensate fraction (d)-(f) and of the first order coherence functions between sites 3,9 (blue solid line) and 8,10 (red dashed line) (g)-(i). The parameters are $U = 0.02J$, $\kappa = 0$ and $n_{\text{tot}}(0) = 1000$.*

effect is enhanced when we increase the interaction strength. For strong interactions, figure 3.7 (c), this low decay rate state is the breather state with the particles localized in the middle site. For zero interactions, figure 3.7 (a), the corresponding state is a consequence of the inhibition of the tunneling due to the strong dissipation. We further clearly observe that the most stable state presents a maximum at $\gamma = 4J$, which is exactly the Zeno effect we discussed in section 3.1.

3.3 Dark Solitons

From the discussion we had in section 3.1, about the inhibition of quantum tunneling, one could imagine that we can use localized losses to engineer a dark soliton. Of course, what we had in figure 3.1 (b) was not a dark soliton, although our system is fully coherent, since there is no nonlinearity. In this

section we discuss what happens in the presence of interparticle interactions. As a system we use a lattice with 11 sites, where dissipation occurs only in the middle site. Initially, the lattice is loaded with pure homogeneous BEC with 1000 particles.

The nonlinear case is similar with what discussed in section 3.1. For weak losses the particle tunnels to the leaky central site where they leave the lattice, figure 3.8 (a). The BEC remains pure in the whole evolution as we can see in figure 3.8 (d,g). To further analyze the coherence in our system we will use the first order coherence function

$$g_{j,\ell}^{(1)} = \frac{|\langle \hat{\alpha}_j^\dagger \hat{\alpha}_\ell \rangle|}{\sqrt{\langle \hat{n}_j \rangle \langle \hat{n}_\ell \rangle}} \tag{3.10}$$

between the sites j and ℓ. As expected the coherence between different sites is preserved, figure 3.8 (d). For strong dissipation, figure 3.8 (b), again a stable vacancy appear in the central leaky site and the loss of atoms slows down. However, there is an important difference with the noninteracting case, the condensate loses its purity as it is depicted in figure figure 3.8 (e). This is further confirmed in figure figure 3.8 (h) where we have the evolution of the first order coherence function. As we can see the coherence between sites 3 and 9 drops fast, while the coherence between sites 8 and 10 is preserved. This means that the condensate fragments into two pieces without relative phase coherence. Thus, we cannot claim that we have created a coherent dark soliton. Here we must note that the mean-field approximation predicts that dissipation can be used to create coherent dark solitons [54], since it cannot assert the coherence of the final state.

In figure 3.8 (c), we follow a different strategy. We switch off the dissipation after a vacancy is formed, at $t < 0.5J^{-1}$. In this case the condensate remains pure for longer times (figure 3.8 (f)), but the vacancy is not stable. It splits into two dark solitons which travel outwards where are reflected at the boundaries. When the two dark solitons are met again we observe a rapid loss of coherence between the two halfs of the lattice (figure 3.8 (i)), so the dark solitons are destroyed. As we are going to see in the next subsection, in order to engineer a stable and standing dark soliton we will need one more ingredient: phase imprinting.

3.3.1 Phase Imprinting

Phase imprinting is a well-known, both theoretical [75, 76] and experimental [73, 74], method to create dark solitons. The BEC is exposed to a pulsed, off-resonant laser light, such that the atoms experience a spatially varying
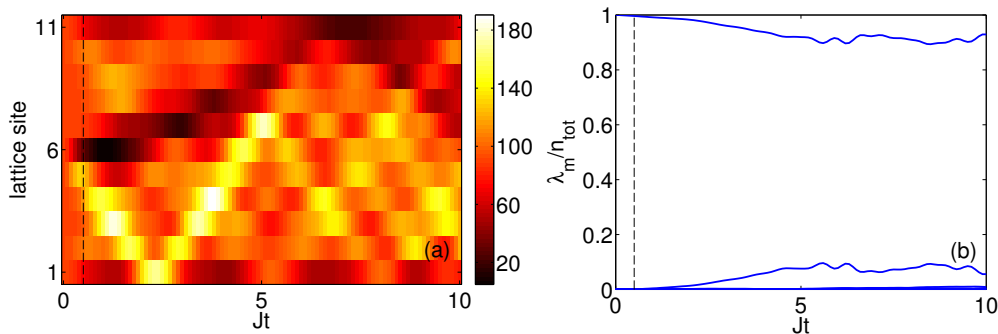
Figure 3.9: *Generation of a moving dark soliton using phase imprinting in the upper half of the lattice, both for times $t < 0.5J^{-1}$. Evolution of the particle density* (a), *of the SPDM eigenvalues* (b). *The parameters are $U = 0.02J$, $\kappa = 0$ and $n_{\text{tot}}(0) = 1000$.*

light-shift potential of the form $V(\ell) = V_0\Theta(\ell - k)$ for a time T. Here Θ is the Heaviside function and k is the lattice site where a phase jump will occur. We choose the exposition time T such that $V_0T = \pi$. If T is small enough, so we can neglect the tunneling during this time, the phase of the condensate wavefunction changes as e^{-iV_0T} for $\ell > k$. In this way we have imprinted a sudden change of the condensate phase at $\ell = k$. However, a phase jump is possible only if the density at $\ell = k$ vanishes. In this way coherent dark soliton is created at the desired lattice site k.

In figure 3.9 we have applied this method to an 11-site lattice which initially is filled with a pure homogeneous BEC. The local potential is applied on the upper half $(V(\ell) = V_0\Theta(\ell-6))$ of the lattice for $t < 0.5J^{-1}$, imprinting a phase difference of π. The result of the phase imprinting is that a large density of particles travels to the lower half of the lattice with large velocity, while a dark soliton travels to the opposite direction with smaller velocity (figure 3.9 (a)). In the whole evolution the coherence of the condensate is preserved as we can see in figure 3.9 (b), where we have plotted the evolution the eigenvalues of the SPDM, λ_m/n_{tot}. In this case we have achieved to create a coherent dark soliton which however is moving in the lattice. In the next subsection we present how we can combine phase imprinting with particle losses in order to engineer a stable, standing, coherent dark soliton.

3.3.2 Coherent Dark Soliton

It has been proposed that one can create a standing dark soliton by properly engineer the phase and the density of the BEC in the framework of Gross-Pitaevskii equation [75]. Here we use the localized particle losses in
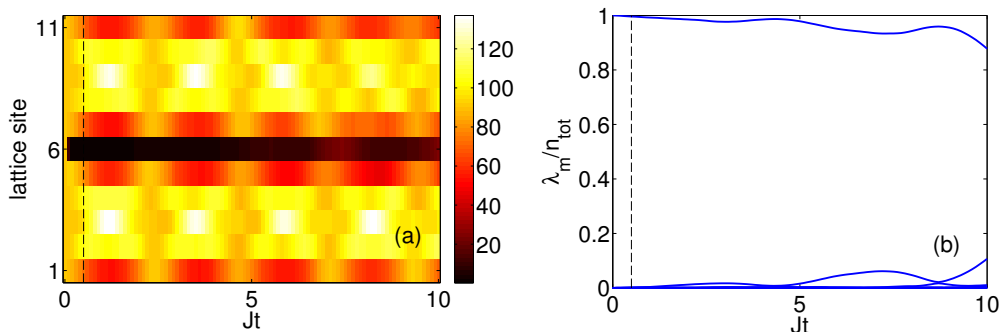
Figure 3.10: *Generation of a dark soliton using particle losses at rate $\gamma_6 = 20J$ at the central site and phase imprinting in the upper half of the lattice, both for times $t < 0.5J^{-1}$. Evolution of the particle density* (a), *of the SPDM eigenvalues* (b). *The parameters are $U = 0.02J$, $\kappa = 0$ and $n_{\mathrm{tot}}(0) = 1000$.*

order to achieve the required density profile. We use again a lattice with eleven sites filled with pure homogeneous BEC and we apply a local potential on the upper half of the lattice for $t < 0.5J^{-1}$, as we did in the previous subsection, and in addition we use particle losses in the central site for the same period of time, see figure 3.10. The result is a standing dark soliton in the central site. The condensate remains pure over a long time, as it is depicted in figure 3.10 (b).

In real life experiments the local potential, used for the phase imprinting, is never sharp enough to describe it with a step function, but there is a finite width at the edge [73]. In order to make our simulations more realistic we use a potential of the form

$$V(\ell) = \frac{V_0}{1 + \mathrm{e}^{-C(\ell - k)}}, \tag{3.11}$$

where k is the central site of the lattice. For $C \to \infty$ this function is the Heaviside step function. As in the previous subsection, we use this potential for $t < 0.5J^{-1}$, in combination with particle losses in the central site $k = 6$ for the same period of time. In figure 3.11 we have the resulting dynamics for two different functions 3.11. For $C = 6$, figure 3.11 (a), we observe the formation of a dark soliton which survive for a long time. However, for $t \approx 10J^{-1}$ the particles start to fill the vacancy and the soliton is destroyed, figure 3.11 (b). The BEC remains approximately pure, as it is depicted in figure 3.11 (c). From the other hand, for a smoother potential, figure 3.11 (d) where $C = 2$, we observe that the dark soliton is destroyed much sooner than in the previous case. The particles start to drop into the central site at about $t \approx 6J^{-1}$, figure 3.11 (e). Moreover, the condensate fragments since
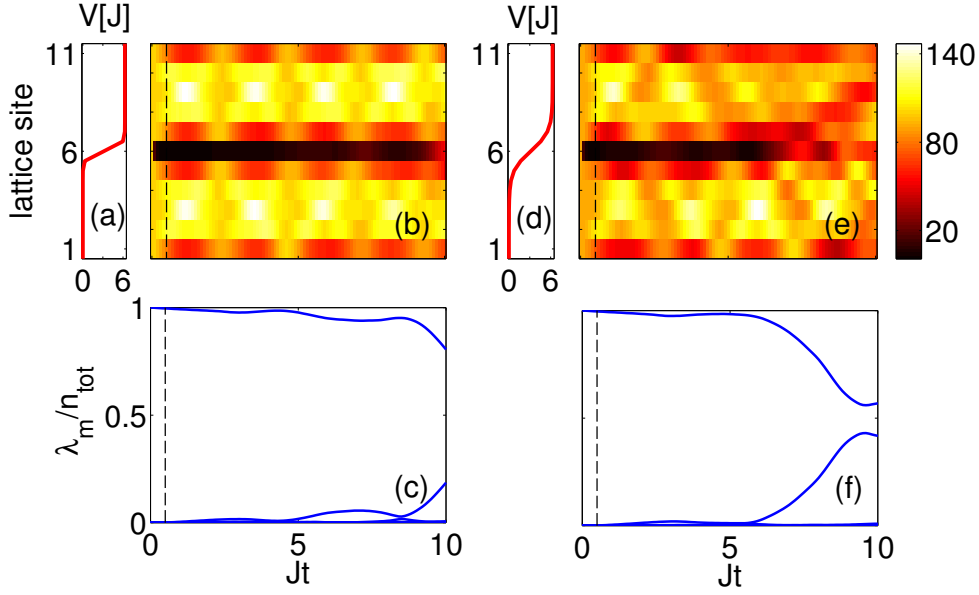
Figure 3.11: *Generation of a dark soliton using particle losses at rate $\gamma_6 = 20J$ at the central site and phase imprinting in the upper half of the lattice using a smooth function with $C = 6$ (a) and $C = 2$ (d), both for times $t < 0.5J^{-1}$. Evolution of the particle density (b,e), of the SPDM eigenvalues (c,f). The parameters are $U = 0.02J$, $\kappa = 0$ and $n_{tot}(0) = 1000$.*

a second macroscopic eigenvalue of the SPDM emerges, see figure 3.11 (f). In other words, the smoother the potential is, the sooner the dark soliton is destroyed.

3.4 Conclusions

In this chapter we have discussed how we can use localized single particle losses in order to engineer stable nonlinear structures in an one dimensional optical lattice initially filled with BEC. We have created a discrete breather, in a triple-well trap, by using boundary dissipation. This was possible due to the cooperation between the strong interparticle interactions and the losses. Although, one expects strong interaction to destroy the BEC, the dissipation helps to repurify the condensate almost completely. Another striking effect is that strong dissipation can effectively suppress decay and induce stable vacancies. The number of the lost atoms shows a pronounced maximum for intermediate values of loss rate, when the time scales of the dissipation and the tunneling are matched. A standing coherent dark soliton can be created

if we use in addition with the losses phase engineering. These examples show that dissipation can be used to control the dynamics in complex quantum many-body systems.

Chapter 4

Entanglement in Dissipative Optical Lattices

In the present chapter we analyze the dynamics induced by the interplay of localized particle dissipation and strong atom-atom interactions. If the interaction strength exceeds a threshold, two meta-stable equilibria emerge which can be used to prepare either an almost pure Bose-Einstein condensate or a macroscopically entangled "breather" state.

The meta-stable breather states show remarkable statistical properties: The atoms relax to a coherent superposition of bunches localized at different lattice positions. Driven by particle loss and interactions, almost all atoms localize in one of the non-dissipative wells. The meta-stable state corresponds to a *coherent* superposition of these localized modes and thus to a macroscopically entangled quantum state. Because of the tunable large number of atoms forming the breather state, they may serve as a distinguished probe of decoherence and the emergence of classicality. Furthermore, the breather states generalize the so-called NOON states enabling interferometry beyond the standard quantum limit [43, 44]. As particle loss is an elementary and omnipresent dissipation process, this method may be generalized to a variety of open quantum systems well beyond the dynamics of ultracold atoms, e.g. to optical fiber setups [102] or hybrid quantum systems [103, 104].

This chapter is organized as follows. First we analyze breather states in small systems, which allow for a numerically exact simulation of the quantum many-body dynamics in section 4.1. In extended lattices discussed in section 4.3, the localized modes correspond to so-called discrete breathers. The emerging meta-stable quantum state is more complex, as the atoms can localize in a variety of lattice sites. Nevertheless, one can identify "breather-states" by the number fluctuations and the correlations between neighboring

sites. The formation of breather states can be understood to a large extent within a semi-classical phase space picture introduced in section 4.2. We analyze the flow of phase space distribution functions such as the Wigner or the Husimi function. To leading order it is given by a classical Liouvillian flow which is equivalent to a dissipative Gross-Pitaevskii equation. The emergence of breather states can then be linked to a classical bifurcation of the associated mean-field dynamics. While this semiclassical approach obviously cannot describe the coherence of the quantum state or the formation of entanglement, it correctly predicts the critical interaction strength above which breather states are formed.

4.1 Decay in a Three Site Lattice

Our starting point is the open Bose-Hubbard trimer, allowing for numerical exact solutions for rather large particle numbers. Already, this simple model exhibits the different dynamical phases we aim to understand. We consider periodic boundary conditions, while losses occur only from the site $j = 2$ at a rate γ_2. The system is mirror-symmetric with respect to an exchange of sites 1 and 3.

4.1.1 Particle Correlations

Particle dissipation obviously reduces the total particle number in the lattice, but, as we discussed in the previous chapters, this is not the most interesting effect. Rich dynamics can be revealed if we study the quantum correlations in the strong interacting regime. In figure 4.1 we have simulated the dynamics for three different initial states for weak ($U = 0.01J$) and strong ($U = 0.1J$) interactions. A pure Bose-Einstein condensate with an (anti-) symmetric wavefunction

$$|\Psi_\pm\rangle = \frac{1}{2^N \sqrt{N!}} (\hat{\alpha}_1^\dagger \pm \hat{\alpha}_3^\dagger)^N |0\rangle \tag{4.1}$$

and the Fock state

$$|\Psi_F\rangle = \frac{1}{2\sqrt{(N/2)!}} (\hat{\alpha}_1^\dagger)^{(N/2)} (\hat{\alpha}_3^\dagger)^{(N/2)} |0\rangle, \tag{4.2}$$

assuming that the initial particle number N is even. In the top row of figure 4.1 we have plotted the evolution of the total particle number n_{tot}. The most interesting observation here is that the decay is very slow for the

anti-symmetric initial state $|\Psi_-\rangle$. Indeed, this state is a stationary state of the Master equation (2.1) for $U = 0$, such that decay is absent in the non-interacting limit (cf. [62]). The physical reason for this is the destructive interference of atoms tunneling from sites 1 and 3 to the leaky site 2. In the case of strong interactions, tunneling is allowed but weak. Localized states, which will be referred to as breather states, form at the non-dissipative sites. The formation and properties of these states is analyzed in detail in the present chapter.

The dissipative dynamics drives the atoms to a very different quantum state depending on the initial state and the interaction strength U. To characterize these states we analyze the first and second order correlation functions between different sites of the lattice. The coherence of the many-body quantum state is characterized by the first-order correlation function (3.10) between the wells j and ℓ, which is plotted in the second row of figure 4.1. The symmetric initial state $|\Psi_+\rangle$ is stable for all values of the interaction strength U and the BEC remains approximately pure. In this case, particle dissipation can even increase the purity and coherence of the condensate. This counter-intuitive feature was discussed in detail in [58,59,64,65]. The anti-symmetric state $|\Psi_-\rangle$ is stable only if interactions are weak. For $U = 0.1J$ one observes a sharp decrease of first-order correlation which indicates the destruction of the condensate. The initial state is dynamically unstable such that the atoms relax to a different meta-stable equilibrium state, the breather state.

Density fluctuations and correlations are characterized by the second order correlation function

$$g^{(2)}_{j,\ell} = \frac{\langle \hat{n}_j \hat{n}_\ell \rangle}{\langle \hat{n}_j \rangle \langle \hat{n}_\ell \rangle}. \tag{4.3}$$

For $j = \ell$, this expression reduces to the normalized second moment of the number operator $\langle \hat{n}_j^2 \rangle / \langle \hat{n}_j \rangle^2$, which quantifies the number fluctuations in the jth well. The evolution of the number correlations and fluctuations are shown in figure 4.1 in the bottom panels. While these quantities are essentially constant for a BEC with a symmetric wave function $|\Psi_+\rangle$, strong anti-correlations develop for the initial state $|\Psi_-\rangle$ in the regime of strong interactions. The (anti-) correlations are also found for the Fock state $|\Psi_F\rangle$, whose experimental preparation can be significantly easier. These results show that the atoms bunch at one of the non-dissipative lattice sites, while the other sites are essentially empty. Nevertheless, as we are going to discuss in detail in subsection 4.1.3, the two contributions localized either at site 1 or 3 remain *coherent*. The atoms thus relax deterministically to a macroscopically entangled state, also called a Schrödinger cat state (cf. [42]). We will refer to these states as "breather" states as they correspond to the so-called discrete breathers in extended lattices in the semiclassical limit [46, 47, 56].
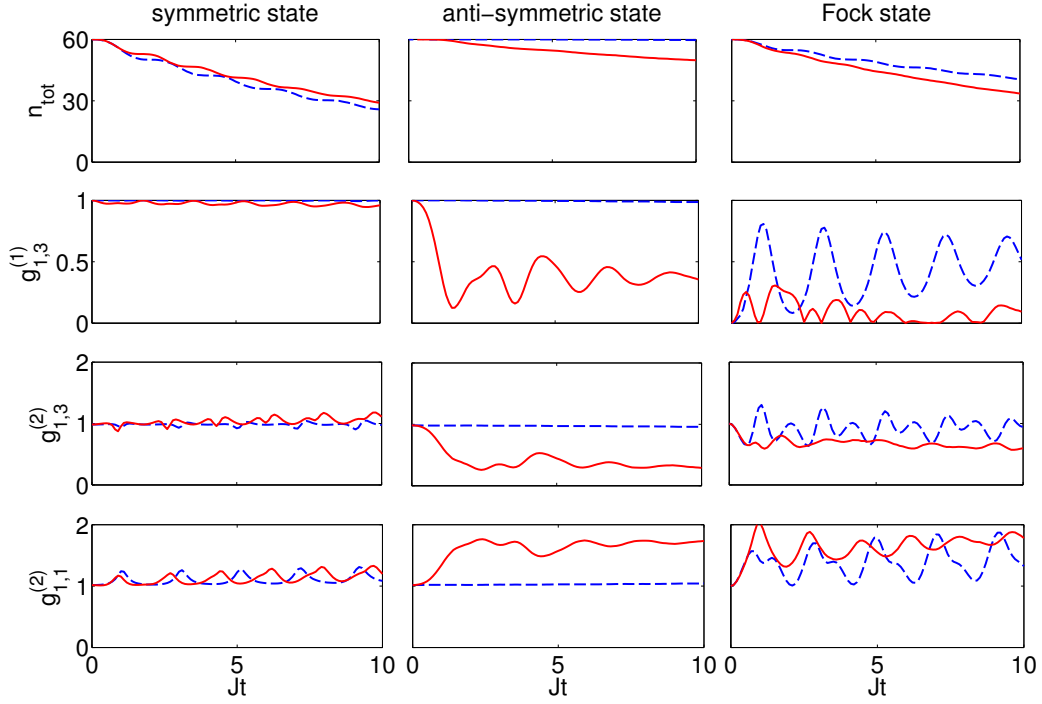
Figure 4.1: *Dynamics of the atom number and the correlation functions in an open Bose-Hubbard trimer with loss from site 2 for weak interactions ($U = 0.01J$, dashed blue line) and strong interactions ($U = 0.1J$, solid red line). Plotted is the total particle number n_{tot} (first row), the phase coherence between the sites 1 and 3 $g_{1,3}^{(1)}$ (second row), the number correlations between the sites 1 and 3 $g_{1,3}^{(2)}$ (third row) and the number fluctuations $g_{1,1}^{(2)}$ (fourth row). The dynamics has been simulated for three different initial states: A BEC with symmetric wave function (left), a BEC with an anti-symmetric wave function (middle) and a Fock state (right). The loss rate is $\gamma_2 = 0.2J$ and the initial populations are $n_1(0) = n_3(0) = 30$, $n_2(0) = 0$ in all cases. Time is given as Jt in units of the tunneling time. For the simulations we have used the quantum jump method averaging over 200 trajectories.*
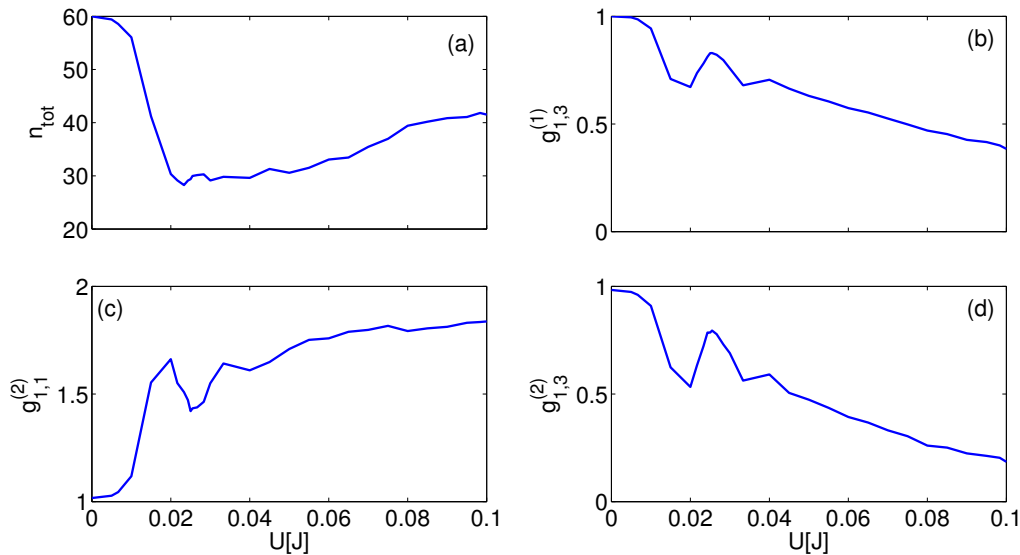
Figure 4.2: *Onset of breather formation in a triple-well trap for strong atomic interactions. Shown are* (a) *the total particle number* $\langle \hat{n}_{\text{tot}} \rangle$, (b) *the phase coherence* $g_{1,3}^{(1)}$ *and* (c,d) *the density correlation functions* $g_{1,1}^{(2)}$ *and* $g_{1,3}^{(2)}$ *as a function of the interaction strength* U *after a fixed propagation time* $t_{\text{final}} = 50 J^{-1}$ *for* $\gamma_2 = 0.2 \text{J}^{-1}$. *The initial state is a pure BEC in the state* $|\Psi_- \rangle$ *with* $N = 60$ *atoms. For the simulations we have used the quantum jump method averaging over 200 trajectories.*

This correspondence will be discussed in detail in section 4.2.

4.1.2 Transition to the Breather Regime

Strong interparticle interactions are crucial for the onset of the meta-stable breather states. This is analyzed in figure 4.2, where we have plotted the total particle number as well as the first and second order correlation functions after a fixed propagation time $t_{\text{final}} = 50\,J^{-1}$ versus the interaction strength U. As one can see for weak interactions, $U \lesssim 0.01\,J$, the BEC remains almost pure and the density-density correlation function are approximately equal to unity. The characteristic properties of a breather state, strong number fluctuations and anti-correlations between neighboring sites, are observed only for $U \lesssim 0.01\,J$. The transition to the breather regime can be understood within a semiclassical phase space picture which will be discussed in detail in section 4.2. This approach predicts a bifurcation of meta-stable states at a critical interaction strength $Un_{\text{tot}}(0) = 0.4J$. Before we come back to this issue, we first characterize the quantum properties of the breather states in

more detail.

4.1.3 Breather State: Characterization

Characteristic of a breather state is the large number of particles localized at a single lattice site, leaving the neighboring sites essentially empty. To make this statement more precise, we analyze the full counting statistics and the coherence of the many-body quantum state in detail. Figure 4.3 (a,b) shows the full counting statistics of the particle number in well 1 and 2, respectively, at time $t = 10\,J^{-1}$ after a breather state has formed. The most important result is that the probability distribution $P(n_1)$ becomes bimodal: Either a breather forms in the first well (n_1 large) or in the third well (n_1 almost zero). The second well is almost empty for large values of the interaction constant U. This stabilizes the breather state as only few atoms are subject to particle loss. For intermediate values of the interaction constant U, one also finds the characteristic bimodal number distribution in the first well. However, the particle number in the second well is larger, such that decay is much stronger.

The two breathers in site 1 and 3 are fully coherent, even for large interactions. To analyze the coherence of the the many-body quantum state $\hat{\rho}(t)$ in more detail, we first note that $\hat{\rho}(t)$ can be written as the incoherent sum of contributions with different total particle number n:

$$\hat{\rho}(t) = \sum_n p_n(t)\,\hat{\rho}^{(n)}(t). \tag{4.4}$$

There are no coherences between the contributions $\hat{\rho}^{(n)}(t)$ as particle loss proceeds via incoherent jumps only. Numerical results for the density matrix $\hat{\rho}^{(n)}(t)$ with $n = 50$ are shown in figure 4.3 (c,d) at time $t = 10\,J^{-1}$ after the formation of a breather state. We have plotted the matrix elements of $\hat{\rho}^{(n)}(t)$ for a subset of matrix indices, fixing $n_2 = n_2' = 0$ or $n_2 = n_2' = 1$, respectively. For this plot we simulated the dynamics with the quantum jump method using $L = 3000$ stochastic trajectories in total. One observes that the coherences, i.e. the off-diagonal matrix elements of the projected density matrix assume their maximum possible values,

$$|\rho_{n_1,n_1'}|^2 \approx |\rho_{n_1,n_1}|\,|\rho_{n_1',n_1'}|. \tag{4.5}$$

This shows that the two breathers formed at lattice sites 1 and 3 are indeed fully *coherent*. Breather states with different total particle number are generally not coherent as discussed above. However, this neither affects the entanglement of the particles nor its use in quantum interferometry.
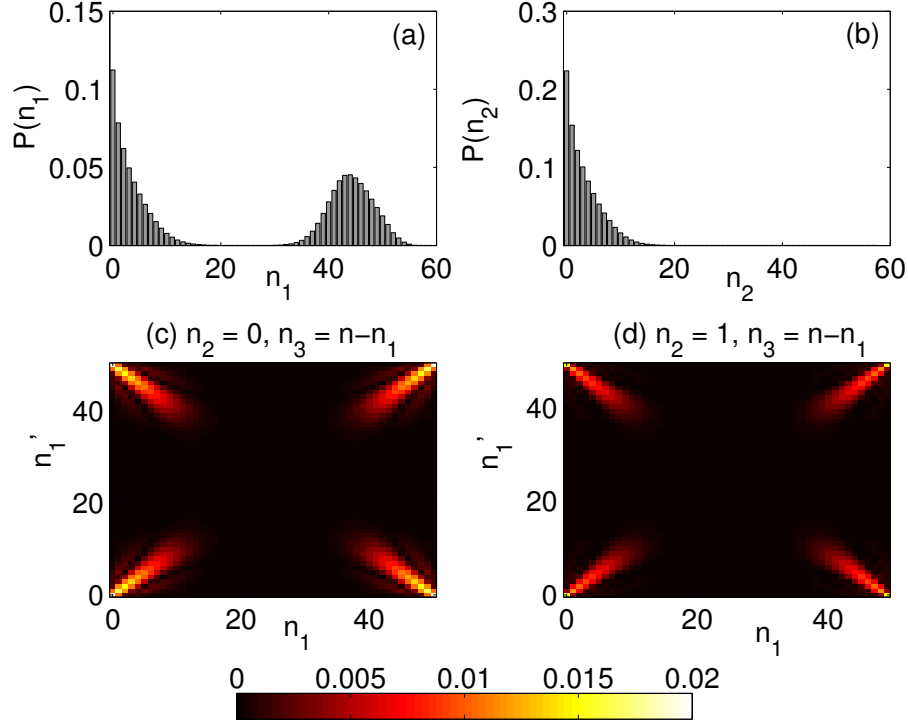
Figure 4.3: (a,b) *Full counting statistics of the breather state at time* $t = 10\,J^{-1}$ *in the first and second well.* (c,d) *Density matrix* $\rho(n_1, n_2, n_3; n_1', n_2', n_3')$ *of a breather state at time* $t = 10\,J^{-1}$ *for a fixed particle number* $n = 50$ *and* $n_2 = n_2' = 0$ *(c) and* $n_2 = n_2' = 1$ *(d), respectively. Parameters are* $U = 0.1\,J$ *and* $\gamma_2 = 0.2\,J$. *The initial state is a pure BEC with* $N = 60$ *particles and an anti-symmetric wave function* (4.15). *Taken from* [67].

Due to the almost perfect coherence of the modes, breather states enable new applications in precision quantum metrology. In particular, they generalize the so-called NOON states $|n, 0, 0\rangle + e^{i\alpha}|0, 0, n\rangle$ which enable precision interferometry beyond the standard quantum limit [43]. Breather states can be written as a superposition of states of the form

$$|n_1, n_2, n - n_1 - n_2\rangle + e^{i\alpha}|n - n_1 - n_2, n_2, n_1\rangle. \tag{4.6}$$

That is, the coherence of wells 1 and 3 is guaranteed as in an ordinary NOON state but the total number of particles forming the NOON state varies statistically. Nevertheless, this is sufficient for precision interferometry.
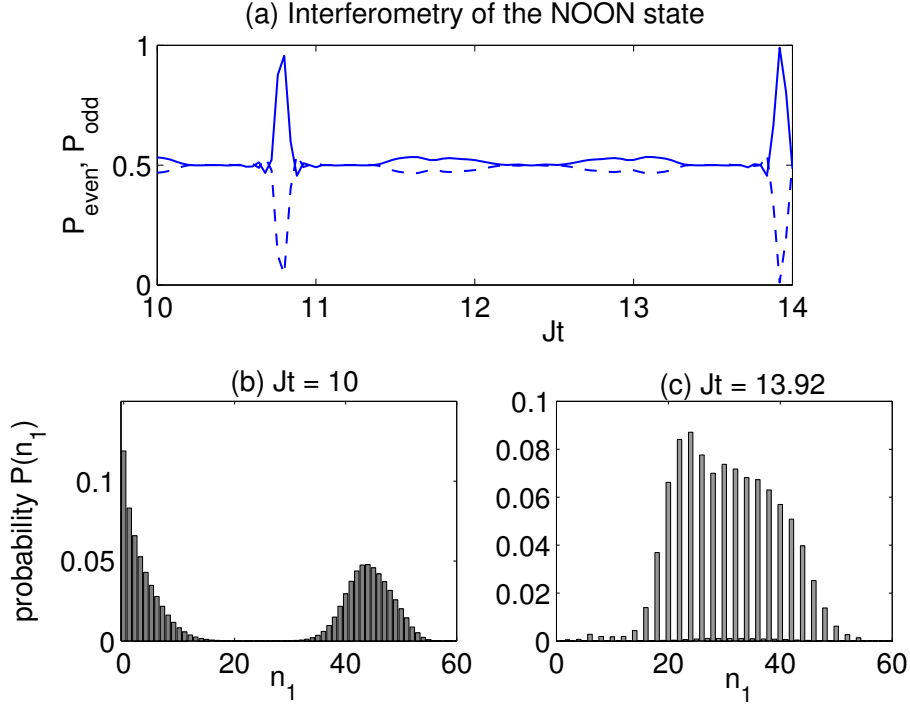
Figure 4.4: *Interferometry of the NOON state according to the time evolution $\hat{U}(t) = \exp[-J(\hat{\alpha}_1^\dagger\hat{\alpha}_3 - \hat{\alpha}_3^\dagger\hat{\alpha}_1)t]$. (a) Probability to detect an even (solid line) and an odd number of particles (dashed line) at site 1 as a function of time. Lower panels: Full counting statistics at site 1 at (b) the beginning of the interferometer stage $t = 10J^{-1}$ and (c) during the interferometer stage at $t = 13.92J^{-1}$, where $P_{even} = 1$. The breather state is generated starting from a BEC with an anti-symmetric wave function as shown in Fig. 4.1 with $U = 0.1J$ and $\gamma_2 = 0.2J$. During the interferometer stage we assume that $U = \gamma_2 = 0$. Taken from [67].*

4.1.4 Breather State: Interferometry

Starting from the breather state analyzed in the previous subsection, we consider an interferometric measurement, where the modes (lattice sites) 1 and 3 are mixed. Assuming that interactions (by tuning a Feshbach resonance) and losses are switched off, the dynamics during the interferometer stage is given by the time evolution operator

$$\hat{U}_{interferometer} = \exp[-i\hat{H}_{mix}t], \tag{4.7}$$

where $\hat{H}_{mix} = iJ(\hat{\alpha}_1^\dagger\hat{\alpha}_3 - \hat{\alpha}_3^\dagger\hat{\alpha}_1)$. In analogy to the parity observable in NOON state interferometry [44], we record the probability to detect either an even

or an odd number of particles in site 1. Such a measurement is automatically realized by the optical imaging apparatus in the experiments [31, 32].

The probability $P_{\text{even,odd}}$ to detect an even or an odd number of particles is plotted in figure 4.4 (a) as a function of time. P_{even} approaches unity periodically at times

$$t_{\text{rev}} = \left(n + \frac{1}{4} \right) \pi \, J^{-1}, \qquad n = 0, 1, 2, \ldots, \tag{4.8}$$

which unambiguously proves the coherence of the breather state. Figure 4.4 (b,c) shows the full counting statistics in site 1 at the beginning of the interferometer stage at $t = 10 J^{-1}$ and during the interferometer stage at $t = 13.92 J^{-1}$. Destructive interference forbids to detect an odd number of particles at this time, such that $P_{\text{even}}(t)$ approaches unity.

The interference fringes observed for $P_{\text{even,odd}}(t)$ are extremely sharp, which enables precision measurement beyond the standard quantum limit. In the present setup, the detection of a fringe reveals the value of the tunneling rate J with ultra-high precision via equation (4.8). Different quantities can be measured by a modified interferometry scheme as described in [44]. An important but very difficult goal is to increase the number of particles forming a NOON state (see, e.g., [33]), as the measurement uncertainty of this method scales inversely with the particle number N. This goal may be archived with the breather states discussed here which are readily generated also for large samples.

4.1.5 Entanglement and Decoherence

The particles in a breather or NOON state are strongly entangled. This means that if some particles are measured at one site, then the remaining particles will be projected onto the same site with overwhelming probability. To unambiguously detect this form of multi-particle entanglement, we analyze the variance of the population imbalance $\Delta(\hat{n}_3 - \hat{n}_1)^2$, which scales as $\sim n_{\text{tot}}^2$ for a breather state, while it is bounded by n_{tot} for a pure product state, n_{tot} being the total particle number. The variance can thus serve as an entanglement criterion, if the quantum state is pure or, more importantly, if one can assure that a large value of the variance is not due to a incoherent mixture of states localized at site 1 or 3.

We assume that a quantum state is decomposed into pure states, $\hat{\rho} = L^{-1} \sum_{a=1}^{L} |\psi_a\rangle\langle\psi_a|$, as it is automatically the case in a quantum jump simu-
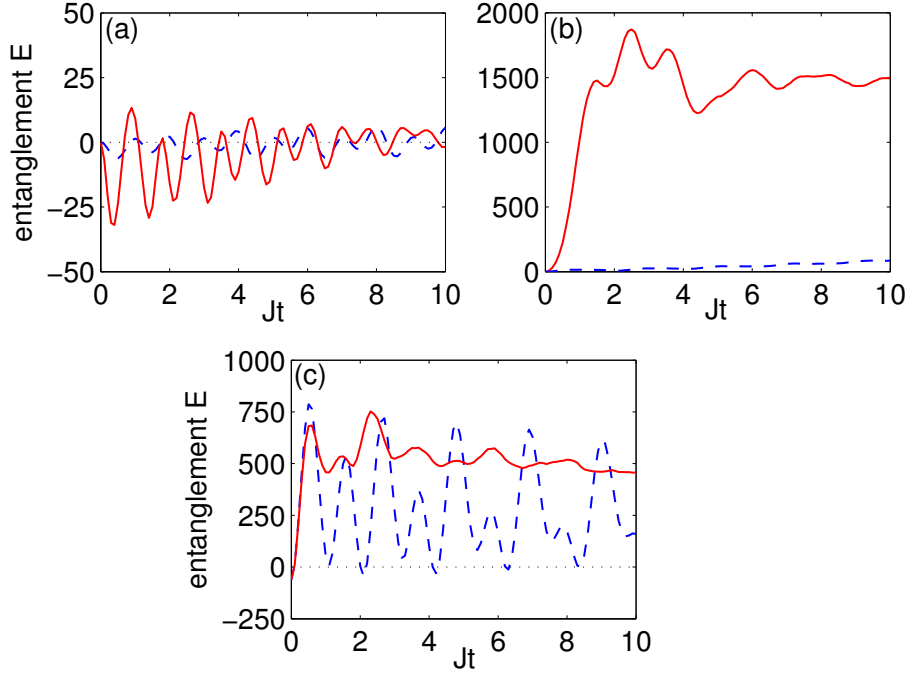
Figure 4.5: *Evolution of the entanglement parameter* (4.9) *for three different initial states:* (a) *a BEC with symmetric wave function* $|\Psi_+\rangle$, (b) *a BEC with an anti-symmetric wave function* $|\Psi_-\rangle$ *and* (c) *a Fock state* $|\Psi_F\rangle$. *Parameters are* $\gamma_2 = 0.2J$, $U = 0.01J$ *(dashed blue lines) and* $U = 0.1J$ *(solid red line), respectively.* Taken from [67].

lations [93]. We then introduce the entanglement parameter

$$
\begin{aligned}
E_{r,q} \; := \; & \langle (\hat{n}_r - \hat{n}_q)^2 \rangle - \langle \hat{n}_r - \hat{n}_q \rangle^2 - \langle \hat{n}_r + \hat{n}_q \rangle \\
& - \frac{1}{2L^2} \sum_{a,b} \left[\langle (\hat{n}_r - \hat{n}_q) \rangle_a - \langle (\hat{n}_r - \hat{n}_q) \rangle_b \right]^2 ,
\end{aligned}
\tag{4.9}
$$

for the wells (r, q), where $\langle \cdot \rangle_{a,b}$ denotes the expectation value in the pure state $|\psi_{a,b}\rangle$. The last term in the parameter $E_{r,q}$ corrects for the possibility of an incoherent superposition of states localized at sites 1 and 3. For a separable quantum state one can now show that $E_{j,k} < 0$ such that a value $E_{j,k} > 0$ unambiguously proves entanglement of the particles. The detailed derivation is given in appendix C.

Figure 4.5 shows the evolution of the entanglement parameter $E_{1,3}(t)$ for three different initial states. The symmetric state $|\Psi_+\rangle$ remains close to a pure BEC, such that $E_{1,3}(t) \approx 0$ for all times. In contrast, the anti-symmetric state $|\Psi_-\rangle$ and the Fock state $|\Psi_F\rangle$ relax to strongly entangled breather states

if interactions are sufficiently strong. In this case we observe large positive values of the entanglement parameter $E_{1,3}(t) \approx 1500$ and $E_{1,3}(t) \approx 500$, respectively, which clearly reveals the presence of many-particle entanglement. Notably, entanglement is also generated for the Fock state $|\Psi_F\rangle$ in the regime of weak interactions $U = 0.01J$. However, this is only a transient phenomena caused by interference effects. The breather states formed in the case of strong interactions are metastable such that the generated entanglement persists for long times until all particles decay from the trap. Thus, localized particle dissipation enables the robust, deterministic generation of entanglement only in the presence of strong interactions.

Furthermore, entangled breather states provide a sensitive probe for environmentally induced decoherence. Figure 4.6 (a) shows the evolution of the entanglement parameter $E_{1,3}(t)$ for three different values of the strength of phase noise κ starting from the anti-symmetric initial state $|\Psi_-\rangle$. Entanglement is generated in all cases, but $E_{1,3}(t)$ rapidly decreases again when κ is large due to the decoherence of the breathers. Notably, one finds strong number fluctuations $g_{1,1}^{(2)} > 1$ and anti-correlations $g_{1,3}^{(2)} < 1$ also in the presence of strong phase noise, but interferometry is no longer possible. Figure 4.6 (b) shows the maximum value of $E_{1,3}(t)$ realized in the presence of phase noise. Entanglement decreases with the noise rate κ, in which breather states with large particle numbers are most sensitive. However, entanglement persists up to relatively large values of $\kappa \approx 10^{-2}J$ in all cases.

4.2 Semiclassical Interpretation

The semi-classical phase space picture can help us understand the formation of the breather state. Any quantum state can be represented by a quasi distribution function on the associated classical phase space without loss of information, such as the Wigner or the Husimi function [96]. In the following, we make use of both distribution functions which are defined as

$$Q(\alpha_1, \ldots, \alpha_M; t) := \langle \alpha_1, \ldots, \alpha_M | \hat{\rho}(t) | \alpha_1, \ldots, \alpha_M \rangle \quad (4.10)$$

and

$$\begin{aligned}
\mathcal{W} \;&:= \; \frac{1}{\pi^M} \int \prod_j d^2\beta_j \, \exp\left[\sum_j \alpha_j \beta_j^* - \alpha_j^* \beta_j\right] \\
&\quad \times \langle \alpha_1 - \beta_1, \ldots, \alpha_M - \beta_M | \hat{\rho} | \alpha_1 + \beta_1, \ldots, \alpha_M + \beta_M \rangle \quad (4.11)
\end{aligned}$$

respectively. Here, $|\alpha_j\rangle$ is a Glauber coherent state in the jth well and M is the number of lattice sites. The evolution equations of these distribution
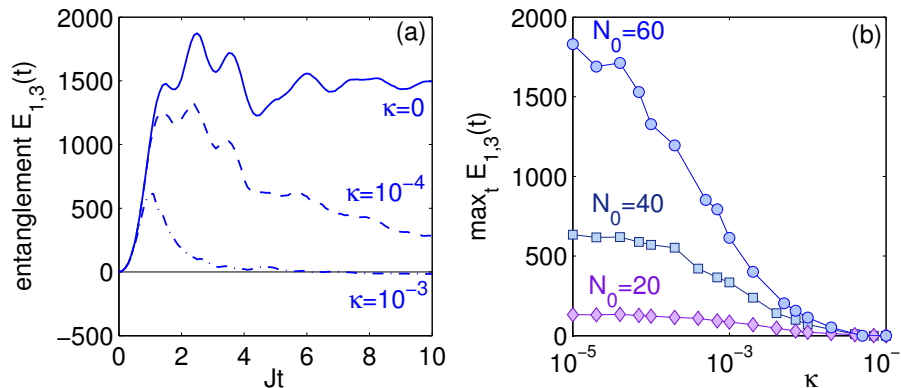
Figure 4.6: *Entanglement and decoherence of a breather state in the presence of phase noise* (a) *Evolution of the entanglement parameter* (4.9) *for the anti-symmetric initial state* $|\Psi_-\rangle$ *and* $\kappa = 0$ *(solid line),* $\kappa = 10^{-4}J$ *(dashed line) and* $\kappa = 10^{-3}J$ *(dash-dotted line) and* $n_{\text{tot}}(0) = 60$. (b) *Temporal maximum of the entanglement parameter* $\max_t E_{1,3}(t)$ *as a function of the phase noise rate* κ *for the anti-symmetric initial state* $|\Psi_-\rangle$ *and different particle numbers. Parameters are* $U = 0.1J$ *and* $\gamma_2 = 0.2J$. *Taken from* [67].

functions can be calculated systematically using the operator correspondence discussed in [96]. The evolution equation for the Wigner function is discussed in detail in appendix B.

A general feature is that the dynamics of the phase space quasi distribution functions is, to leading order in $1/N$, given by a classical Liouville equation,

$$\frac{\partial Q}{\partial t} = -\sum_j \left(\frac{\partial}{\partial \alpha_j} \dot{\alpha}_j + \frac{\partial}{\partial \alpha_j^*} \dot{\alpha}_j^* \right) Q + \text{noise}. \qquad (4.12)$$

Due to the structure of the evolution equation (4.12), the "classical Liouvillian" flow provides the skeleton of the quantum dynamics (see M. Berry's quote in [100]) of the Husimi or Wigner function, whereas the quantum corrections vanish with increasing particle number as $1/N$ [97]. In particular, the Liouvillian approximation neglects phase-space interference effects as well as (anti-)diffusion terms which lead to an elongation of the Wigner- and the Husimi-function [98]. The associated classical flow is given by the dissipative discrete Gross-Pitaevskii equation (DGPE) [55–57]

$$i\dot{\alpha}_j = -J(\alpha_{j+1} - \alpha_{j-1}) + U|\alpha_j|^2 \alpha_j - i\gamma_j \alpha_j/2 \,. \qquad (4.13)$$

Figure 4.7 (a) shows three trajectories of the DGPE for different initial values of the $\alpha_j = |\alpha_j|e^{i\phi_j}$. We have plotted the evolution of the population
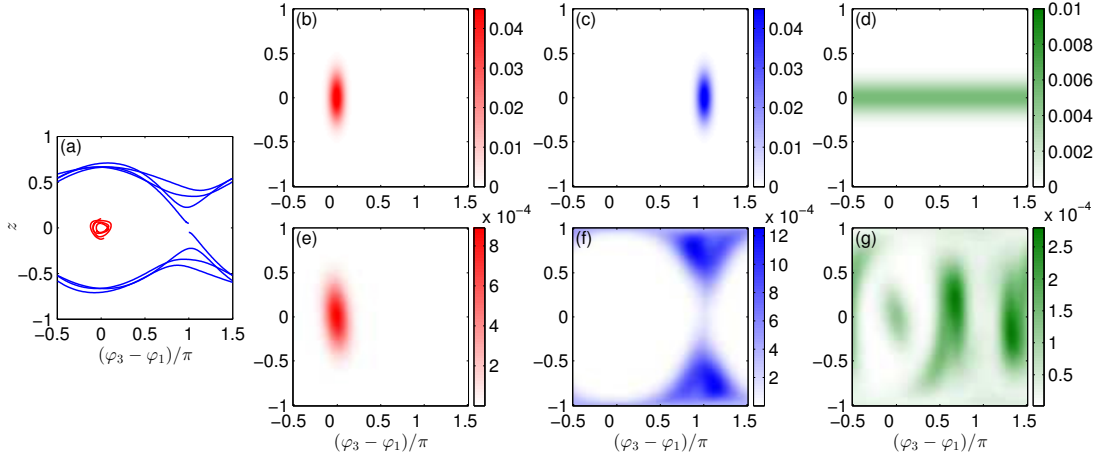
Figure 4.7: *Semiclassical interpretation of breather state formation. (a) Classical trajectories starting in the vicinity of the symmetric states $(\alpha_1, \alpha_2, \alpha_3) = (1, 0, 1)/\sqrt{2}$ (red) and the anti-symmetric states $(1, 0, -1)/\sqrt{2}$ (blue). (b-g) The quantum dynamics of the Husimi Q function follows the classical phase space trajectories. (b,e) A BEC with a symmetric wave function $|\Psi_+\rangle$ remains approximately pure. (c,f) A BEC with an anti-symmetric wave function $|\Psi_-\rangle$ is coherently split into two parts forming the breather state. (d,g) A number state $|\Psi_F\rangle$ is also split into two parts, but number fluctuations and correlations are less pronounced. The Husimi function $Q(\alpha_1, \alpha_2, \alpha_3)$ is plotted as a function of the population imbalance $z = (|\alpha_3|^2 - |\alpha_1|^2)/n_{\text{tot}}$ and the relative phase $\phi_3 - \phi_1$ for $\alpha_2 = 0$ and $|\alpha_1|^2 + |\alpha_3|^2 = n_{\text{tot}}$ at times $t = 0$ (b-d) and $t = 10J^{-1}$ (e-g). Here, n_{tot} denotes the total particle number at the respective time. Parameters are $U = 0.1J$, $\gamma_2 = 0.2J$ and $N(0) = 60$. Taken from [67].*

imbalance between the first and third site $z = (|\alpha_3|^2 - |\alpha_1|^2)/n_{\text{tot}}$ vs. the relative phase $\Delta\phi = \phi_3 - \phi_1$. One observes that the trajectory starting at $\Delta\phi = 0$ (red) is dynamically stable, such that it remains in the vicinity of the point $(z, \Delta\phi) = (0, 0)$ for all times. In contrast, trajectories starting close to $(z, \Delta\phi) = (0, \pi)$ converge to regions with either $z > 0$ or $z < 0$. These regions correspond to self-trapped states, which are known from the non-dissipative case [25, 37, 38]. For $\gamma_2 > 0$, these states become *attractively stable*, which enables the dynamic formation of breather states.

The corresponding quantum dynamics of an initially pure BEC with a (anti-) symmetric $|\Psi_\pm\rangle$ wave function is shown in figure 4.7 (b,e) and (c,f), respectively. The Husimi function of the initial states are localized around $(z, \Delta\phi) = (0, 0)$ and $(z, \Delta\phi) = (0, \pi)$ as shown in figure 4.7 (b,c). The
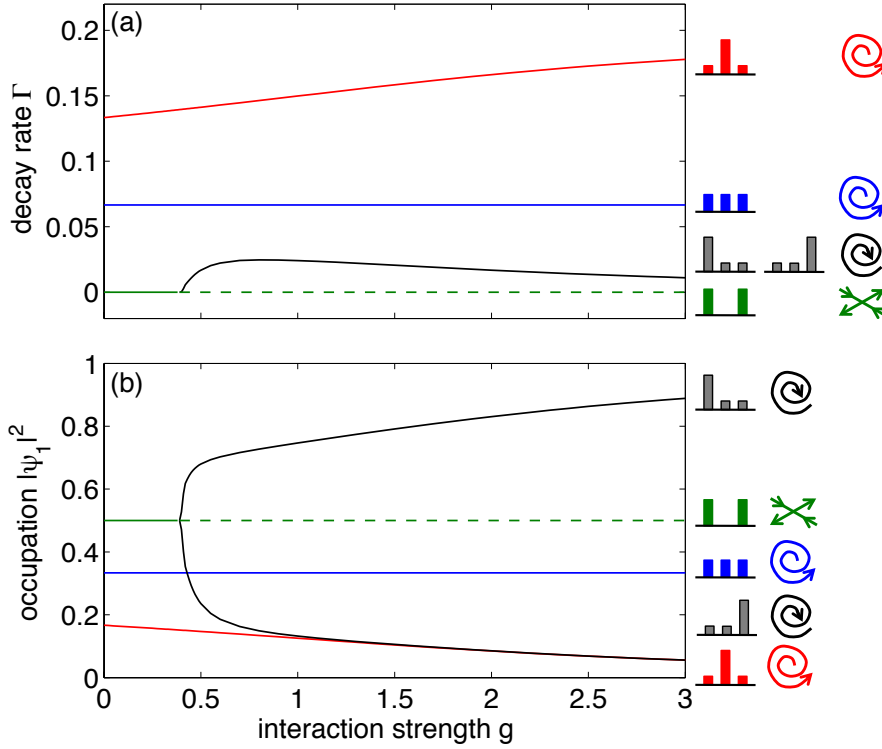
Figure 4.8: *Properties of the meta-stable solutions of the non hermitian DGPE (4.14) for $J = 1$ and $\gamma_2 = 0.2$ as a function of the interaction strength $g = Un_{\text{tot}}$. (a) Decay rate per particle Γ and (b) relative occupation of the first well $|\alpha_1|^2$. The icons on the right indicate the density distribution in the three wells and the dynamical stability for large g.* Taken from [67].

DGPE then predicts the flow of the Husimi function on a coarse grained scale. Trajectories starting in the vicinity of $(z, \Delta\phi) = (0, 0)$ remain close to their initial states and so does the Husimi function of the symmetric state $|\Psi_+\rangle$. In contrast, the Husimi function splits up into two fragments localized in the self-trapping regions of phase space for the anti-symmetric initial state $|\Psi_-\rangle$ – a breather state is formed. Finally, in figure 4.7 (d) the Husimi function of a Fock state is depicted. In this case also the dynamics leads to the split of the function in two parts, as figure 4.7 (g) illustrates. However, the number fluctuations and correlations are less pronounced.

The semi-classical picture predicts the fragmentation of the condensate but, of course, cannot assert the coherence and thus the entanglement of the fragments which is a genuine quantum feature. However, it correctly predicts the stability of an initial state and the emergence of breathers. Thus we can
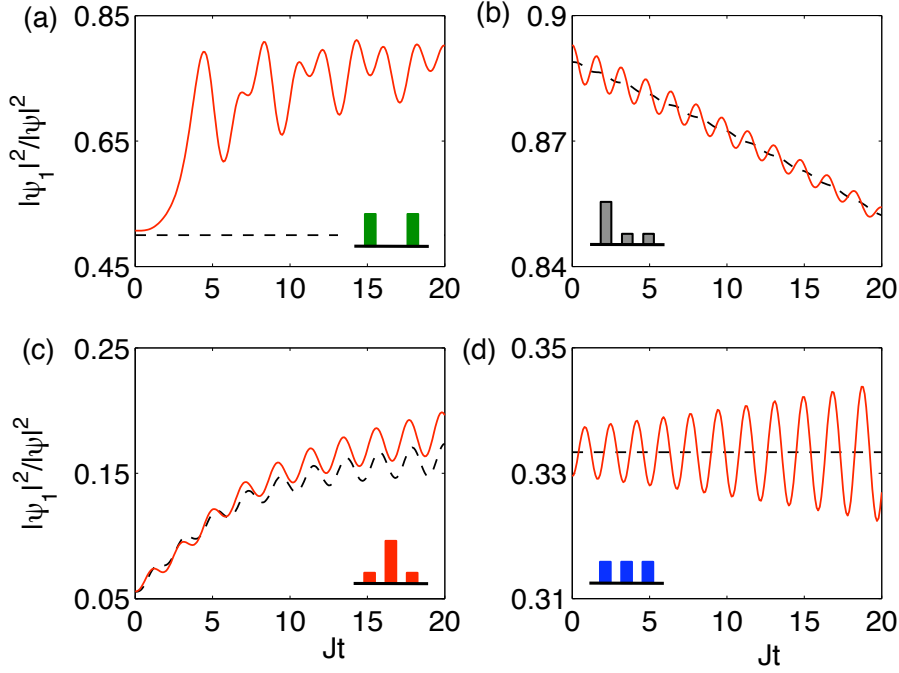
Figure 4.9: *Analysis of the dynamical stability of the meta-stable solutions of the DGPE (4.14) for $J = 1$, $Un_{\mathrm{tot}} = 3$ and $\gamma_2 = 0.2$. The dynamics has been simulated starting from a meta-stable state (black line) and the state plus a small perturbation of order 0.01 (red line). Plotted is the relative occupation of the first well $|\alpha_1(t)|^2/\|\vec{\alpha}(t)\|^2$. The density distribution of the initial states are illustrated by the icons in the corners:* (a) *the anti-symmetric state,* (b) *a breather in the first well,* (c) *a breather in the leaky second well and* (d) *the balanced state.* Taken from [67].

infer the critical interaction strength for the transition to the breather regime from the associated "classical" dynamics. To this end we analyze the meta-stable states of the DGPE which are defined as the solutions of the equation

$$-J(\alpha_{\ell-1} + \alpha_{\ell+1}) + U|\alpha_\ell|^2\alpha_\ell - i\frac{\gamma}{2}\delta_{\ell,2}\alpha_\ell = (\mu - i\Gamma/2)\,\alpha_\ell. \qquad (4.14)$$

Here and in the following, we denote by $\vec{\alpha} = (\alpha_1, \ldots, \alpha_M)^t$ the vector of all amplitudes α_j. The meta-stable states are not stationary states of the DGPE in a strict sense, as the norm and thus the effective nonlinearity $g = U\|\vec{\alpha}\|^2$ decays with a rate Γ. However, if decay is slow enough and if the solutions are dynamically stable, the time evolution will follow these quasi steady states adiabatically (cf., e.g., [101]).

The properties of the meta-stable states, their decay rate and their den-

sity distribution are summarized in figure 4.8 as a function of the effective nonlinearity g. In the linear case $g = 0$, three solution exist which are obtained by a simple diagonalization of the single-particle Hamiltonian. Of particular interest is the anti-symmetric state

$$\vec{\alpha}_{\mathrm{as}} = \frac{1}{\sqrt{2}}(1, 0, -1), \tag{4.15}$$

which exists for all g and has a vanishing decay rate Γ. With increasing interaction strength g, new solutions come into being. At a critical value $g_{\mathrm{cr}} = 0.4$, the anti-symmetric state $\vec{\alpha}_{\mathrm{as}}$ bifurcates and two breather solutions emerge. These breathers are strongly localized in one of the non-decaying wells $j = 1, 3$. Due to the symmetry of the system, both have the same decay rate Γ.

For weak interactions, the state $\vec{\alpha}_{\mathrm{as}}$ dominates the dynamics as its decay rate Γ vanishes. However, this is no longer possible for $g > g_{\mathrm{cr}}$ as these states become dynamically unstable as shown in figure 4.9 (a). Instead, the breathers dominate the dynamics. Their decay rate is rather small [46, 47, 56, 69] and, most importantly, they are attractively stable as shown in figure 4.9 (b). Thus, a breather is formed dynamically during the time evolution for most initial conditions if g is large enough. The remaining meta-stable states are marginally unstable as shown in figure 4.9 (c,d).

4.3 Decay in Extended Lattices

A breather state emerges also in extended lattices, if the interaction strength exceeds a critical value. In the following we analyze the breather formation quantitatively and derive a formula for the critical interaction strength, which depends on the size of the optical lattice. The results presented in this section should be observable in ongoing experiments with ultracold bosons in quasi one dimensional optical lattices [27, 29]. As exact numerical simulations of the many-body quantum dynamics are no longer possible for extended lattices with many particles, we use the truncated Wigner method (see appendix B for details). This approximate method is appropriate for a system with large filling factors, since in this case the error induced from the truncation vanishes as $1/N$ [97, 98]. More importantly for our case, the truncated Wigner method can describe the deviation from a pure BEC state, in contrast to pure mean-field models [55, 56, 70].
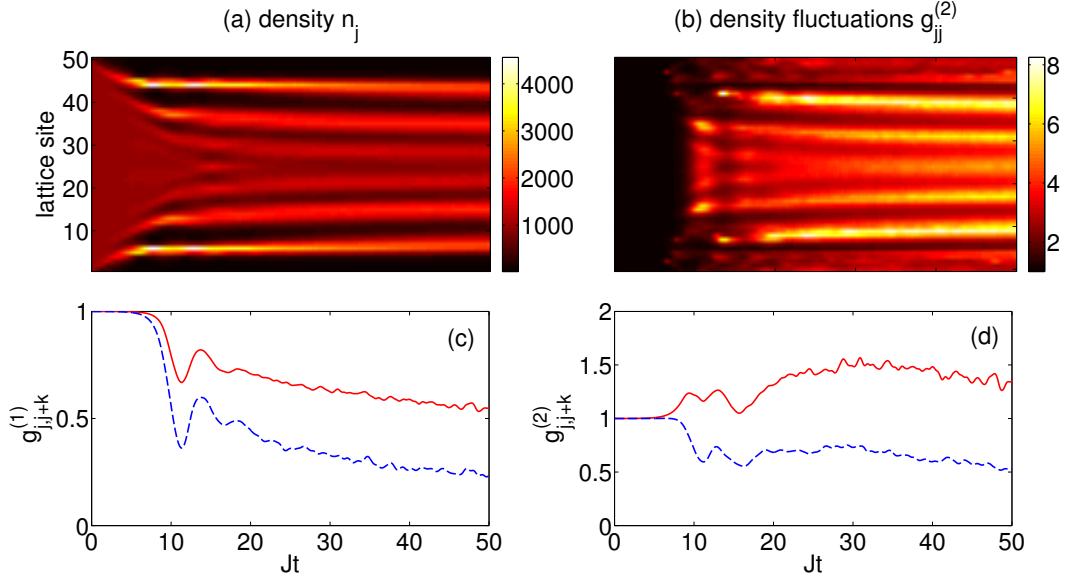
Figure 4.10: *Dynamics of a leaky Bose-Hubbard chain with 50 wells. We have plotted* (a) *the particle density* $\langle \hat{n}_j(t) \rangle$, (b) t*he density fluctuations* $g_{j,j}^{(2)}(t)$ *in each lattice site as well as* (c) *the phase coherence* $g_{j,j+k}^{(1)}(t)$ *and* (d) *the density-density correlations* $g_{j,j+k}^{(2)}(t)$ *between site* $j = 25$ *and the neighboring sites* $k = 1$ *(solid red line),* $k = 2$ *(dashed blue line). Parameters are* $U n_{\text{tot}}(0) = 25J$, $\gamma_1 = 2J$, $M = 50$ *and* $\rho(t = 0) = n_{\text{tot}}(0)/M = 1000$.

4.3.1 Breather State Formation

In the following we consider an extended optical lattice consisting of $M = 50$ sites with periodic boundary conditions unless states otherwise. Loss occurs from the lattice site $j = 1$ only. As initial state we assume a pure BEC which is moved at constant speed [34] or accelerated [35] to the edge of the first Brillouin zone. Hence the quantum state of the particles at $t = 0$ is given by

$$|\Psi(0)\rangle = \frac{1}{\sqrt{N!}} \left(\sum_{j=1}^{M} \psi_j \hat{a}_j^\dagger \right)^N |0\rangle \qquad (4.16)$$

with $\psi_j = (-1)^j/\sqrt{M}$, which generalizes the antisymmetric initial state $|\Psi_-\rangle$ discussed for the triple-well trap. We consider the case of large filling factors, with $N/M = 1000$ in all simulations.

For weak interactions the quantum state remains close to a pure BEC during the decay, such that all coherence functions are approximately one. The dynamics changes dramatically for strong interactions as shown in fig-
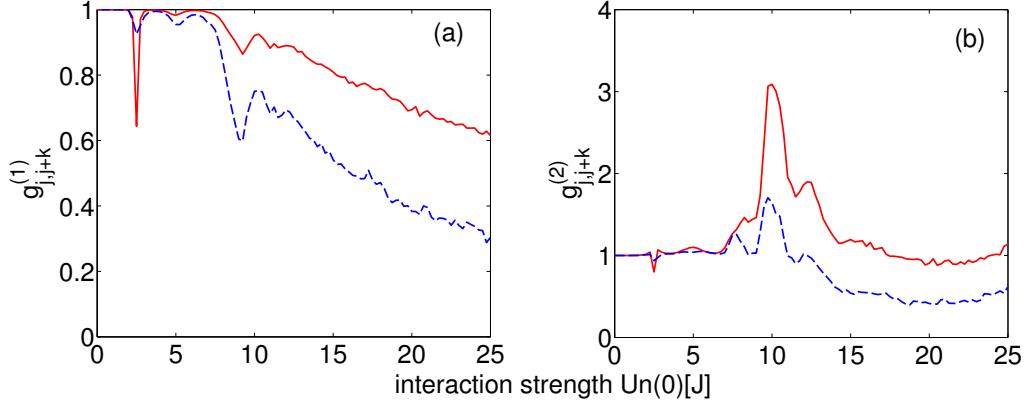
Figure 4.11: *Transition to the breather regime in an open optical lattice. Shown is* (a) *the the phase coherence $g^{(1)}_{j,j+k}$ and* (b) *the number correlation function $g^{(2)}_{j,j+k}$ between site $j = 9$ and the neighboring sites $k = 1$ (solid red line) and $k = 2$ (dashed blue line), respectively, after a fixed propagation time $t_{\text{final}} = 50J^{-1}$. One observes a sharp transition when the interaction strength $Un_{\text{tot}}(0)$ exceeds a critical value of approx. $2.5J$. Parameters are $\gamma_1 = 2J$, $M = 50$ and the particle density is $\rho(t = 0) = N/M = 1000$.*

ure 4.10. The phase coherence $g^{(1)}_{j,k}$ between adjacent wells is lost after a short transient period, indicating the dynamical instability of the condensate. At the same time the number fluctuations $g^{(2)}_{j,j}$ rapidly increase as shown in figure 4.10 (b). This reveals a strong spatial bunching of the particles as expected for a breather state. This feature of the dissipative equilibrium state is in strong contrast to the non-dissipative case, where repulsive inter-actions *suppress* number fluctuations in thermal equilibrium. Part (d) of the figure reveals the second characteristic trait of the breather state. Strong anti-correlations with $g^{(2)}_{j,j+2} \approx 0.5$ are observed between the site $j = 25$ and the next-to-nearest neighbor. No anti-correlations are observed for the direct neighbor, as breathers can extend over more than one site in an extended lattice. We thus conclude that the particles tend to bunch at one site of the lattice, leaving the neighboring sites essentially empty. This is exactly the signature of the breather state in the extended lattice, which we have discussed above for the trimer case. The position of the individual breathers in this breather state is random due to the quantum fluctuations. We note that it can be experimentally easier to prepare breather states starting from a Mott insulator instead of a BEC at the band edge. Simulations for small lattices show the development of strong density anti-correlations and multi-particle entanglement also in this case.

The transition to the breather regime for strong interactions is further analyzed in figure 4.11, which shows the first and second order coherence functions as a function of the interaction strength for a fixed propagation time $t_{\text{final}} = 50\,J^{-1}$ at the reference site $j = 9$. For $UN(0) \lesssim 2.5\,J$ the phase coherence between neighboring sites is preserved, while the particles decay from the lattice. For stronger interactions, however, phase coherence is lost and the BEC fragments into a breather state. The second order correlation function $g_{j,j+2}^{(2)}$ reveals the existence of strong anti-correlations for large values of U. However, we observe $g_{j,j+2}^{(2)} > 1$ in the vicinity of the transition point. This is a consequence of the localization of the breathers, which becomes tighter with increasing U [47]. Directly above the transition breathers exist, but typically extend over several lattice sites, such that we observe positive correlations at this length scale. Moreover, the formation of breathers suppresses the decay from the lattice, that is, the total particle number decreases more slowly. This is due to the strong localization of the breathers preventing particles from tunneling to the leaky lattice sites.

Here it must be noted that the coherence functions show the same qualitative behavior if another lattice site is chosen as a reference site instead of $j = 25$ or $j = 9$. The oscillations we observe in figure 4.11 (b) and for intermediate values of U are just a manifestation of the temporal oscillations of the $g^{(1)}$ and $g^{(2)}$, as shown in figure 4.10 (c) and (d).

4.3.2 Critical Interaction Strength

Breather formation sets in abruptly when the interaction strength exceeds a critical value U_{crit}. Extensive numerical simulations show that the transition point depends on the size of the lattice, i.e. the number of sites M, as shown in figure 4.12. As the lattice becomes larger, breather formation is facilitated such that the critical value U_{crit} decreases rather rapidly. In these simulations, U_{crit} was determined as follows. After a fixed propagation time we find the values of the density fluctuations $g_{j,j}^{(2)}$ for different interaction strengths U and for various lattice sites j. We identified the critical interaction as the maximum interaction strength in which the density fluctuations at all sites j differ from the value in the non-interacting case, $g_{j,j}^{(2)} = 1$, by less than 5%. In all simulations we have used $\gamma_1 = 2J$ and the same initial density, $\rho(t = 0) = N/M = 1000$. In the following we derive a formula for the critical interaction strength, which will also clarify the microscopic origin of breather formation and its connection to the self-trapping effect. Our considerations follows the reasoning presented in [70] for the analogous mean-field system.

As shown in [70], breathers formation is a local process, which occurs if
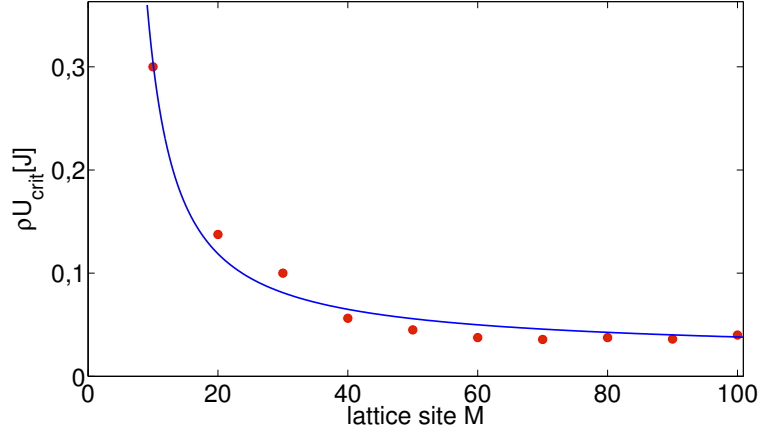
Figure 4.12: *The critical nonlinearity ρU_{crit}, at which breathers start to form, as a function of the lattice size M. Numerical results using the truncated Wigner method (blue circles) are compared to a fit using equation (4.19) (red line). The fitting parameters we found are $L = 0.075$ with bounds $(0.054, 0.096)$ and $P_{\mathrm{th}} = 1 - 2.4 \times 10^{-7}$ with bounds $(1 + 4.54 \times 10^{-7}, 1 - 9.3 \times 10^{-7})$, while the summed square of residuals is $SSE = 1.2 \times 10^{-3}$. The other parameters are $\gamma_1 = 2J$ and $\rho(t = 0) = N/M = 1000$.*

the local effective nonlinearity exceeds a critical value L

$$Un_j/J \leq L \tag{4.17}$$

for at least one lattice site j. Then the nonlinearity is strong enough to induce self-trapping at the respective lattice site (cf. also [25, 37, 38]). Starting from this local ansatz, the critical interaction strength can be inferred as follows. Breathers are observed if the probability to satisfy condition (4.17) exceeds a certain threshold value

$$\mathrm{prob}(\exists\, j : n_j > JL/U) \geq P_{\mathrm{th}}. \tag{4.18}$$

Hennig and Fleischmann [70] furthermore argue that the probability to observe a certain particle number n_j follows a Poissonian distribution in the diffusive regime, such that the cumulative distribution function is given by $\mathrm{prob}(n_j < n_{\mathrm{crit}}) = 1 - e^{-Mn_{\mathrm{crit}}/N}$. Using this result for a single lattice site, one calculate the probability to find at least one $n_j \geq n_{\mathrm{crit}} = JL/U$:

$$
\begin{aligned}
\mathrm{prob}(\exists\, j : n_j > n_{\mathrm{crit}}) &= 1 - \mathrm{prob}(n_j < n_{\mathrm{crit}}\ \forall j) \\
&= 1 - (1 - e^{-Mn_{\mathrm{crit}}/N})^M.
\end{aligned}
$$

Substituting this result into equation (4.18) and solving for U then yields the following condition for the onset of breather formation

$$U\rho \geq U_{\text{crit}}\rho = \frac{-JL}{\log[1-(1-P_{\text{th}})^{1/M}]} \, , \tag{4.19}$$

where $\rho = N/M$ is the particle density.

The analytic prediction (4.19) depends on two parameters L and P_{th}, which are used as fit parameters to model the numeric results. This fit yields an excellent agreement with the numeric results as shown in figure 4.12. We stress that the decrease of U_{crit} with increasing lattice site cannot be modeled by a simple algebraic or exponential decay. Notably, we obtain significantly smaller values for U_{crit} than in [70]. This is attributed to the fact that the unstable initial state considered here, a BEC at the band edge, has a higher energy and thus fragments into breathers much more easily.

4.4 Conclusions

In this chapter we have discussed how particle losses combined with strong interparticle interactions and discrete geometry can deterministically lead to the formation of quantum superpositions of discrete breathers. For a small trimer system we have discussed the properties of these "breather states" in detail including entanglement, decoherence and possible applications in precision quantum interferometry. A semiclassical interpretation of breather state formation has revealed the connection to a classical bifurcation of the associated mean-field dynamics. Furthermore, we have studied the dynamical formation of breather states in extended lattices and we have derived a formula which predicts the critical interaction strength, in which the breathers start to form, in lattices with different size. The formation and the properties of these structures could be readily observed in ongoing experiments with ultracold atoms in optical lattices [27, 31, 32, 36].

Chapter 5

Non-Equilibrium Transport in Bose-Hubbard Chains

The technological advances of the last decades made feasible the creation of extremely small devices, which opened the possibility to realize logic structures on the atomic level [79–82]. At these scales however quantum effects are present, so many-body correlation effects on particle transport are important. These ideas created interest for the investigation of transport of ultracold atoms in systems with reduced dimensionality. The transport of fermionic and bosonic ultracold atoms in quantum wires and in one-dimensional optical lattices have been studied in [83–88]. A cold-atom analog of a mesoscopic conductor has been experimentally realized by dividing a macroscopic atomic cloud using a laser beam [92]. Moreover, it has been proposed the creation of bosonic analogues to the mesoscopic systems used in electronic devices, like a diode or field-effect transistor, the so-called atomtronics [89–91].

In this chapter we focus on the bosonic transport through a Bose-Hubbard chain coupled to two bosonic reservoirs, which keep the system far from equilibrium. In [78] we have treated the same system by using approximations based on the non-equilibrium Green's function formalism and compare the results with the truncated Wigner approximation. Here we will use mainly the truncated Wigner method for our simulations. In section 5.1 we introduce a simple model to study transport through a Bose-Hubbard chain, which uses the Master equation formalism. In the next section we investigate the behavior of currents and coherence functions in an out-of-equilibrium system, in the presence of weak and strong interparticle interactions. Finally, in sections 5.3 and 5.4 we study the transport through a single interacting and non-resonant site, respectively.
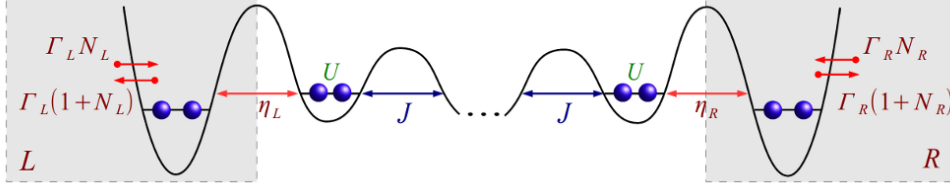
Figure 5.1: *Schematic of a Bose-Hubbard chain coupled to two bosonic reservoirs.*

5.1 A Bose-Hubbard Chain Coupled to Reservoirs

The electronic (fermionic) transport through mesoscopic devices has been extensively studied due to its technological applications. From the other hand, bosons present the advantage of occupying the same place in space even when they have the same energy, which is impossible to achieve with electrons. So the the first obvious question is about the differences between the bosonic and fermionic transport. Furthermore, can we use these differences to engineer mesoscopic bosonic systems with the properties we desire? To start answer these questions we need to create a steady state current along an optical lattice filled with ultracold bosonic atoms.

Inspired by the case of the single noninteracting site coupled to a thermal reservoir, we discussed in section 1.4, we will create two reservoirs by using appropriate creation and destruction of particles in the outer sites of a lattice. So, our system consists of a lattice, with $M+2$ sites, in which in the outer two wells we destroy and create single particles with rates $\Gamma_i(1 + N_i)$ and $\Gamma_i N_i$, respectively (see figure 5.1). These simultaneous destruction and creation of particles with these specific rates has as a consequence to control and keep constant the particle number in the outer wells in the whole evolution.

Indeed it is easy to see that the population of the outer wells remain constant. The Master equation that describes now our system is given by

$$
\begin{aligned}
\frac{\partial}{\partial t}\hat{\rho}(t) \;=\; & -i[\hat{H}, \hat{\rho}(t)] - \\
& - \sum_{k=R,L} \left\{ \frac{\Gamma_k(1 + N_k)}{2}[\hat{\alpha}_k^\dagger \hat{\alpha}_k \hat{\rho}(t) + \hat{\rho}(t)\hat{\alpha}_k^\dagger \hat{\alpha}_k - 2\hat{\alpha}_k \hat{\rho}(t)\hat{\alpha}_k^\dagger] + \right. \\
& \left. + \frac{\Gamma_k N_k}{2}[\hat{\alpha}_k \hat{\alpha}_k^\dagger \hat{\rho}(t) + \hat{\rho}(t)\hat{\alpha}_k \hat{\alpha}_k^\dagger - 2\hat{\alpha}_k^\dagger \hat{\rho}(t)\hat{\alpha}_k] \right\},
\end{aligned} \qquad (5.1)
$$

where

$$\hat{H} = -J\sum_{j=1}^{M-1}\left(\hat{\alpha}_{j+1}^{\dagger}\hat{\alpha}_j + \hat{\alpha}_j^{\dagger}\hat{\alpha}_{j+1}\right) + \frac{U}{2}\sum_{j=1}^{M}\hat{\alpha}_j^{\dagger}\hat{\alpha}_j^{\dagger}\hat{\alpha}_j\hat{\alpha}_j -$$
$$-\eta_L\left(\hat{\alpha}_1^{\dagger}\hat{\alpha}_L + \hat{\alpha}_L^{\dagger}\hat{\alpha}_1\right) + \frac{U}{2}\hat{\alpha}_L^{\dagger}\hat{\alpha}_L^{\dagger}\hat{\alpha}_L\hat{\alpha}_L -$$
$$-\eta_R\left(\hat{\alpha}_M^{\dagger}\hat{\alpha}_R + \hat{\alpha}_R^{\dagger}\hat{\alpha}_M\right) + \frac{U}{2}\hat{\alpha}_R^{\dagger}\hat{\alpha}_R^{\dagger}\hat{\alpha}_R\hat{\alpha}_R. \quad (5.2)$$

Now, let's write down the exact evolution equations for the population of the outer two wells:

$$\frac{d}{dt}\langle\hat{\alpha}_L^{\dagger}\hat{\alpha}_L\rangle = -2\eta_L\Im\langle\hat{\alpha}_L^{\dagger}\hat{\alpha}_1\rangle - \frac{\Gamma_L}{2}\langle\hat{\alpha}_L^{\dagger}\hat{\alpha}_L\rangle + \frac{\Gamma_L}{2}N_L \quad (5.3)$$

$$\frac{d}{dt}\langle\hat{\alpha}_R^{\dagger}\hat{\alpha}_R\rangle = -2\eta_R\Im\langle\hat{\alpha}_R^{\dagger}\hat{\alpha}_M\rangle - \frac{\Gamma_R}{2}\langle\hat{\alpha}_R^{\dagger}\hat{\alpha}_R\rangle + \frac{\Gamma_R}{2}N_R \quad (5.4)$$

if we assume $\eta_{L,R}\ll\Gamma_{L,R}$ we can approximate the above equations as follows

$$\frac{d}{dt}\langle\hat{\alpha}_L^{\dagger}\hat{\alpha}_L\rangle \approx -\frac{\Gamma_L}{2}\langle\hat{\alpha}_L^{\dagger}\hat{\alpha}_L\rangle + \frac{\Gamma_L}{2}N_L \quad (5.5)$$

$$\frac{d}{dt}\langle\hat{\alpha}_R^{\dagger}\hat{\alpha}_R\rangle \approx -\frac{\Gamma_R}{2}\langle\hat{\alpha}_R^{\dagger}\hat{\alpha}_R\rangle + \frac{\Gamma_R}{2}N_R. \quad (5.6)$$

The above equations have the following analytical solutions

$$\langle\hat{\alpha}_L^{\dagger}\hat{\alpha}_L\rangle_t \approx (\langle\hat{\alpha}_L^{\dagger}\hat{\alpha}_L\rangle_{t=0} - N_L)e^{-\frac{\Gamma_L}{2}t} + N_L$$
$$\langle\hat{\alpha}_R^{\dagger}\hat{\alpha}_R\rangle_t \approx (\langle\hat{\alpha}_R^{\dagger}\hat{\alpha}_R\rangle_{t=0} - N_R)e^{-\frac{\Gamma_R}{2}t} + N_R \quad (5.7)$$

now if we initially have $\langle\hat{\alpha}_L^{\dagger}\hat{\alpha}_L\rangle_{t=0} = N_L$ and $\langle\hat{\alpha}_R^{\dagger}\hat{\alpha}_R\rangle_{t=0} = N_R$ then in the whole evolution of our system the particle number will remain almost constant

$$\langle\hat{\alpha}_L^{\dagger}\hat{\alpha}_L\rangle_t \approx N_L, \ \langle\hat{\alpha}_R^{\dagger}\hat{\alpha}_R\rangle_t \approx N_R. \quad (5.8)$$

This very simple model allow us to control the population of the outer two wells in order to create a "voltage" between the two ends of the lattice.

Here we must note that this model is a simplified approximation of a Bose-Hubbard chain coupled to two bosonic thermal reservoirs, where the two outer wells serve as "contacts". In order to realize such a system experimentally we envisage the following procedure, which has essentially been realized already by the authors of [90]. One starts with a rather large trap with a Bose-Einstein condensate in perfect equilibrium in it. Then by an instantaneous potential shift one induces a sloshing of the condensate. After that the system should be cut into two subsystems, for instance by an

impenetrable barrier. In this way one produces two different bosonic reservoirs which contain a large number of particles in excited states. Gradually removing the barrier one can then couple these "reservoirs" and hence allow for the transport. The additional structuring of the contact area into several quantum dots can be accomplished in the way similar to that described in [90] for one well, or by adding a lattice potential along the channel created in [92].

5.2 A Double Well Coupled to Two Reservoirs

Now that we have set up our model, we would like to know how the transport properties are change if we vary the parameters of our model. Especially, what happens when interparticle interaction are present, since they bring nonlinearity to our problem. For our numerical calculations we use the truncated Wigner method, since, as we are going to see, when a steady state is reached the system loses its coherence. We are interested in transport, so it would be useful to introduce the following current operators

$$\hat{j}_L = i\eta_L(\hat{\alpha}_1^\dagger \hat{\alpha}_L - \hat{\alpha}_L^\dagger \hat{\alpha}_1), \;\; \hat{j}_R = i\eta_R(\hat{\alpha}_R^\dagger \hat{\alpha}_M - \hat{\alpha}_M^\dagger \hat{\alpha}_R). \tag{5.9}$$

Thus the current from the left reservoir to the chain and the current from the chain to the right reservoir are given by the expressions

$$j_L \equiv \langle \hat{j}_L \rangle = -2\eta_L \Im\langle \hat{\alpha}_1^\dagger \hat{\alpha}_L \rangle, \;\; j_R \equiv \langle \hat{j}_R \rangle = -2\eta_R \Im\langle \hat{\alpha}_R^\dagger \hat{\alpha}_M \rangle, \tag{5.10}$$

We have defined the currents in such a way that they will be both positive if the particles flow from the left reservoir to the right. For the current operators holds the following continuity equation

$$\hat{j}_L - \hat{j}_R = \partial_t \hat{n}_{tot} \equiv \partial_t(\hat{n}_1 + ... + \hat{n}_M). \tag{5.11}$$

As we discussed above, the dissipation mechanism we use allow us to control the particle number in the reservoirs. So let's see what happens if we change the "voltage", that is the particle difference of the reservoirs: $V = n_L - n_R \approx N_L - N_R$. Our system consists of four wells in which the outer two are the reservoirs. In figures 5.2 and 5.3 we have plotted the evolution of the system for small and large voltage, respectively, in the presence of interactions $U = 10^{-3}J$. In both cases after sort time a steady state is reached: the average currents $j_L^{\text{avg.}}$ and $j_R^{\text{avg.}}$ are equal, as it is depicted in

Figure 5.2: *The evolution of* (a) *the particle density in each lattice site,* (b) *the phase coherence (blue line) and the density-density correlations (red line),* (c) *the density fluctuations in the second site and* (d) *the currents. The parameters are* $U = 10^{-3}J$, $\eta_L = \eta_R = J$, $\Gamma_L = \Gamma_R = 10J$, $N_L = 700$ *and* $N_R = 100$. *Initially we had* $n_L(0) = 700$ *and* $n_1(0) = n_2(0) = n_R(0) = 100$.

figures 5.2 (d) and 5.3 (d). However, the resulting steady states have different characteristics. In the small voltage case at the steady state, the particle number in the first and second well are the same , as we can see in figure 5.2 (a). Moreover, the correlation functions have the behavior of a thermal state [20]: phase coherence $g_{1,2}^{(1)} \approx 0$, density-density correlations $g_{1,2}^{(2)} \approx 1$ (see figure 5.2 (b)) and density fluctuations $g_{1,1}^{(2)} \approx 2$ (see figure 5.2 (c)). From the other hand, in the large voltage case, we observe large particle imbalance between the two wells (see figure 5.3 (a)) density-density correlations smaller than one (see figure 5.3 (b)) and density fluctuations greater than two (see figure 5.3 (c)). As expected, also in this case the phase coherence tends to zero. The fact that the density-density correlations are smaller than one means that the particle densities in the two wells are correlated and we have anti-bunching: we will have many particles in the first well and fewer in the second one.

The above observations becomes more clear if we look at figure 5.4, where we have the mean particle number in the two wells and the currents, at the steady state, as a function of the voltage. In these examples we increase the particle number in the left reservoir, while we keep constant the particle
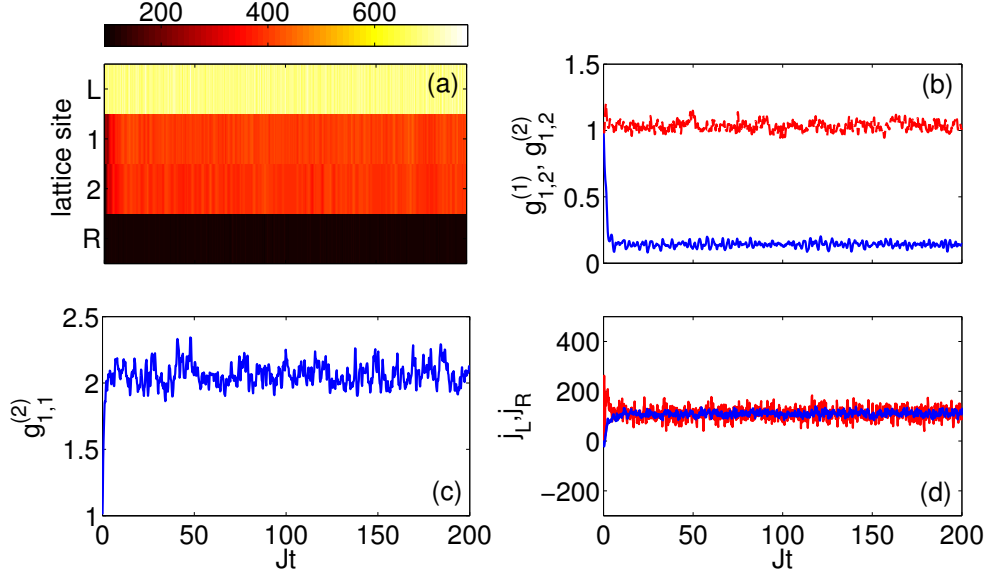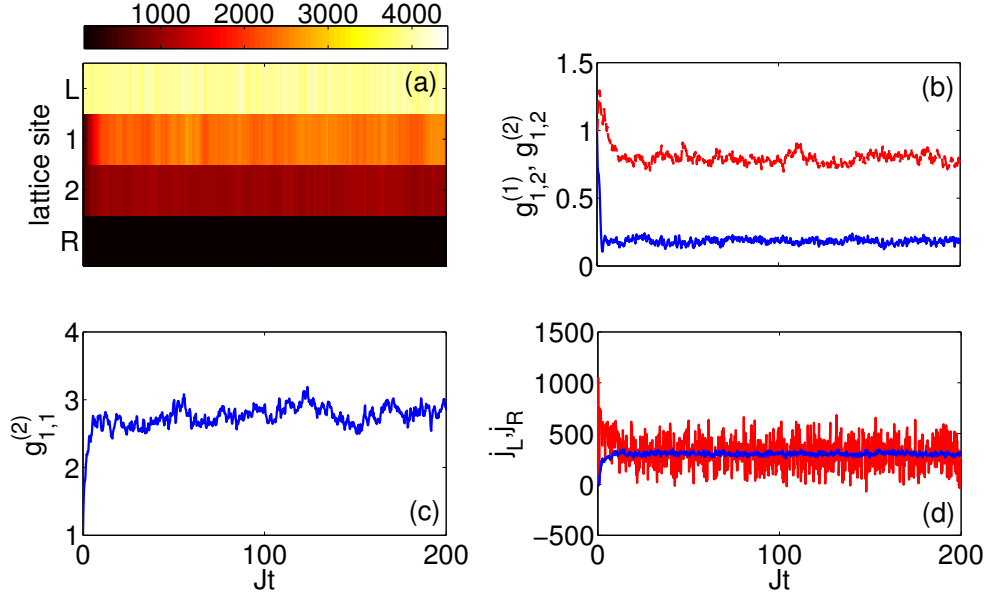
Figure 5.3: *The evolution of* (a) *the particle density in each lattice site,* (b) *the phase coherence (blue line) and the density-density correlations (red line),* (c) *the density fluctuations in the second site and (d) the currents. The parameters are* $U = 10^{-3}J$, $\eta_L = \eta_R = J$, $\Gamma_L = \Gamma_R = 10J$, $N_L = 4000$ *and* $N_R = 100$. *Initially we had* $n_L(0) = 4000$ *and* $n_1(0) = n_2(0) = n_R(0) = 100$.

number in the right one. In figure 5.4 (a) we have the particle number in the two wells as a function of voltage in the interacting case. In this figure we observe two regimes. in the first one, for $V \lesssim 1000$, the particle number in the two wells are the same and increase linearly with the voltage. In the second regime, for $V \gtrsim 1000$, the particle number in the first well (the well that is connected with the reservoir with the larger particle number) increases linearly with the voltage, while in the second well the particle number becomes almost constant. This is consequence of the self trapping effect: the change of behavior appears when the macroscopic interaction strength is greater than the tunneling strength, $Un_{\text{tot}}(0) > J$. On the contrary, in the non-interacting case, figure 5.4 (c), the particle number in the two wells are exactly the same and they increase linearly with the voltage.

Finally, let's discuss the behavior of the steady state current as a function of the voltage. In the non-interacting case, figure 5.4 (d), the current increase linearly with the voltage. However, for the interacting case, figure 5.4 (b), the current has a maximum after which the current drops. This means that for large voltages the transport of the particles through the lattice is blocked.

(a) $U = 10^{-3}J$

(b) $U = 10^{-3}J$

(c) $U = 0$

(d) $U = 0$
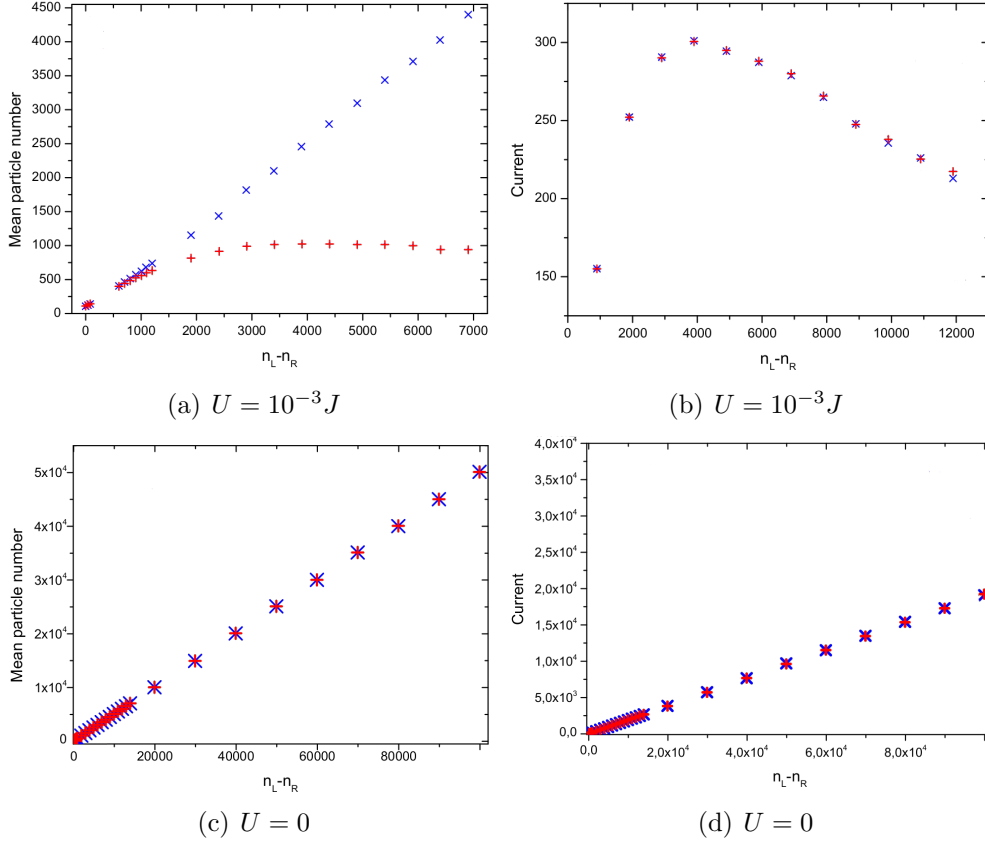
Figure 5.4: *The mean particle number in each lattice site (blue x for the first well, red crosses for the second) and the current (blue x for j_L and red crossesfor j_R) as a function of the voltage for non zero (a,b) and zero interactions (c,d). The parameters are $\eta_L = \eta_R = J$, $\Gamma_L = \Gamma_R = 10J$.*

The same qualitative behaviour we have observed in [78] by approximate the interaction contribution to the self-energy by the tabpole diagram, in the non-equilibrium Green's function framework. This behaviour is consequence of the interactions: as we saw in figure 5.4 (a) the particle number in the first lattice site increases with the voltage, which also means that the macroscopic interaction strength increases in that lattice site. Thus, we can conclude that the strong interactions that appear in the first lattice site block the transport of the particles.
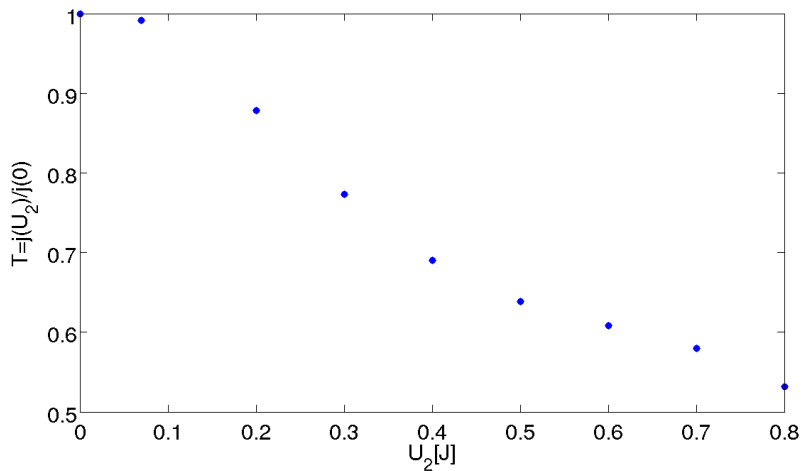
Figure 5.5: *The transmission coefficient through the middle site, in which interactions appear, as a function of the interactions in this site. The other parameters are $\eta_L = \eta_R = J$, $\Gamma_L = \Gamma_R = 50J$, and $E_L = E_1 = E_2 = E_3 = E_R = 0$. Initially we had $n_L(0) = 15$, $n_1(0) = n_2(0) = n_3(0) = 10$ and $n_R(0) = 5$.*

5.3 Transport Through a Single Interacting Site

The comment with which we finished the last section makes apparent the importance of the interparticle interactions in the transport of bosons through the lattice. In order to further investigate the observation we made in the last subsection we study the transport through a Bose-Hubbard chain but with interactions only in one lattice site. The system consists of five wells: the outer two are the reservoirs while the interactions are everywhere zero except the middle site where interactions occur.

In figure 5.5 we have the transmission coefficient, that is the steady state current through the middle interacting site divided by the current through the middle site when the interactions are zero, $U_2 = 0$, as a function of the interaction strength in the middle site. As one can see the transmission coefficient drops as the interactions are increased. This behavior confirms the observation we did in the last subsection. The interactions that appear in the middle site act as a barrier which blocks the transport of the atoms through the middle interacting site. The suppression of transport due to the interparticle interactions can also be understood by a simple argument. The

particles from the reservoir are forced to enter the interacting site but there they are trapped, since they cannot get rid of the energy by tunneling to the neighboring sites. As the particle number increases it becomes harder for particles out of the interacting site to tunnel, since this site is out of resonance. So finally a steady state is reached.

5.4 Transport Through a Single Non-Resonant Site

If our argument about the suppression of transport due to the interactions is correct, we could also achieve the same result if we bring out of resonance the energy level of the middle site, with zero interactions everywhere. Since there are no interactions in our system we can write down the exact evolution equations for the elements of the single particle density matrix. These equations can be obtained from the Master equation via $\frac{d}{dt}\langle\hat{\alpha}_\ell^\dagger\hat{\alpha}_m\rangle = tr\{\hat{\alpha}_\ell^\dagger\hat{\alpha}_m\dot{\hat{\rho}}\}$, with result

$$
\begin{aligned}
i\frac{d}{dt}\langle\hat{\alpha}_j^\dagger\hat{\alpha}_k\rangle = {} & -J\left(\langle\hat{\alpha}_j^\dagger\hat{\alpha}_{k+1}\rangle + \langle\hat{\alpha}_j^\dagger\hat{\alpha}_{k-1}\rangle - \langle\hat{\alpha}_{j+1}^\dagger\hat{\alpha}_k\rangle - \langle\hat{\alpha}_{j-1}^\dagger\hat{\alpha}_k\rangle\right) - \\
& -\eta_R\left(\langle\hat{\alpha}_j^\dagger\hat{\alpha}_R\rangle\delta_{kM} - \langle\hat{\alpha}_R^\dagger\hat{\alpha}_k\rangle\delta_{jM}\right) - \\
& -\eta_L\left(\langle\hat{\alpha}_j^\dagger\hat{\alpha}_L\rangle\delta_{k1} - \langle\hat{\alpha}_L^\dagger\hat{\alpha}_k\rangle\delta_{j1}\right) + (E_k - E_j)\langle\hat{\alpha}_j^\dagger\hat{\alpha}_k\rangle, \quad (5.12)
\end{aligned}
$$

also we have

$$
\begin{aligned}
i\frac{d}{dt}\langle\hat{\alpha}_j^\dagger\hat{\alpha}_L\rangle = {} & -J\left(\langle\hat{\alpha}_{j-1}^\dagger\hat{\alpha}_L\rangle - \langle\hat{\alpha}_{j+1}^\dagger\hat{\alpha}_L\rangle\right) + (E_L - E_j)\langle\hat{\alpha}_j^\dagger\hat{\alpha}_L\rangle - \\
& -\eta_L(\langle\hat{\alpha}_j^\dagger\hat{\alpha}_1\rangle - \langle\hat{\alpha}_L^\dagger\hat{\alpha}_L\rangle\delta_{j1}) + \eta_R\langle\hat{\alpha}_R^\dagger\hat{\alpha}_L\rangle\delta_{jM} - \\
& -i\frac{\Gamma_L}{2}\langle\hat{\alpha}_j^\dagger\hat{\alpha}_L\rangle, \quad (5.13)
\end{aligned}
$$

$$
\begin{aligned}
i\frac{d}{dt}\langle\hat{\alpha}_j^\dagger\hat{\alpha}_R\rangle = {} & -J\left(\langle\hat{\alpha}_{j-1}^\dagger\hat{\alpha}_R\rangle - \langle\hat{\alpha}_{j+1}^\dagger\hat{\alpha}_R\rangle\right) + (E_R - E_j)\langle\hat{\alpha}_j^\dagger\hat{\alpha}_R\rangle - \\
& -\eta_R(\langle\hat{\alpha}_j^\dagger\hat{\alpha}_M\rangle - \langle\hat{\alpha}_R^\dagger\hat{\alpha}_R\rangle\delta_{Mj}) + \eta_L\langle\hat{\alpha}_L^\dagger\hat{\alpha}_R\rangle\delta_{1j} - \\
& -i\frac{\Gamma_R}{2}\langle\hat{\alpha}_j^\dagger\hat{\alpha}_R\rangle, \quad (5.14)
\end{aligned}
$$

$$
\begin{aligned}
i\frac{d}{dt}\langle\hat{\alpha}_R^\dagger\hat{\alpha}_L\rangle = {} & \eta_R\langle\hat{\alpha}_M^\dagger\hat{\alpha}_L\rangle - \eta_L\langle\hat{\alpha}_R^\dagger\hat{\alpha}_1\rangle + (E_L - E_R)\langle\hat{\alpha}_R^\dagger\hat{\alpha}_L\rangle - \\
& -i\frac{\Gamma_R + \Gamma_L}{2}\langle\hat{\alpha}_R^\dagger\hat{\alpha}_L\rangle, \quad (5.15)
\end{aligned}
$$
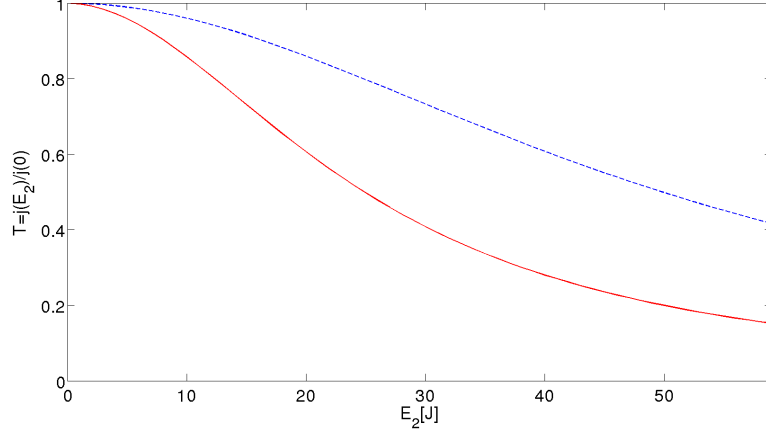
Figure 5.6: The transmission coefficient through the non-resonant middle site as a function of the energy of this site. Red line: $\Gamma_L = \Gamma_R = 50J$. Blue dashed line: $\Gamma_L = \Gamma_R = 100J$. The other parameters are $U = 0$, $\eta_L = \eta_R = J$, and $E_L = E_1 = E_3 = E_R = 0$. Initially we had $n_L(0) = 30$, $n_1(0) = n_2(0) = n_3(0) = 10$ and $n_R(0) = 10$.

$$i\frac{d}{dt}\langle\hat{\alpha}_R^\dagger\hat{\alpha}_R\rangle = -\eta_R\left(\langle\hat{\alpha}_R^\dagger\hat{\alpha}_M\rangle - \langle\hat{\alpha}_M^\dagger\hat{\alpha}_R\rangle\right) - i\frac{\Gamma_R}{2}\langle\hat{\alpha}_R^\dagger\hat{\alpha}_R\rangle + i\frac{\Gamma_R}{2}N_R, \quad (5.16)$$

$$i\frac{d}{dt}\langle\hat{\alpha}_L^\dagger\hat{\alpha}_L\rangle = -\eta_L\left(\langle\hat{\alpha}_L^\dagger\hat{\alpha}_1\rangle - \langle\hat{\alpha}_1^\dagger\hat{\alpha}_L\rangle\right) - i\frac{\Gamma_L}{2}\langle\hat{\alpha}_L^\dagger\hat{\alpha}_L\rangle + i\frac{\Gamma_L}{2}N_L, \quad (5.17)$$

where $k, j = 1, ..., M$ with $M = 3$.

In figure 5.6 we have plotted the transmission coefficient T, that is the steady state current through the middle non-resonant site divided by the current through the middle site of a flat lattice ($E_2 = 0$), as a function of the energy of the non-resonant site. As one can see the transmission coefficient decreases as the energy difference between the middle site and the neighboring sites increases. This behavior confirms our argument we gave in the previous section. Large energy difference between neighboring sites blocks the transport of the bosons. We also note that if we increase $\Gamma_{L,R}$ then the decrease of T becomes slower. So we can control the transport also by controlling parameters of the reservoirs, like $\Gamma_{L,R}$.

5.5 Conclusions

The present chapter was devoted to the non-equilibrium transport through a Bose-Hubbard chain. We have used a simple model which uses the Master equation formalism and allows to study the non-equilibrium dynamics. The presence of interparticle interactions plays an important role to the transport properties of the system. In the weak interacting case one observes that the system reach a thermal-like steady state, while in the strong interacting case we have the formation of bunches of atoms due to the self-trapping effect. In both cases the coherence of the system in the steady state is lost, that is why one should be careful of what approximations uses. Here we have mainly used the truncated Wigner method which allows the deviation from the pure BEC state and we have used the correlation functions equations only in section 5.4 where the interactions are absent from the system. We further investigated the role of interactions and saw that the transport of bosons through a single interacting site is suppressed. The same holds for the transport through a single non-resonant site. In both cases the bosons are repelled by the high energy barrier of the single site.

Chapter 6

Path Integrals in the BEC Theory

In this chapter we study bosonic systems by using the path integral formalism. The chapter is divided into two independent sections. In section 6.1 we discuss the emergence of the Bose-Einstein condensation from the point of view of the quantum information theory. We analyse the statistical and the genuine quantum correlations as the bosonic system changes from the ideal gas state to the BEC state using as tools the geometric entropy and the mutual information. In section 6.2 we develop a general formalism which allows the use of coherent state path integrals directly in the continuum. The formalism is applied to the case of the M-site Bose-Hubbard model.

6.1 The Bose-Einstein Condensation in Quantum Informational Terms

In subsection 1.1.1 we have presented a standard textbook derivation of the Bose-Einstein condensation phenomenon. One could study the same phenomenon in the quantum field theory framework, by using the functional integral formalism [137]. In this section we use this formalism to probe the implications of the BEC on the spatial correlations of an ideal quantum system. The tool we shall use for this task is the so-called geometric entropy [105].

The notion of the geometric entropy, in the framework of a quantum system, is quite old. One of the first calculations [108] was performed in the eighties for the case of a scalar field propagating in a black hole background. Some years later, a similar problem, in the framework of a quantum

91

field theory, was addressed by several authors [109–119]. Geometric entropy, generally speaking, is a measure of the information loss after cutting out a spatial region of the system. It caught attention because of its characteristic behavior: for a system in its ground state, it grows like the boundary surface of the excluded subregion, a property it shares with the black hole entropy. In fact, in the context of quantum field theory, pioneering work on the geometric entropy was driven in part by the suggested connection to the Bekenstein–Hawking black hole entropy [120, 121]. From the very beginning, geometric entropy has been tightly related with the presence of spatial entanglement in a quantum system. Entanglement is a fundamental ingredient of quantum mechanics leading to strong correlations between subsystems. From the early days of quantum mechanics up until now, it has been playing an increasingly important role in understanding and controlling quantum systems. The interest in it has been renewed [122–126] after the developments of the quantum information science in which it is viewed as a resource in quantum information processing. Geometric entropy has been considered as a measure of spatial entanglement when the system under consideration is in a pure quantum state.

When the system is in a thermal state, e.g. in a mixed state, the geometric entropy can be defined, following the von Neumann definition, in an analogous way. However, in this case, it does not have the same properties as the entanglement entropy in a pure state system, and it is no longer a good estimator of entanglement since it mixes correlations of different types [111–119, 127–129], from genuine quantum to thermal correlations. Since it measures the thermal information loss, geometric entropy becomes an extensive quantity at the limit of an infinite system, and loses the "area law" behavior that characterizes a pure state system. As an alternative probe for the amount of correlations between different parts of a system in the case of thermal states,the notion of the so-called "mutual information" [127, 130–133] has been proposed, which, roughly speaking, eliminates the contribution of the extensive part of the thermal entropy from the geometric entropy and can be considered as an upper limit for the entanglement entropy.

In any case, geometric entropy has been considered as a convenient construction, playing the role of an order parameter, for the investigation of finite temperature conformal quantum field systems [116–119] and in the context of the AdS/CFT correspondence, aiming at the physics of strongly coupled Quark-Gluon Plasma, the weakly coupled deconfined phase of Yang-Mills theories or the phase structure of large N QCD at a finite density [134, 135].

In the current work, we examine the geometric entropy in a free bosonic quantum field theory at finite temperature and at zero and non-zero chemical potential. Having found it, we subtract its extensive part, that is, the part

related to the amount of information that is lost due to the mixed nature of the system. The result, defined as the mutual information, quantifies the spatial correlations between the different parts of the system and exhibits the known area law behavior.

The underlying reason for the present study is connected to the Bose-Einstein condensation that characterizes the system, which has been in the center of theoretical and experimental investigations during the last fifteen years after the production of the condensate in the laboratory [8, 9]. Bose-Einstein condensation has the characteristics of a phase transition albeit, theoretically at least, it can take place in an ideal system [17–19, 136–139]. It is then natural to search for the interconnection between this phase transition and the spatial correlations in the Bose system. Our findings indicate that, indeed, the Bose-Einstein condensation influences the behavior of the mutual information: We find that its derivative with respect to the temperature, $\partial I_m/\partial \mathrm{T}$, has a finite discontinuity at the critical temperature both at the non-relativistic and the relativistic limit. Thus, we show how this phase transition leaves its fingerprint on a quantum informational quantity like mutual information.

This section is structured as follows: First, in subsection 6.1.1, we define the geometric entropy at zero temperature and we discuss the area law behavior. In subsection 6.1.2, we introduce the transition amplitude for second quantized bosonic fields. Then in subsection 6.1.3 we define the thermal density matrix the partition function for a scalar bosonic field. In subsection 6.1.4 we present the calculation of the geometric entropy at finite temperature and zero chemical potential and we retrieve the resulting mutual information, setting the stage for our result goal which is the topic of the section that follows. This is subsection 6.1.5, in which we apply our results in an environment with a finite charge density, we calculate the explicit form of the mutual information, and we derive the discontinuity of its temperature derivative. Finally, in the last subsection we summarize our findings. In Appendix D we present some technical details of our calculations.

6.1.1 Geometric Entropy and the Area Law

The goal of this subsection is to define the so-called geometric entropy at zero temperature and discuss its properties. We assume that we have a large system at zero temperature in its ground state, with density matrix of the form $\hat{\rho} = |\mathrm{Gr.}\rangle\langle\mathrm{Gr.}|$, and that there is a non-zero energy gap above it. By defining an "in" spatial region A and an "out" spatial region B (see figure 6.1) and tracing out the "out" degrees of freedom one obtains the reduced
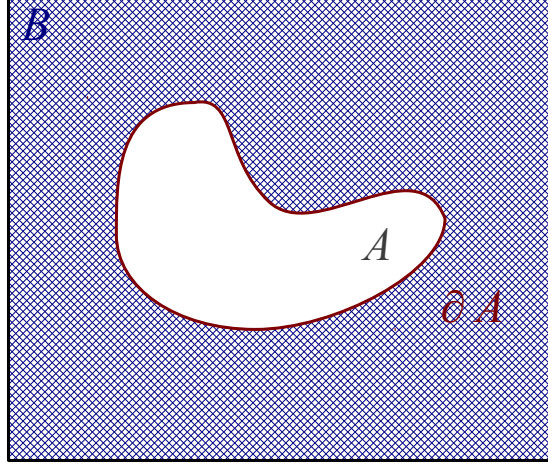
Figure 6.1: *Schematic of a quantum system prepared in its ground state and partitioned into two spatial regions A and B, via the boundary ∂A.*

density matrix for the "in" region: $\hat{\rho}_A = \text{tr}_{\text{B}}\hat{\rho}$. The geometric entropy is then defined as the von Neumann entropy: $S_A = -\text{tr}\hat{\rho}_A \ln \hat{\rho}_A$. Since there is an energy gap we expect a finite correlation length ξ

$$\langle \hat{O}(\vec{x}_1)\hat{O}(\vec{x}_1)\rangle - \langle \hat{O}(\vec{x}_1)\rangle\langle \hat{O}(\vec{x}_2)\rangle \overset{|\vec{x}_1-\vec{x}_2|\to\infty}{\sim} \exp\left\{-\frac{|\vec{x}_1-\vec{x}_2|}{\xi}\right\}, \qquad (6.1)$$

where the operator $\hat{O}(\vec{x}_j)$ is defined in the neighborhood of the point $\vec{x}_j$ and the expectation values are with respect to the ground state $|\text{Gr.}\rangle$. So the correlations drop exponentially with the relative distance. This last observation will help us to understand an important characteristic of the geometric entropy, the area law.

We will argue that we can write the geometric entropy in the form [107]

$$S_A = \alpha|\partial A| + \varepsilon(|\partial A|^{-\beta}), \qquad (6.2)$$

where α, γ are real and $\beta > 0$. In the following we will deal with an infinite system, so the last term in (6.2) tends to zero, since the boundary, $|\partial A|$, tends to infinity. A first observation is that in the entropy (6.2) there is no volume term, $|A|$. This is expected since our system is in a pure state $|\text{Gr.}\rangle$. Indeed, a volume term would appear only if every particle in the system was entangled with an environment, so it would contribute to the entropy.

Now we will try to justify the area term $|\partial A|$. This term is a consequence

of the finite correlation length, ξ, due to the energy gap[1]. The entropy S_A measures how much the region A is entangled with the region B. Since, ξ is finite we cannot expect a particle deep in region A to be entangled with a particle deep in region B. So the only contribution to the entropy comes from a strip at each side of the boundary, ∂A, of width ξ. The coefficient α in (6.2) is a non-universal quantity that depends in general on the small-scale properties of the ground state, such as the correlation length ξ. This characteristic area dependence of the entropy is known as *area law*.

Finally, it is worth to note that in the special case of a two dimensional system there will be in (6.2) an additional term $-\gamma$. This term is of great importance for topological systems, which is beyond the scope of this section. We will only say that it characterizes global features of the ground state and that the presence of this term shows an additional order in our system which do not depend on the boundary (for more details see [107]).

6.1.2 Second Quantized Bosonic Fields and the Transition Amplitude

The first ingredient we will need is the transition amplitude, from one state to another, for a bosonic field theory. Let's remember the correspondences between quantum mechanics and quantum field theory. The position operator $\hat{\vec{x}}$, correspond to the field operator $\hat{\varphi}(\vec{x})$, while the position eigenstate $|\vec{x}\,\rangle$, to the field state $|\varphi\rangle$

$$\hat{\vec{x}}\,|\vec{x}\,\rangle = \vec{x}\,|\vec{x}\,\rangle \rightarrow \hat{\varphi}(\vec{x})\,|\varphi\rangle = \varphi(\vec{x})\,|\varphi\rangle, \tag{6.3}$$

where $\vec{x}$ is the eigenvalue of the position operator and $\varphi(\vec{x})$ is the eigenvalue of the field operator which is function of $\vec{x}$. The eigenstates of the field operator form a complete and orthogonal basis in the Fock space

$$\hat{I} = \int \mathcal{D}\varphi(\vec{x})|\varphi\rangle\langle\varphi|, \tag{6.4}$$

$$\langle\varphi_a|\varphi_b\rangle = \prod_{\vec{x}} \delta(\varphi_a(\vec{x}) - \varphi_b(\vec{x})) \equiv \delta[\varphi_a - \varphi_b]. \tag{6.5}$$

Now, we must write the commutation relation that involves the field ϕ, so we need the momentum conjugate to ϕ. To this end, we need the action, $S[\varphi]$, which is functional of the field

$$S[\phi] = \int_{t_i}^{t_f} dt \int d^3x \mathcal{L}[\varphi], \tag{6.6}$$

---

[1]This term also appears in conformal field theories which have not energy gap. However, this is beyond the scope of this section.

where $\mathcal{L}$ is the Lagrangian density. By using the action principle it is easy to obtain the equations of motion

$$\partial_\mu \left(\frac{\partial \mathcal{L}}{\partial(\partial_\mu \varphi)} \right) - \frac{\partial \mathcal{L}}{\partial \varphi} = 0 \tag{6.7}$$

where $\partial_\mu = \partial/\partial x^\mu$, with $x^0 = t$. The field momentum conjugate to φ is

$$\pi(t, \vec{x}) = \frac{\partial \mathcal{L}}{\partial(\partial_0 \varphi(t, \vec{x}))} \tag{6.8}$$

and the field Hamiltonian is the Legendre transform of the Lagrangian

$$H = \int d^3x \left(\pi(t, \vec{x}) \, \partial_0 \varphi(t, \vec{x}) - \mathcal{L} \right). \tag{6.9}$$

Now we quantize the fields and the corresponding operators satisfy the equal-time commutation relations

$$[\hat{\varphi}(t, \vec{x}), \hat{\pi}(t, \vec{x}\,')] = i\delta^3(\vec{x} - \vec{x}\,'). \tag{6.10}$$

and we write the second quantized Hamiltonian

$$\hat{H} = \int d^3x \, \mathcal{H}(\hat{\varphi}, \hat{\pi}). \tag{6.11}$$

Similarly, with the field operator, we have for the conjugate momentum field operator

$$\hat{\pi}(\vec{x})|\pi\rangle = \pi(\vec{x})|\pi\rangle, \tag{6.12}$$

with completeness and orthogonality relations

$$\hat{I} = \int \frac{\mathcal{D}\pi(\vec{x})}{2\pi} |\pi\rangle\langle\pi|, \tag{6.13}$$

$$\langle \pi_a | \pi_b \rangle = \delta[\pi_a - \pi_b]. \tag{6.14}$$

Finally, the overlap of the field eigenstate with the conjugate momentum eigenstate gives

$$\langle \varphi | \pi \rangle = \exp \left\{ i \int d^3x \, \pi(\vec{x})\varphi(\vec{x}) \right\}. \tag{6.15}$$

In the next subsection we will derive the partition function for a bosonic field. For this we need the transition amplitude, for going from a state $|\phi_i\rangle$ at $t = t_i$ to the state $|\phi_f\rangle$ at $t = t_f$, $\langle \phi_f | \mathrm{e}^{-iH(t_f - t_i)} | \phi_i \rangle$. To derive a useful expression for this transition amplitude we divide the time interval (t_i, t_f)

into N equal steps of magnitude $\Delta t = (t_f - t_i)/(N+1)$ and we insert the completeness relations (6.4) and (6.13) as follows

$$\langle\phi_f|e^{-i\hat{H}(t_f-t_i)}|\phi_i\rangle \;\; = \;\; \lim_{N\to\infty}\int\prod_{j=0}^{N+1}d\phi_j\int\prod_{j=1}^{N}\frac{d\pi_j}{2\pi}\delta(\phi_{N+1}-\phi_j)\delta(\phi_0-\phi_i)$$

$$\times\prod_{j=1}^{N}\langle\phi_j|e^{-i\hat{H}\Delta t}|\pi_j\rangle\prod_{j=1}^{N}\langle\pi_j|\phi_{j-1}\rangle. \tag{6.16}$$

Since $\Delta t \to 0$, we expand the exponentials in (6.16) and keep terms to first order

$$\langle\phi_j|e^{-i\hat{H}_j\Delta t}|\pi_j\rangle \;\; \approx \;\; \langle\phi_j|(1-i\hat{H}_j\Delta t)|\pi_j\rangle$$
$$= \;\; (1-iH_j\Delta t)\langle\phi_j|\pi_j\rangle, \tag{6.17}$$

where

$$H_j = \int d^3x\,\mathcal{H}(\pi_j(\vec{x}),\phi_j(\vec{x})). \tag{6.18}$$

Using the relation (6.15) it is easy to write

$$\langle\phi_f|e^{-i\hat{H}(t_f-t_i)}|\phi_i\rangle \;\; = \;\; \lim_{N\to\infty}\int\prod_{j=0}^{N+1}d\phi_j\int\prod_{j=1}^{N}\frac{d\pi_j}{2\pi}\delta(\phi_{N+1}-\delta_f)\delta(\phi_0-\phi_i) \tag{6.19}$$

$$\times\exp\left\{-i\Delta t\sum_{j=1}^{N}\int d^3x[\mathcal{H}(\pi_j,\phi_j)-\pi_j(\phi_j-\phi_{j-1})/\Delta t]\right\}.$$

Now we take the continuum limit of (6.19) and we obtain the following result for the transition amplitude

$$\langle\phi_f|e^{-i\hat{H}(t_f-t_i)}|\phi_i\rangle \;\; = \;\; \int\mathcal{D}\pi\int_{\substack{\phi(t_f,\vec{x})=\phi_f(\vec{x})\\\phi(t_i,\vec{x})=\phi_i(\vec{x})}}\mathcal{D}\phi\;\;\exp\left\{i\int_{t_i}^{t_f}dt\int d^3x\right.$$

$$\left.\times\left(\pi(t,\vec{x})\frac{\partial\phi(t,\vec{x})}{\partial t}-\mathcal{H}(\pi(t,\vec{x}),\phi(t,\vec{x}))\right)\right\} \tag{6.20}$$

where $\mathcal{D}\pi$ and $\mathcal{D}\phi$ denote functional integration, with the π integration unrestricted and ϕ integration is such that the fields starts at $\phi_i(\vec{x})$ and ends at $\phi_f(\vec{x})$. Here we must note that in expression (6.20) there are no operators but only functions.

6.1.3   Thermal Density Matrix and Partition Function for Bosonic Fields

The thermal density matrix for the canonical ensemble has the well-known form

$$\hat{\rho} = \frac{\mathrm{e}^{-\beta \hat{H}}}{Z}, \tag{6.21}$$

where Z is the partition function, $\hat{H}$ the Hamiltonian and $\beta = 1/kT$, with T the temperature of the system. For a quantum field system, the Fock state representation of (6.21) is

$$\rho[\phi_f, \phi_i] = \frac{1}{Z} \langle \phi_f | \mathrm{e}^{-\beta \hat{H}} | \phi_i \rangle, \tag{6.22}$$

where ϕ denotes a single scalar field or even a collection of fields. The numerator in the right hand side of (6.22) looks like the transition amplitude (6.20) with the only difference that the time is imaginary $\tau = it$. In other words we can interpret $\langle \phi_f | \mathrm{e}^{-\beta \hat{H}} | \phi_i \rangle$ as the transition amplitude to go from the field $|\phi_i\rangle$ at $\tau_i = 0$ to the field $|\phi_f\rangle$ at $\tau_f = \beta$. Thus we can write

$$
\begin{aligned}
\langle \phi_f | \mathrm{e}^{-\beta \hat{H}} | \phi_i \rangle &= \int \mathcal{D}\pi \underset{\substack{\phi(\beta,\vec{x})=\phi_f(\vec{x}) \\ \phi(0,\vec{x})=\phi_i(\vec{x})}}{\int \mathcal{D}\phi} \quad \exp \left\{ \int_0^\beta d\tau \int d^3 x \right. \\
&\left. \times \left(i\pi(\tau,\vec{x}) \frac{\partial \phi(\tau,\vec{x})}{\partial \tau} - \mathcal{H}(\pi(\tau,\vec{x}), \phi(\tau,\vec{x})) \right) \right\}.
\end{aligned} \tag{6.23}
$$

In a similar way we can write the partition function Z if we remember that

$$Z(\beta) = \mathrm{Tr}\ \mathrm{e}^{-\beta \hat{H}} = \sum_a \int d\phi_a \langle \phi_a | \mathrm{e}^{-\beta \hat{H}} | \phi_a \rangle, \tag{6.24}$$

where the sum is over all states. In the right hand side we have the transition amplitude to go from a state $|\phi_a\rangle$ at $\tau_i = 0$ to the same state $|\phi_a\rangle$ at $\tau_f = \beta$, thus we can write

$$
\begin{aligned}
Z(\beta) &= \int \mathcal{D}\pi \underset{\mathrm{periodic}}{\int \mathcal{D}\phi} \exp \left\{ \int_0^\beta d\tau \int d^3 x \right. \\
&\left. \times \left(i\pi(\tau,\vec{x}) \frac{\partial \phi(\tau,\vec{x})}{\partial \tau} - \mathcal{H}(\pi(\tau,\vec{x}), \phi(\tau,\vec{x})) \right) \right\},
\end{aligned} \tag{6.25}
$$

where the term *periodic* means that the integration over the field is constrained in such a way that $\phi(0,\vec{x}) = \phi(\beta,\vec{x})$, which is consequence of the trace operation.

Finally, we can write the thermal density matrix in the form

$$
\rho[\phi_f, \phi_i] \;=\; \frac{1}{Z(\beta)} \int \mathcal{D}\pi \int_{\substack{\phi(\beta,\vec{x})=\phi_f(\vec{x}) \\ \phi(0,\vec{x})=\phi_i(\vec{x})}} \mathcal{D}\phi \; \exp\left\{ \int_0^\beta d\tau \int d^3x \right.
$$
$$
\left. \times \left(i\pi(\tau,\vec{x})\frac{\partial\phi(\tau,\vec{x})}{\partial\tau} - \mathcal{H}(\pi(\tau,\vec{x}),\phi(\tau,\vec{x})) \right) \right\}, \quad (6.26)
$$

where $Z(\beta)$ is the partition function (6.25). The above expression for the density matrix (6.26) and the partition function (6.25) can readily be generalized to an arbitary number of fields. If our system admits a conserved charge the we must make the replacement

$$
\mathcal{H}(\pi,\phi) \to \mathcal{H}(\pi,\phi) - \mu\mathcal{N}(\pi,\phi) \tag{6.27}
$$

where $\mathcal{N}(\pi,\phi)$ is the conserved charge density.

Before proceeding we will see a simple example, the neutral scalar field. In this case the most general renormalizable Lagrangian is

$$
\mathcal{L} = \frac{1}{2}\partial_\mu\phi\,\partial^\mu\phi - \frac{1}{2}m^2\phi^2 - V(\phi), \tag{6.28}
$$

where m is the mass of the field and

$$
V(\phi) = \lambda\phi^4, \tag{6.29}
$$

is the potential with $\lambda \geq 0$ for the stability of the vacuum.

The momentum conjugate to field ϕ is

$$
\pi = \frac{\partial\mathcal{L}}{\partial(\partial_0\phi)} = \frac{\partial\phi}{\partial t} \tag{6.30}
$$

and the Hamiltonian is obtained through the Legendre transformation

$$
\mathcal{H} = \pi\frac{\partial\phi}{\partial t} - \mathcal{L} = \frac{1}{2}\pi^2 + \frac{1}{2}(\nabla\phi)^2 + \frac{1}{2}m^2\phi^2 + V(\phi). \tag{6.31}
$$

In this example there is no conserved charge. To proceed we write the density matrix (6.26) in a discretized form

$$
\rho[\phi_f, \phi_i]\, Z(\beta) \;=\; \lim_{N\to\infty} \prod_{k=0}^{N+1} \int d\phi_k \prod_{k=1}^{N} \int_{-\infty}^{\infty} \frac{d\pi_k}{2\pi}
$$
$$
\times \exp\left\{ \sum_{j=1}^{N} \int d^3x\, (i\pi_j(\phi_j - \phi_{j-1}) \right.
$$
$$
\left. - \frac{\Delta\tau}{2}\,[\pi_j^2 + (\nabla\phi_j)^2 + m^2\phi_j^2 + 2V(\phi)]) \right\} \tag{6.32}
$$

where $\phi_1 = \phi_i$ and $\phi_{N+1} = \phi_f$. In this form it is easy to perform the momentum integrals since they are a product of Gaussian integrals. We divide the position space into M^3 small cubes with volume $v = (aM)^3$ where $a \to 0$ and $M \to \infty$, M being an integer. For convenience we use the variable $\Pi_j = (a^3 \Delta \tau)^{-1/2}$, so we have

$$\int_{-\infty}^{\infty} \frac{d\Pi_j}{2\pi} \exp\left\{-\frac{1}{2}\Pi_j^2 + i\left(\frac{a^3}{\Delta\tau}\right)(\phi_j - \phi_{j-1})\Pi_j\right\}$$
$$= \frac{1}{\sqrt{2\pi}} \exp\left\{-\frac{a^3(\phi_j - \phi_{j-1})^2}{2\Delta\tau}\right\} \tag{6.33}$$

for each cube. So we have

$$\begin{aligned}\rho[\phi_f, \phi_i] \, Z(\beta) &= \lim_{M,N\to\infty} (2\pi)^{-M^3 N/2} \int \left(\prod_{k=1}^{N} d\phi_k\right) \\ &\times \exp\left\{\Delta\tau \sum_{j=1}^{N} \int d^3x \left[-\frac{1}{2}\left(\frac{\phi_j - \phi_{j-1}}{\Delta\tau}\right)^2\right.\right. \\ &\left.\left. -\frac{1}{2}(\nabla\phi_j)^2 - \frac{1}{2}m^2\phi_j^2 - V(\phi_j)\right]\right\}.\end{aligned} \tag{6.34}$$

Taking the continuum limit, we have

$$\rho[\phi_f, \phi_i] = \frac{1}{Z(\beta)} \int_{\substack{\phi(\beta,\vec{x})=\phi_f(\vec{x}) \\ \phi(0,\vec{x})=\phi_i(\vec{x})}} \mathcal{D}\phi(\tau, \vec{x}) \, e^{-\int_0^\beta d\tau \int d^3x \mathcal{L}_{\mathrm{E}}[\phi]}, \tag{6.35}$$

where the partition function, by following a similar process, can also be written in the form

$$Z(\beta) = \int_{\text{periodic}} \mathcal{D}\phi(\tau, \vec{x}) e^{-\int_0^\beta d\tau \int d^3x \mathcal{L}_{\mathrm{E}}[\phi]}. \tag{6.36}$$

The formulas (6.35) and (6.36) expresses the thermal density matrix and the partition function as a functional integral over ϕ of the exponential of the action in imaginary time

$$\mathcal{L}_{\mathrm{E}} = (\partial_\tau \phi)^2 + (\nabla\phi)^2 + m^2\phi^2 + V(\phi). \tag{6.37}$$

6.1.4   Geometric Entropy at Finite Temperature

Our starting point is the thermal density matrix (6.35) in D spatial dimensions

$$\rho[\phi_f, \phi_i] = \frac{1}{Z(\beta)} \int\limits_{\substack{\phi(\beta, \vec{x})=\phi_f(\vec{x}) \\ \phi(0, \vec{x})=\phi_i(\vec{x})}} \mathcal{D}\phi(\tau, \vec{x}) \, e^{-\int\limits_0^\beta d\tau \int d^D x \mathcal{L}_E[\phi]} \tag{6.38}$$

here the action is the free Euclidean Klein-Gordon Lagrangian

$$\mathcal{L}_E = \frac{1}{2}\partial_\mu \phi \, \partial_\mu \phi + \frac{1}{2}m^2 \phi^2. \tag{6.39}$$

It is worth noting that at the zero temperature limit, $\beta \to \infty$, (6.38) is just an expression for the ground state density matrix [111–115]. It is then natural to expect that our result will reproduce, at this limit, the known [110–119] entanglement entropy.

Our goal is to derive the geomtric entropy we introduced in subsection 6.1.1. The calculation of the entropy can be performed with the help of the so-called replica method [111–113]. To apply it, one introduces the quantity

$$\begin{aligned}
\text{Tr}(\hat{\rho}_R)^n &= \int \left(\prod_{j=1}^n \mathcal{D}\phi_j \right) \rho_R[\phi_1, \phi_2]\rho_R[\phi_2, \phi_3] \dots \rho_R[\phi_{n-1}, \phi_n]\rho_R[\phi_n, \phi_1] \\
&\equiv f(n), \tag{6.40}
\end{aligned}$$

where $\hat{\rho}_R$ is the reduced density matrix after we have spatially divided our system in an "in" region and an "out" region which we have traced out (see subsection 6.1.1). After calculating the function $f(n)$ for integer n, we consider the function

$$f(n) = \text{Tr}(\hat{\rho}_R)^\nu, \; \nu > 0. \tag{6.41}$$

Using analytic continuation we can find the entanglement entropy from the relation

$$S_g = -\lim_{\nu \to 1} \frac{\text{Tr}(\hat{\rho}_R)^\nu - 1}{\nu - 1} = -\text{Tr}(\hat{\rho}_R \ln \hat{\rho}_R). \tag{6.42}$$

For the case at hand we divide the D dimensional space on which our system is defined, into two regions $A: \; (x_1 > 0, \vec{x}_\perp)$ and $B: \; (x_1 < 0, \vec{x}_\perp)$. Tracing out the "in" region, and gluing along the axis $x_1 > 0$, n copies of the resulting reduced density matrix, we find [110–119]:

$$\text{Tr}(\hat{\rho}_R)^n = \frac{1}{Z^n(\beta)} \int\limits_{M_n} \mathcal{D}\phi \, e^{-S[\phi]} \equiv \frac{Z_n(\beta)}{Z^n(\beta)}. \tag{6.43}$$

In Z_n the fields are defined on a $D+1$ dimensional space $M_n = R_{D-1} \times C_n$. The subspace R_{D-1} is an Euclidean space with metric $ds^2 = dx_2^2 + \cdots + dx_D^2$ while C_n is a two dimensional Riemann space consisting of n sheets glued together along the positive x_1 axis. This n folded structure turns eventually [111–115] the (τ, x_1) plane into a flat cone with an angle deficit $\delta = 2\pi(1-n)$ at the origin. Having found $\mathrm{Tr}(\hat{\rho}_R)^n$ we can obtain the geometric entropy by using equation (6.42):

$$S_g = -\left(\frac{\partial}{\partial n} - 1\right) \ln Z_n \bigg|_{n=1}.$$

For a free bosonic theory, the partition function can be deduced by following standard steps [111–115]:

$$
\begin{aligned}
\ln Z_n(\beta) &= \ln\left[\det_{M_n}(-\partial_E^2 + m^2)\right]^{-\frac{1}{2}} = -\frac{1}{2}\mathrm{Tr}_{M_n}\left[\ln(-\partial_E^2 + m^2)\right] \\
&= \frac{1}{2}\int_{0^+}^{\infty} \frac{dT}{T} e^{-Tm^2} \mathrm{Tr}_{M_n} e^{-T(-\partial_E^2)} \\
&= \frac{1}{2}\frac{1}{(4\pi)^{(D-1)/2}} V_{D-1} \int_{0^+}^{\infty} \frac{dT}{T^{(D+1)/2}} e^{-Tm^2} \mathrm{Tr}_{C_n} e^{-T(-\partial_E^2)} \quad (6.44)
\end{aligned}
$$

where $\partial_E^2 = \partial_\tau^2 + \partial_{\vec{x}}^2 + m^2$. Due to the locality of the action, the partition function in (6.44) is not expected to depend explicitly on the details of the Riemann surface. Thus, in order to calculate the non-trivial trace appearing in (6.44), we start with the finite temperature propagator of a free particle in cartesian coordinates:

$$A_{\beta_n}(\vec{x}\,', \vec{x}) = \langle \vec{x}\,' | e^{-T(-\partial_E^2)} | \vec{x} \,\rangle_{\beta_n}. \quad (6.45)$$

In (6.45) the $|\vec{x}\rangle$ denotes the the eigenstates of the position operator and the subscript $\beta_n = \beta n$ indicates the periodic boundary conditions imposed on the thermal Green's function. As it is obvious, they are dictated by the n folded structure of the Riemann space C_n. The next step is to transfer the result onto a two dimensional cone with angle deficit $2\pi(1-n)$:

$$ds^2 = d\rho^2 + \rho^2 n^2 d\theta^2, \ 0 \le \theta \le 2\pi. \quad (6.46)$$
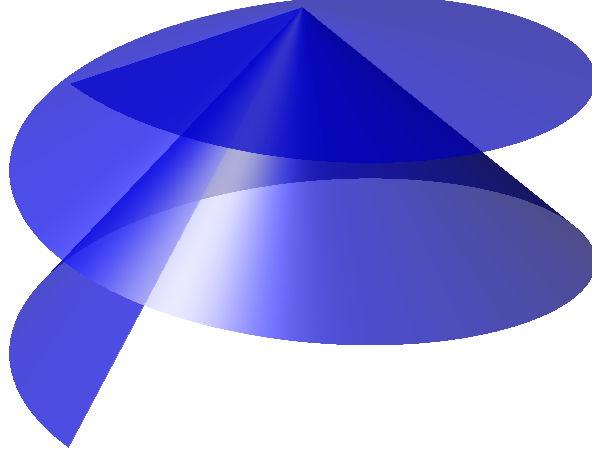
Figure 6.2: *Part of the two-dimensional space C_n, on which the path integration takes place.*

One can easily find that the free thermal propagator in (6.45) assumes the form [140]:

$$
\begin{aligned}
A_{\beta_n}(\vec{x}\,',\vec{x}) &= \frac{1}{4\pi T} \sum_{\nu=-\infty}^{\infty} e^{-\frac{1}{4T}\left[(x_1'-x_1)^2+(x_0'-x_0-\nu\beta_n)^2\right]} \\
&= \frac{1}{4\pi T} \sum_{\nu=-\infty}^{\infty} e^{-\frac{1}{4T}(\vec{x}'-\vec{x})^2+\frac{\nu\beta_n}{2T}(x_0'-x_0)-\frac{(\nu\beta_n)^2}{4T}}.
\end{aligned}
\tag{6.47}
$$

The above expression can be written in the conical metric (6.46) by making the replacements $x_0 = \rho\sin(n\theta)$, $x_1 = \rho\cos(n\theta)$, and using the expansion [141]:

$$
e^{iz\cos(n\theta)} = \sum_{m=-\infty}^{\infty} c_m J_{\frac{|m|}{n}}(z)e^{im\theta}, \ \ c_m = i^{\frac{|m|}{n}},
\tag{6.48}
$$

where $J_{\frac{|m|}{n}}$ are Bessel functions of the first kind. Thus, the thermal propagator on the surface (6.46) reads:

$$
\begin{aligned}
A_{\beta_n}(\rho',\theta';\rho,\theta;n) &= \frac{1}{4\pi it} \sum_{\nu,m,m_1,m_2} e^{-\frac{(\nu\beta)^2}{4it}} e^{-\frac{\rho'^2+\rho^2}{4it}} \times \\
&\times e^{im(\theta'-\theta)}e^{im_1\theta'+im_2\theta}e^{-\frac{i\pi(m_1+m_2)}{2n}} J_{\frac{|m|}{n}}\left(\frac{\rho'\rho}{2t}\right) \times \\
&\times J_{\frac{|m_1|}{n}}\left(\frac{\nu\beta_n}{2t}\rho'\right) J_{\frac{|m_2|}{n}}\left(\frac{\nu\beta_n}{2t}\rho\right) \times \\
&\times i^{-\frac{|m|}{n}} i^{\frac{|m_1|}{n}} (-i)^{\frac{|m_2|}{n}}.
\end{aligned}
\tag{6.49}
$$

In the last expression the rotation $T \to it$ has been adopted in order to secure convergence of all our intermediate steps.

Tracing out (6.49) we find:

$$
\begin{aligned}
A_{\beta_n} &= \mathrm{tr}_{C_n} \mathrm{e}^{-T(-\partial_E^2)} \\
&= \frac{1}{2it} \sum_{\nu,m,m_1} \mathrm{e}^{-\frac{(\nu\beta)^2}{4it}} i^{-\frac{|m|}{n}} \times \\
&\quad \times \int_0^\infty d\rho\rho \mathrm{e}^{-\frac{\rho^2}{2it}} J_{\frac{|m|}{n}}\left(\frac{\rho^2}{2t}\right) J_{\frac{|m_1|}{n}}^2\left(\frac{\nu\beta_n}{2t}\rho\right).
\end{aligned}
\tag{6.50}
$$

At this point we stress the fact that for $n \neq 1$, the trace over the conical metric (6.46), that is the integration over ρ, must be performed before the summations over m or m_1. The relevant calculations can be facilitated by using the fact that, apart for $Z_{n=1}$ which is easily calculated, we are only interested in the derivative of (6.50) with respect to n:

$$
\begin{aligned}
\left(\partial_n A_{\beta_n}\right)_{n=1} &= \frac{1}{2it} \sum_\nu \mathrm{e}^{-\frac{(\nu\beta)^2}{4it}} \partial_n \left[\sum_m \int_0^\infty d\rho\rho \mathrm{e}^{-\frac{\rho^2}{2it}} i^{-\frac{|m|}{n}} J_{\frac{|m|}{n}}\left(\frac{\rho^2}{2t}\right) \right]_{n=1} + \\
&\quad + \frac{1}{2it} \partial_n \left[\sum_{\nu,m} \mathrm{e}^{-\frac{(\nu\beta_n)^2}{4it}} \int_0^\infty d\rho\rho J_{\frac{|m|}{n}}\left(\frac{\nu\beta_n}{2t}\rho\right) \right]_{n=1}.
\end{aligned}
\tag{6.51}
$$

In obtaining the last expression we have used the identities:

$$
\sum_m i^{-m} J_m(z) = \mathrm{e}^{-iz}, \quad \sum_m J_m^2(z) = 1.
\tag{6.52}
$$

In Appendix D we prove that:

$$
\frac{1}{2it} \sum_m \int_0^\infty d\rho\rho \mathrm{e}^{-\frac{\rho^2}{2it}} i^{-\frac{|m|}{n}} J_{\frac{|m|}{n}}\left(\frac{\rho^2}{2t}\right)
$$
$$
\underset{it \to T}{=} n\frac{V_2}{4\pi T} + \frac{1}{12}\left(\frac{1}{n} - n\right) + \mathcal{O}\left(\frac{T}{V_2}\right)
\tag{6.53}
$$

and

$$
\frac{1}{2it} \sum_m \int_0^\infty d\rho\rho J_{\frac{|m|}{n}}^2\left(\frac{\nu\beta_n}{2t}\rho\right) \underset{it \to T}{=} \frac{V_2}{4\pi T} + \mathcal{O}\left(\frac{T}{V_2}\right).
\tag{6.54}
$$

In the above equations we introduced an upper cutoff R in the ρ-integrals and we have written as $V_2 = \pi R^2$ the volume of the two dimensional subspace. Substituting the first term in the rhs of (6.53) into (6.51) and feeding with the result (6.51) we find (see Appendix) that it leads to the logarithm of the partition function:

$$\frac{1}{2}\frac{V_{D-1}V_2}{(4\pi)^{\frac{D+1}{2}}}\int_{0^+}^{\infty}\frac{dT}{T^{\frac{D+3}{2}}}\,\mathrm{e}^{-Tm^2}\sum_{\nu}\mathrm{e}^{-\frac{(\nu\beta)^2}{4T}} = \ln Z_1(\beta). \qquad (6.55)$$

Following the same steps for the first term in the rhs of (6.54) we can prove that it is connected to the thermal entropy of the system:

$$\frac{1}{2}\frac{V_{D-1}V_2}{(4\pi)^{\frac{D+1}{2}}}\partial_n\left[\int_{0^+}^{\infty}\frac{dT}{T^{\frac{D+3}{2}}}\,\mathrm{e}^{-Tm^2}\sum_{\nu}\mathrm{e}^{-\frac{(\nu\beta)^2}{4T}}\right]$$
$$= \frac{1}{2}V_D\int\frac{d^Dp}{(2\pi)^D}\left(\ln(1-\mathrm{e}^{-\beta\omega})-\frac{\beta\omega}{\mathrm{e}^{\beta\omega}-1}\right) \qquad (6.56)$$

where $\omega^2 = p^2 + m^2$. The contribution to (6.51) of the second term in the rhs of (6.53) assumes the form:

$$\frac{1}{12}\frac{1}{(4\pi)^{\frac{D-1}{2}}}V_{D-1}\int_{0}^{\infty}\frac{dT}{T^{\frac{D+1}{2}}}\,\mathrm{e}^{-Tm^2}\sum_{\nu}\mathrm{e}^{-\frac{(\nu\beta)^2}{4T}}$$
$$= \frac{\pi}{6}V_{D-1}\int\frac{d^Dp}{(2\pi)^D\omega}\frac{1}{\tanh(\frac{\omega\beta}{2})}. \qquad (6.57)$$

Collecting everything together and using (6.44) we get the geometric entropy:

$$S_g = \frac{\pi}{6}V_{D-1}\int\frac{d^Dp}{(2\pi)^D\omega}\frac{1}{\tanh(\frac{\omega\beta}{2})} +$$
$$+\frac{1}{2}V_D\int\frac{d^Dp}{(2\pi)^D}\left(\ln(1-\mathrm{e}^{-\beta\omega})-\frac{\beta\omega}{\mathrm{e}^{\beta\omega}-1}\right). \qquad (6.58)$$

At the limit $p \to \infty$, $\tanh\left(\frac{\sqrt{p^2+m^2}\beta}{2}\right) \to 1$ and consequently the fist integral in (6.58) diverges. The same divergence appears in the case of zero temperature:

$$S_g(\beta = \infty) = \frac{\pi}{6}V_{D-1}\int\frac{d^Dp}{(2\pi)^D}\frac{1}{\sqrt{p^2+m^2}}$$
$$\to \frac{1}{12}\frac{V_{D-1}}{(4\pi)^{\frac{D-1}{2}}}m^{D-1}\Gamma\left(-\frac{D-1}{2},\frac{m^2}{\Lambda^2}\right). \qquad (6.59)$$

After this observation we are led to write:

$$S_g(\beta) = S_g(\beta = \infty) + \frac{\pi}{3}V_{D-1}\int\frac{d^D p}{(2\pi)^D\omega}\frac{1}{e^{\beta\omega}-1} +$$
$$+\frac{1}{2}S_{\text{thermal}}. \tag{6.60}$$

Some comments are in order at this point. The first term in the last expression represents the well known [110–119] entanglement entropy at zero temperature. This is a quantity that diverges in the absence of an ultraviolet cutoff, while it grows like the boundary surface of the excluded subregion. This fact clearly indicates the existence of very strong quantum correlations between fields defined at neighboring points, a direct consequence of a local quantum field theory. A quantitative explanation of such a behavior can be traced back to the uncertainty relations. Even at zero temperature, the notion of a sharp, well defined, boundary surface is more classical than quantum. The divergences appearing in $S_g(\text{T} = 0)$ are connected to the fact that in (6.59) we integrate down to zero distance, driving to infinity the density of the reduced density matrix eigenvalues. The second term is finite and well-defined for $m^2 > 0$. It is also proportional to the boundary surface and it is an increasing function of the temperature. We can consider it as a measure of the number of degrees of freedom that have been excited on the boundary surface due to the non-zero temperature and, consequently, as a measure of the thermal correlations between the partitions. The last term is the thermal entropy of the subsystem, an obviously extensive quantity. Subtracting this term from the geometric entropy we are led to find the following quantity:

$$I_m(\beta) = S_g(\beta = \infty) + \frac{\pi}{3}V_{D-1}\int\frac{d^D p}{(2\pi)^D\omega}\frac{1}{e^{\beta\omega}-1}. \tag{6.61}$$

which turns out to be proportional to the mutual information. In general the mutual information is a measure of all correlations, thermal and quantum. We use the following definition:

$$I(A : B) = S(\rho_A) + S(\rho_B) - S(\rho_{AB}). \tag{6.62}$$

For the case in hand the entropy of the combined system AB is just the total thermal entropy, $S(\rho_{AB}) = S_{\text{thermal}}$. The entropies of each one of the two subsystems are equal due to the way we have divided our system. Moreover, each one of them contains a part which is one half of the total thermal entropy of the system. Thus, their extensive thermal contribution to the mutual information is equal to $S(\rho_{AB})$ and when subtracting the latter, all contributions due to the thermal entropy will be eliminated. So, what (6.61) represents is the mutual information of the system divided by 2, $I_m(\beta) \equiv I(A : B)/2$.

6.1.5   Mutual Information and Bose-Einstein Condensation

Almost all of the technical details needed for the current section have already been exposed in the previous one. The basic difference of the analysis that follows, lies on the fact that we are now interested in charged scalar (non- interacting) fields. The field theoretical description will be based on complex fields while the introduction of a chemical potential (as a Lagrange multiplier) will ensure the conservation of the charge. In this framework, the partition function of the system assumes the form:

$$Z(\beta) = \int\limits_{\beta-\text{periodic}} \mathcal{D}\phi\mathcal{D}\phi^* \exp\left\{ -\int\limits_0^\beta d\tau \int d^D x \mathcal{L}[\phi, \phi^*]\right\}. \tag{6.63}$$

The Lagrangian entering the last expression can be written [137, 138] as follows:

$$\mathcal{L}[\phi, \phi^*] = \phi^*\big[-(\partial_\tau - \mu)^2 - \partial_{\vec{x}}^2 + m^2\big]\phi. \tag{6.64}$$

Following the same steps as in the previous section, we find:

$$\ln Z_n(\beta) = \frac{1}{(4\pi)^{\frac{D-1}{2}}} V_{D-1} \int\limits_0^\infty \frac{dT}{T^{\frac{D+1}{2}}} e^{-Tm^2} \text{Tr}_{C_n} e^{-T(-\partial_E^2 + 2\mu\partial_0 - \mu^2)}. \tag{6.65}$$

Once again we start from the free thermal propagator in Cartesian coordinates:

$$\begin{aligned}
A_{\beta_n}(\vec{x}\,', \vec{x}) &= \frac{1}{4\pi T} \sum_{\nu=-\infty}^\infty \exp\left\{ -\frac{1}{4T}(\vec{x}\,' - \vec{x})^2 + \right. \\
&\quad \left. + \Big(\frac{\nu\beta_n}{2T} + \mu\Big)(x_0' - x_0) - \frac{(\nu\beta_n)^2}{4T} - \mu\nu\beta_n\right\}
\end{aligned} \tag{6.66}$$

to arrive at the traced quantity that is relevant for the final calculation in (6.65):

$$\begin{aligned}
\text{Tr}_{C_n} e^{-T(-\partial_E^2 + 2\mu\partial_0 - \mu^2)} &\rightarrow n\text{Tr}_{C_1} e^{-T(-\partial_E^2 + 2\mu\partial_0 - \mu^2)} + \\
&\quad + \frac{1}{12}\left(\frac{1}{n} - n\right) \sum_\nu e^{-\frac{(\nu\beta)^2}{4T} - \mu\nu\beta} + \\
&\quad + \mathcal{O}\Big(\frac{T}{V_2}\Big)
\end{aligned} \tag{6.67}$$

where the arrow underlines the fact that we have followed the same steps as from (6.47) to (6.54) and we have kept only the non-extensive terms that are relevant for determining the mutual information.

In Appendix D we show that:

$$
\begin{aligned}
I_m &= \frac{\pi}{6} V_{D-1} \int \frac{d^D p}{(2\pi)^D \omega} \left\{ \frac{1}{\tanh\left[\frac{(\omega-\mu)\beta}{2}\right]} + \right. \\
&\left. \quad + \frac{1}{\tanh\left[\frac{(\omega+\mu)\beta}{2}\right]} \right\}.
\end{aligned} \tag{6.68}
$$

Isolating the (diverging) zero temperature contribution we find:

$$
\begin{aligned}
I_m &= S_g(\beta=\infty) + \frac{\pi}{6} V_{D-1} \int \frac{d^D p}{(2\pi)^D \omega} \left\{ \frac{1}{e^{(\omega-\mu)\beta}-1} + \right. \\
&\left. \quad + \frac{1}{e^{(\omega+\mu)\beta}-1} \right\}.
\end{aligned} \tag{6.69}
$$

For the system in hand the zero temperature entanglement entropy reads:

$$
\begin{aligned}
S_g(\beta=\infty) &= \frac{\pi}{3} V_{D-1} \int \frac{d^D p}{(2\pi)^D \omega} \\
&\rightarrow \frac{1}{6} \frac{V_{D-1}}{(4\pi)^{\frac{D-1}{2}}} m^{D-1} \Gamma\left(-\frac{D-1}{2}, \frac{m^2}{\Lambda^2}\right).
\end{aligned} \tag{6.70}
$$

To reveal the physical content of our results we shall focus on the well-studied $D=3$ case which hosts the Bose-Einstein condensation. As it is well-known [136–139] the quantitative realization of the phenomenon is different at the two opposite limits, the non-relativistic $\rho \ll m^3$ and the ultra-relativistic one $\rho \gg m^3$, as these are defined by the total charge density of the system.

Beginning from the non-relativistic case, in which the charge density is very low and the anti-particle contribution can be omitted [138], we rewrite (6.69) in the form:

$$
I_m^{\text{NR}}(\beta) = S_g(\beta=\infty) + \frac{\pi}{6} \frac{V_2}{m} \int \frac{d^3 p}{(2\pi)^3} \frac{1}{e^{(\frac{p^2}{2m}-\mu_{NR})\beta}-1} \tag{6.71}
$$

where we noted as $\mu_{\text{NR}}(\beta) = \mu - m \leq 0$ the non-relativistic chemical potential. The integral appearing in (6.71) is the total density of particles

occupying excited states:

$$\rho^e = \int \frac{d^3p}{(2\pi)^3} \frac{1}{e^{(\frac{p^2}{2m} - \mu_{\mathrm{NR}})\beta} - 1} = \left(\frac{m}{2\pi\beta}\right)^{3/2} \sum_{n=1}^{\infty} \frac{z_{\mathrm{NR}}^n}{n^{3/2}}, \qquad (6.72)$$

where $z_{\mathrm{NR}} = e^{\beta\mu_{NR}} \le 1$. For temperatures below a certain critical value $\mathrm{T_c}$ we have $\mu(\mathrm{T_c}) = m$ and the above quantity is a constant:

$$
\begin{aligned}
\rho^e &= \left(\frac{m}{2\pi\beta}\right)^{3/2} \sum_{n=1}^{\infty} \frac{1}{n^{3/2}} \\
&= \left(\frac{2\pi m}{\beta}\right)^{3/2} \zeta\left(\frac{3}{2}\right), \ 0 \le \mathrm{T} \le \mathrm{T_c}.
\end{aligned}
\qquad (6.73)
$$

At exactly the critical temperature the number (6.73) becomes the conserved total particle density of the system:

$$\rho^e = \rho = \left(\frac{2\pi m}{\beta_c}\right)^{3/2} \zeta\left(\frac{3}{2}\right). \qquad (6.74)$$

As an immediate consequence we get for the mutual information:

$$I_m^{\mathrm{NR}} = S_g(\mathrm{T} = 0) + \frac{\pi}{6}\frac{V_2}{m}\rho\left(\frac{\mathrm{T}}{\mathrm{T_c}}\right)^{3/2}, \ \mathrm{T} < \mathrm{T_c}. \qquad (6.75)$$

Above the critical temperature the system passes to the gas phase in which all of the particles occupy excited states. The mutual information reads now:

$$I_m^{\mathrm{NR}} = S_g(\mathrm{T} = 0) + \frac{\pi}{6}\frac{V_2}{m}\rho, \ \mathrm{T} > \mathrm{T_c}. \qquad (6.76)$$

Thus, the Bose-Einstein condensation and the relevant phase transition are reflected in a discontinuity of the derivative with respect to the temperature of the mutual information:

$$\left.\frac{\partial I_m^{\mathrm{NR}}}{\partial \mathrm{T}}\right|_{\mathrm{T} = \mathrm{T_c^-}} - \left.\frac{\partial I_m^{NR}}{\partial \mathrm{T}}\right|_{\mathrm{T} = \mathrm{T_c^+}} = \frac{\pi^2}{2}\zeta^{2/3}\left(\frac{3}{2}\right)V_2\rho^{1/3}. \qquad (6.77)$$

When $\rho \gg m^3$ we are approaching the ultra-relativistic limit, the critical temperature rises at relativistic high values $\mathrm{T_c} = (3|\rho|/m)^{1/2} \gg m$ and the

behavior of the system changes. Below the critical temperature, one easily finds that [136, 137]:

$$
\begin{aligned}
I_m &= S_g(\mathrm{T}=0) + \frac{\pi}{6}V_2 \int \frac{d^3p}{(2\pi)^3\omega}\left(\frac{1}{\mathrm{e}^{(\omega-\mu)\beta}-1} + \frac{1}{\mathrm{e}^{(\omega+\mu)\beta}-1}\right) \\
&\approx S_g(\mathrm{T}=0) + \frac{\pi V_2}{12}\frac{|\rho|}{m}\left(\frac{\mathrm{T}}{\mathrm{T_c}}\right)^2, \ \ \mathrm{T} < \mathrm{T_c}.
\end{aligned}
\tag{6.78}
$$

The integral that appears in (6.77) and (6.78) is not the charge density of the system and, consequently, is not a conserved quantity even for temperatures above the critical one. However, it is not hard to confirm [136] that at high temperatures $\mathrm{T} > \mathrm{T_c}$ it behaves as following:

$$
\begin{aligned}
&\int \frac{d^3p}{(2\pi^3)\omega}\left(\frac{1}{\mathrm{e}^{(\omega-\mu)\beta}-1} + \frac{1}{\mathrm{e}^{(\omega+\mu)\beta}-1}\right) \\
&= \frac{\mathrm{T}^2}{6} - \frac{\mathrm{T}}{2\pi}(m^2-\mu^2)^{1/2} - \frac{m^2}{4\pi^2}\ln\left(C\frac{m}{\mathrm{T}}\right) + \\
&\quad + \frac{1}{4\pi^2}(m^2-\mu^2) + \mathcal{O}\left(\frac{m^2}{\mathrm{T}^2}\right)
\end{aligned}
\tag{6.79}
$$

where $C = \mathrm{e}^{\gamma_E-1}/4\pi$ and γ_E is the Euler-Macheroni constant.

As in the non-relativistic case, the derivative of the mutual information with respect to the temperature possesses a discontinuity that reflects the underlying phase transition:

$$
\left.\frac{\partial I_m}{\partial \mathrm{T}}\right|_{\mathrm{T}=\mathrm{T_c^-}} - \left.\frac{\partial I_m}{\partial \mathrm{T}}\right|_{\mathrm{T}=\mathrm{T_c^+}} = -\frac{\pi\sqrt{3}}{9}V_2\left(\frac{|\rho|}{m}\right)^{1/2}.
\tag{6.80}
$$

The last result completes our study for the influence of the Bose-Einstein condensation on the entropy of entanglement in an ideal Bose system at finite temperature and non-zero chemical potential (grand canonical ensemble).

6.1.6   Conclusions

In this section we have performed two types of calculations and we have arrived at results with a clear physical content. First, we calculated the geometric entropy in an ideal Bose system at finite temperature and we confirmed the expected result: It combines the genuine quantum correlations with the thermal fluctuations, and it becomes an extensive quantity for an infinite system. Due to the simplicity of the system under consideration,

we were able to explicitly subtract from the geometric entropy its extensive component which coincides with the corresponding thermal entropy. This quantity is proportional to the so-called mutual information and grows like the surface that bounds the space region in which a system lives. The second calculation we performed refers to a Bose system at finite temperature at the grand canonical ensemble. We found that, at the critical temperature, the temperature derivative of the mutual information exhibits a finite discontinuity, and we explicitly calculated it. This result connects the condensation that appears in an ideal quantum Bose system with the spatial correlations between two regions of the system. This connection was shown by using a purely informational tool namely, the quantum mutual information.

6.2 Coherent State Path Integrals and the Bose-Hubbard Model

Almost seventy years ago R.P. Feynman [142, 143] introduced the path integral formalism, since then it has been proven a powerful tool for understanding and handling quantum mechanics, quantum field theory, statistical mechanics, even polymer physics and financial markets [144]. The introduction of the overcomplete base of coherent states [145–150], has expanded the concept of path integration into a complexified phase space enlarging its range of possible applications in many areas of physics and chemistry, mainly as a tool for semiclassical approximations. The path integration in terms of coherent states has been discussed in detail in a lot of excellent papers [151]. In most of them both the definition and the calculations are based on lattice regularization and the continuum limit is taken only after the relevant calculations have been performed. On the other hand, quantitative differences from the exact results have been reported [152] when one tries to handle coherent state path integrals and perform calculations directly in the continuum. From a conceptual point of view, path integrals in the continuum are considered as formal, unless a definite regularization prescription is given [149]. Nonetheless, the continuum form of path integration has been extensively used for perturbative approximations, for resuming perturbative series or for applying non-perturbative techniques. From this point of view, it looks annoying that time-continuous integration in a complexified phase space is plugged with problems. In this section we undertake the task of establishing a time-continuous formulation of path integration in the coherent states basis that does not face inconsistencies and reproduces the exact results at least in the cases in which the relevant Hamiltonian is expressed

in terms of creation and annihilation operators. Such a formulation may be proven a powerful tool for analytical and numerical applications since it allows the use of the quantum field theory toolbox. As a first attempt towards this direction, we examine, through a systematic perturbative expansion, the regime of strong interparticle interactions of the M-site Bose-Hubbard model, a widely used model in the physics of ultarcold atoms.

6.2.1 The Harmonic Oscillator

To set the stage, we begin with the trivial case of a harmonic oscillator

$$\hat{H}_0 = \frac{\hat{p}^2}{2} + \frac{\hat{q}^2}{2}. \tag{6.81}$$

The partition function of this system,

$$Z_0 = \mathrm{Tr} e^{-\beta \hat{H}_0} = \sum_{n=0}^{\infty} e^{-\beta(n+1/2)}, \tag{6.82}$$

can be expressed as a Feynman phase space integral

$$
\begin{aligned}
Z_0 &= \int \mathcal{D}p \int_{q(0)=q(\beta)} \mathcal{D}q \ \exp\left\{-\int_0^\beta d\tau [-ip\dot{q} + H_0(p,q)]\right\} \\
&= \frac{e^{-\beta/2}}{1-e^{-\beta/2}} = \sum_{n=0}^{\infty} e^{-\beta(n+1/2)}.
\end{aligned}
\tag{6.83}
$$

The integral in the left hand side of the above expression acquires a full meaning through its time-sliced definition [144]. However, in the simple case of the harmonic oscillator, the result (6.83) can be derived directly in the continuum.

In the phase space path integral as it appears in equation (6.83) we can make the canonical change of variables

$$q = (z^* + z)/\sqrt{2}, \ p = i(z^* - z)/\sqrt{2}. \tag{6.84}$$

In terms of the complex variables z, z^* equation (6.83) is transcribed into the following form [144]

$$
\begin{aligned}
Z_0 &= \int_{\mathrm{periodic}} \mathcal{D}^2 z \exp\left\{-\int_0^\beta d\tau \left[\frac{1}{2}(z^*\dot{z} - \dot{z}^*z) + |z|^2\right]\right\} \\
&= \sum_{n=0}^{\infty} e^{-\beta(n+1/2)}.
\end{aligned}
\tag{6.85}
$$

A comment is needed at this point. In the phase space integral (6.83) the integration over $q(\tau)$ is restricted by the periodic condition $q(0) = q(\beta)$ while the $p(\tau)$ integration is unrestricted. In the time-sliced expression that defines the integral, this means that we are dealing with $(q_0, ..., q_N; q_0 = q_N)$ "position" and $(p_1, ..., p_N)$ "momentum" integrations. To arrive at the periodic conditions accompanying the integral (6.85), one [144] introduces a fictitious p_0 variable which is set identically equal to p_N.

The partition function (6.85) can also be calculated by using the coherent states basis

$$
\begin{aligned}
Z_0 &= \int \frac{dz dz^*}{2\pi i} \langle z | e^{-\beta \hat{H}_0} | z \rangle \\
&= e^{-\beta/2} \int \frac{dz dz^*}{2\pi i} \langle z | e^{-\beta \hat{\alpha}^\dagger \hat{\alpha}} | z \rangle.
\end{aligned}
\tag{6.86}
$$

Following the standard steps [151], we find

$$
\langle z | e^{-\beta \hat{\alpha}^\dagger \hat{\alpha}} | z \rangle = \lim_{N \to \infty} \prod_{j=1}^{N-1} \int \frac{dz_j dz_j^*}{2\pi i} e^{-f_0(z^*, z)},
\tag{6.87}
$$

where

$$
f_0(z^*, z) = \sum_{j=0}^{N-1} \left[\frac{1}{2}(z_{j+1} - z_j) z_{j+1}^* - \frac{1}{2}(z_{j+1}^* - z_j^*) z_j + \varepsilon z_{j+1}^* z_j \right],
\tag{6.88}
$$

with $\varepsilon = \beta/N$. Note that the boundary conditions in equation (6.87) follow from the trace operation: $z_N^* = z^*$, $z_0 = z$.

Comparing expressions (6.85) and (6.87) we are led to define

$$
\int_{\text{periodic}} \mathcal{D}^2 z \exp \left\{ -\int_0^\beta d\tau \left[\frac{1}{2}(z^* \dot{z} - \dot{z}^* z) + |z|^2 \right] \right\}
$$
$$
= e^{-\beta/2} \lim_{N \to \infty} \prod_{j=1}^{N-1} \int \frac{dz_j dz_j^*}{2\pi i} e^{-f_0(z^*, z)}.
\tag{6.89}
$$

We consider relation (6.89) as a definition in the sence that it gives a concrete meaning to the formal integration over paths that go through a complexified phase space.

The definition (6.89) can also be read from the reverse point of view. Suppose that we are given the normal ordered Hamiltonian $\hat{H}_1 = \hat{\alpha}^\dagger \hat{\alpha}$ and we want to find the continuum limit of the relevant coherent sate path integral. Equation (6.89) dictates that we must begin by finding the position-momentum expression for the Hamiltonian in hand, $\hat{H} = \hat{p}^2/2 + \hat{q}^2/2 - 1/2$.

Then we have to construct the Feynman phase space path integral in which the Hamiltonian assumes its classical version $H_1^F = p^2/2 + q^2/2 - 1/2$. Making in this integral the variable change (6.84) we get $H_1^F = |z|^2 - 1/2$, thus obtaining the continuum limit we are looking for.

6.2.2   The One-Site Bose-Hubbard Model

As a more interesting example we investigate the one-site Bose-Hubbard model

$$\hat{H}_{BH} = E\hat{n} + \frac{U}{2}\hat{n}(\hat{n}-1),\tag{6.90}$$

where $\hat{n} = \hat{\alpha}^\dagger\hat{\alpha}$, E is the on-site energy and U is the interparticle interaction. The partition function of this system is readily seen to be

$$Z_{BH} = \mathrm{Tr}e^{-\beta\hat{H}_{BH}} = \sum_{n=0}^{\infty} e^{\left\{-\beta\left(En + \frac{U}{2}n(n-1)\right)\right\}}.\tag{6.91}$$

The same result can be obtained by going through path integration. As the above discussion has shown, the route begins by using the "position" and "momentum" operators to rewrite (6.90) in the form

$$\hat{H}_{BH} = -\frac{1}{2}(U-E)(\hat{p}^2 + \hat{q}^2) + \frac{U}{8}(\hat{p}^2 + \hat{q}^2)^2 - \frac{E}{2} + \frac{3U}{8}.\tag{6.92}$$

The partition function of the system can now be expressed as a Feynman phase space path integral

$$Z_{BH} = \int \mathcal{D}p \int_{q(0)=q(\beta)} \mathcal{D}q \ \exp\left\{[-ip\dot{q} + H_{BH}^F(p,q)]\right\}.\tag{6.93}$$

It is obvious that in the last expression, H_{BH}^F, stands for the classical version of the quantum Hamiltonian (6.92). Introducing the complex variables (6.84), we obtain

$$Z_{BH} = e^{-\beta\left(\frac{3U}{8} - \frac{E}{2}\right)} \int_{periodic} \mathcal{D}^2 z \, e^{-\int_0^\beta d\tau\left[\frac{1}{2}(z^*\dot{z} - \dot{z}^*z) - (U-E)|z|^2 + \frac{U}{2}|z|^4\right]}.\tag{6.94}$$

We shall prove that the above integral can be exactly calculated yielding the result (6.91). Before this, however, a comment is needed. The Hamiltonian entering in the last expression

$$H_{BH}^F(z, z^*) = -(U-E)|z|^2 + \frac{U}{2}|z|^4 - \frac{E}{2} + \frac{3U}{8}\tag{6.95}$$

seems (apart from a constant) to have been produced from a Weyl ordered quantum Hamiltonian. The point here is that we have begun from the Bose-Hubbard Hamiltonian (6.90) which is normal ordered.

The calculation of the integral (6.94) proceeds with the help of a Hubbard-Stratonovich [153–157] transformation. It can be realized by the introduction of the collective field $\zeta = |z|^2$ and the use of the functional identities

$$\int \mathcal{D}\zeta \ \delta[\zeta - |z|^2] = 1, \tag{6.96}$$

and

$$\delta[\zeta - |z|^2] = \int \mathcal{D}\sigma e^{-i \int_0^\beta d\tau \ \sigma(\zeta - |z|^2)}. \tag{6.97}$$

In this way the integral under consideration takes the form

$$Z_{BH} = e^{-\beta\left(\frac{3U}{8} - \frac{E}{2}\right)} \int \mathcal{D}\zeta \int \mathcal{D}\sigma e^{-i \int_0^\beta d\tau \zeta\sigma - \frac{U}{2} \int_0^\beta d\tau \zeta^2 + (U-E) \int_0^\beta d\tau \zeta}$$

$$\times \int_{\text{periodic}} \mathcal{D}^2 z \ e^{-\int_0^\beta d\tau \left[\frac{1}{2}(z^*\dot{z} - \dot{z}^*z) - i\sigma|z|^2\right]}. \tag{6.98}$$

The last functional integration can be performed directly in the continuum [144]. The result reads as follows

$$\int_{\text{periodic}} \mathcal{D}^2 z \ e^{-\int_0^\beta d\tau \left[\frac{1}{2}(z^*\dot{z} - \dot{z}^*z) - i\sigma|z|^2\right]} = \frac{e^{\frac{i}{2} \int_0^\beta d\tau\sigma}}{1 - e^{i \int_0^\beta d\tau\sigma}}. \tag{6.99}$$

Inserting this into equation (6.98), and assuming that a small positive imaginary part accompanies the field σ, we immediately find

$$Z_{BH} = e^{-\beta\left(\frac{3U}{8} - \frac{E}{2}\right)} \int \mathcal{D}\zeta \int \mathcal{D}\sigma e^{-i \int_0^\beta d\tau \zeta\sigma}$$

$$\times e^{-\frac{U}{2} \int_0^\beta d\tau \zeta^2 + (U-E) \int_0^\beta d\tau \zeta} \sum_{n=0}^{\infty} e^{i\left(n+\frac{1}{2}\right) \int_0^\beta d\tau\sigma}$$

$$= e^{-\beta\frac{3U}{8}} \sum_{n=0}^{\infty} e^{-\frac{U}{2}\beta\left(n+\frac{1}{2}\right)^2 + U\beta\left(n+\frac{1}{2}\right) - E\beta n}$$

$$= \sum_{n=0}^{\infty} e^{-\beta\left[En + \frac{U}{2}n(n-1)\right]} \tag{6.100}$$

Before proceeding, another comment is needed at this point. It would not be possible to calculate the path integral (6.94) if we had used polar coordinates $z = re^{i\theta}$. It is easy to check that in this case one arrives at a wrong

result [152]: For the integral (6.99) one gets $\sum_{n=0}^{\infty} \exp\{-in \int_0^{\beta} d\tau \sigma\}$ while the partition function assumes the form

$$Z'_{BH} = \mathrm{e}^{-\beta\left(\frac{3U}{8} - \frac{E}{2}\right)} \sum_{n=0}^{\infty} \mathrm{e}^{-(U-E)n\beta - \frac{U}{2}n^2\beta} \neq Z_{BH}. \tag{6.101}$$

The reason behind this result is that the use of polar coordinates for the calculation of a path integral directly in the continuum always yields the wrong answer. Only in the time-sliced version of a path integral the use of coordinates other than Cartesians is permitted [144]. Had we used the time-sliced definition for the integral (6.99)

$$\int_{\text{periodic}} \mathcal{D}^2 z \, \mathrm{e}^{-\int_0^{\beta} d\tau\left[\frac{1}{2}(z^*\dot{z} - \dot{z}^*z) + |z|^2 - i\sigma|z|^2\right]} = \mathrm{e}^{i\int_0^{\beta} d\tau\sigma} \lim_{N\to\infty} \prod_{j=0}^{N} \int \frac{dz_j dz_j^*}{2\pi i} \mathrm{e}^{-f(z^*,z)}, \tag{6.102}$$

with

$$f(z^*, z) = \sum_{j=0}^{N-1} \left[\frac{1}{2}(z_{j+1} - z_j)z_{j+1}^* - \frac{1}{2}(z_{j+1}^* - z_j^*)z_{j+1} + \varepsilon\sigma_j z_{j+1}^* z_j\right] \tag{6.103}$$

the change of variables $z_j = r_j \mathrm{e}^{i\theta_j}$ would have produced the right answer for the partition function. Note, in passing, that in our argument we considered relation (6.102) as a definition in the spirit of equation (6.89): One calculates the path integral directly in the continuum and then re-calculate the same expression using the coherent states base.

6.2.3 Correlation Functions

As long as we are interested in the partition function of a system, the measure of integration in terms of the (q, p) variables can be immediately translated into the measure of integration in terms of the (z, z^*) variables. The situation changes when we are interested in calculating path integrals with specific boundary conditions in the complexified phase space. This kind of calculations is tightly related with correlation functions that are the basic tools needed in any actual calculation pertaining to systems with interactions.

We can express propagators in the coherent state language beginning with the definition

$$\langle z_b | \hat{U}(T, 0) | z_a \rangle = \int_{\substack{z^*(T)=z_b^* \\ z(0)=z_a}} \mathcal{D}^2 z \, \mathrm{e}^{-\Gamma_{ba}} \mathrm{e}^{i\int_0^T dt\left[\frac{i}{2}(z^*\dot{z} - \dot{z}^*z) - H^F(z^*,z)\right]}. \tag{6.104}$$

In this expression we have denoted the time evolution operator as

$$\hat{U}(T,0) = \hat{T}\exp\left\{-i\int_0^T dt\ \hat{H}(t)\right\} \tag{6.105}$$

and we have used the abbreviation

$$\Gamma_{ba} = \frac{1}{2}\left(|z_b|^2 + |z_a|^2\right) - \frac{1}{2}\left(z_b^* z(T) + z^*(0)z_a\right). \tag{6.106}$$

The meaning of (6.104) is the following: In the left hand side one begins by dividing the time interval $(T,0)$ into small pieces $\varepsilon = T/N$, inserts in each step the coherent state resolution of the identity operator and following standard [151] steps is led to the time-sliced version of the coherent state path integral. The limit $N \to \infty$ of this discretized expression defines the path integral that appears in the right hand side in equation (6.102). Note that the definition (6.104) remains intact if the original quantum Hamiltonian is not normal ordered. If we begin, for example, with a Weyl or an anti-normal ordered Hamiltonian, the discretized form in the left had side uses the appropriate representation [151] for this Hamiltonian, while, in the right hand side, the H^F form is produced from the original Hamiltonian in its "position"-"momentum" version and the change of variables (6.84).

The consequences of the definition (6.104) can be trivially checked in the case of a harmonic oscillator with a frequency ω. Beginning from the right hand side we solve the classical equations of motion with boundary conditions $z_{\text{cl.}}^*(T) = z_b^*$, $z_{\text{cl.}}(0) = z_a$:

$$z_{\text{cl.}} = z_a e^{i\omega t}, \ \ z_{\text{cl.}}^* = z_b^* e^{-i\omega(T-t)}. \tag{6.107}$$

Making the replacements $z \to z + z_{\text{cl.}}$ and $z^* \to z^* + z_{\text{cl.}}^*$, we find

$$\int_{z_b^*, z_a} \mathcal{D}^2 z\, e^{-\Gamma_{ba}} e^{i\int_0^T d\tau\left[\frac{i}{2}(z^*\dot{z} - \dot{z}^* z) + |z|^2\right]}$$

$$= \exp\left\{z_b^* z_a e^{i\omega T} - \frac{1}{2}(|z_b|^2 + |z_a|^2)\right\} \times$$

$$\times \int_{z_b^* = z_a = 0} \mathcal{D}^2 z\, e^{-\Gamma_{ba}} e^{i\int_0^T d\tau\left[\frac{i}{2}(z^*\dot{z} - \dot{z}^* z) + |z|^2\right]}. \tag{6.108}$$

According to (6.104) the functional integral in the right hand side of equation (6.108) is the vacuum expectation value of the time evolution operator of the harmonic oscillator

$$\langle 0|\hat{U}(T,0)|0\rangle = e^{-i\omega T/2}. \tag{6.109}$$

Inserting eq. (6.109) into equation (6.108) we find the harmonic oscillator propagator in the coherent state representation, a result that could have been produced [151] directly from the left hand side of the definition (6.104).

Another simple case in which the definition (6.104) can be used for calculations directly in the continuum is the case of the one-site Bose-Hubbard model (6.90). First of all, the propagator $K_{ba} = \langle z_b | \exp\{-iT\hat{H}_{BH}\} | z_a \rangle$ is immediately seen to have the form

$$
\begin{aligned}
K_{ba} &= \sum_{n,m} \langle z_b | n \rangle \langle n | \mathrm{e}^{-iT\hat{H}_{BH}} | m \rangle \langle m | z_a \rangle \\
&= \exp\left\{ -\frac{1}{2}(|z_b|^2 + |z_a|^2) \right\} \sum_n \frac{(z_b^* z_a)^n}{n!} \mathrm{e}^{-iEnT - i\frac{U}{2}n(n-1)}. \quad (6.110)
\end{aligned}
$$

Using the identity

$$
\begin{aligned}
\mathrm{e}^{-i\frac{TU}{2}n(n-1)} &= \mathrm{e}^{i\frac{UT}{8}} \mathrm{e}^{-i\frac{TU}{2}(n-1/2)^2} \\
&= \mathrm{e}^{i\frac{UT}{8}} \sqrt{\frac{T}{2i\pi U}} \int_{-\infty}^{\infty} d\omega\, \mathrm{e}^{i\frac{T}{2U}\omega^2 + iT\omega(n-1/2)} \quad (6.111)
\end{aligned}
$$

we can rewrite the propagator into the following exact form [152]

$$
\begin{aligned}
K_{ba} &= \mathrm{e}^{i\frac{UT}{8}} \sqrt{\frac{T}{2i\pi U}} \int_{-\infty}^{\infty} d\omega \exp\left\{ i\frac{T}{2U}\omega^2 - \frac{i\omega T}{2} \right. \\
&\qquad \left. + z_b^* z_a \mathrm{e}^{i(\omega - E)T} - \frac{1}{2}(|z_a|^2 + |z_b|^2) \right\}. \quad (6.112)
\end{aligned}
$$

We can arrive at the same result starting from the functional integral

$$
K_{ba} = \int_{\substack{z^*(T) = z_b^* \\ z(0) = z_a}} \mathcal{D}^2 z\; \mathrm{e}^{-\Gamma_{ba}} \mathrm{e}^{i\int_0^T dt \left[\frac{i}{2}(z^*\dot{z} - \dot{z}^* z) - H^F(z^*, z) \right]} \quad (6.113)
$$

in which the Hamiltonian is defined in equation (6.95). Once again, the Hubbard-Stratonovich transformation can be used to recast the integral (6.113) into the form

$$
\begin{aligned}
K_{ba} &= \mathrm{e}^{-iT\left(\frac{3U}{8} - \frac{E}{2} \right)} \mathrm{e}^{-\frac{1}{2}(|z_a|^2 + |z_b|^2)} \times \\
&\quad \times \int \mathcal{D}\zeta \int \mathcal{D}\sigma\, \mathrm{e}^{-i\int_0^T dt\sigma\zeta - i\frac{U}{2}\int_0^T dt\zeta^2 + i(U - E)\int_0^T dt\zeta} \tilde{K}_{ba}, \quad (6.114)
\end{aligned}
$$

where

$$
\begin{aligned}
\tilde{K}_{ba} &= \int_{z_b^*, z_a} \mathcal{D}^2 z\; \mathrm{e}^{i\int_0^T dt \left[\frac{i}{2}(z^*\dot{z} - \dot{z}^* z) + \sigma|z|^2 \right] + \frac{1}{2}\left(z_b^* z(T) + z^*(0)z_a \right)} \\
&= \exp\left\{ \frac{i}{2} \int_0^T dt\sigma + z_a z_b^* \mathrm{e}^{i\int_0^T dt\sigma} \right\}. \quad (6.115)
\end{aligned}
$$

In order to arrive at the result indicated in the second line of the above expression, we have made the replacements $z \to z + z_{\text{cl.}}$ and $z^* \to z^* + z^*_{\text{cl.}}$ where

$$z_{\text{cl.}} = z_a \mathrm{e}^{-\frac{i}{\hbar} \int_0^t dt' \sigma}, \ z^*_{\text{cl.}} = z^*_b \mathrm{e}^{-\frac{i}{\hbar} \int_t^T dt' \sigma} \tag{6.116}$$

are the solutions of the classical equations of motion, and at the same time we have used the vacuum expectation value of a harmonic oscillator with a time-depended frequency σ [144].

Inserting equation (6.115) into equation (6.114), we get

$$K_{ba} = \mathrm{e}^{-iT\frac{3U}{8}} \mathrm{e}^{-\frac{1}{2}(|z_a|^2 + |z_b|^2)} \sum_{n=0}^{\infty} \frac{(z_a z^*_b)^n}{n!} \mathrm{e}^{-iTEn - i\frac{U}{2}T\left(n+\frac{1}{2}\right)^2 + iUT\left(n+\frac{1}{2}\right)}. \tag{6.117}$$

Using now the identities

$$\int_{-\infty}^{\infty} dx \delta(x - n - 1/2) = 1, \tag{6.118}$$

$$T \int_{-\infty}^{\infty} \frac{d\omega}{2\pi} \mathrm{e}^{-i\omega T(x-n-1/2)} = \delta(x - n - 1/2) \tag{6.119}$$

expression (6.117) turns to the exact result (6.112).

6.2.4 The Bose-Hubbard Model

$\mathfrak{T}$he advantage of using functional integrals for the analysis of models like the Bose-Hubbard, is that we can borrow well-established techniques from the realm of quantum field theories. To be concrete, let us discuss the M-site Bose-Hubbard Hamiltonian

$$\hat{H}_{BH} = E \sum_{j=1}^{M} \hat{n}_j - J \sum_{\langle i,j \rangle} (\hat{\alpha}_i^{\dagger} \hat{\alpha}_j + \hat{\alpha}_j^{\dagger} \hat{\alpha}_i) + \frac{U}{2} \sum_{j=1}^{M} \hat{n}_j(\hat{n}_j - 1). \tag{6.120}$$

For simplicity reasons we assumed that the lattice is flat, $E_j = E$. The coherent state representation of the Green's function of this system can be found by using the rules we used for the one-site model

$$K_{ba}^M = \int_{\substack{\vec{z}^*(T) = \vec{z}^*_b \\ \vec{z}(0) = \vec{z}_a}} \mathcal{D}^2 \vec{z} \, \mathrm{e}^{-\Gamma_{ba}} \mathrm{e}^{i \int_0^T dt \left[\frac{i}{2} (\vec{z}^* \cdot \dot{\vec{z}} - \dot{\vec{z}}^* \cdot \vec{z}) - H_{MBH}^F(\vec{z}^*, \vec{z}) \right]}. \tag{6.121}$$

In this integral we defined a M dimensional vector $\vec{z} = (z_1, ..., z_M)$ and we have generalized accordingly the expressions (6.95) and (6.104)

$$
\begin{aligned}
H_{MBH}^F &= \sum_j \left[-(U-E)|z_j|^2 + \frac{U}{2}|z_j|^4 - \frac{E}{2} + \frac{3U}{8} \right] \\
&\quad -J\sum_{\langle i,j \rangle} (z_i^* z_j + z_j^* z_i), \quad\quad (6.122) \\
\Gamma_{ba} &= \frac{1}{2}\left(|\vec{z}_b|^2 + |\vec{z}_a|^2 \right) - \frac{1}{2}\left(\vec{z}_b^* \cdot \vec{z}(T) + \vec{z}^*(0) \cdot \vec{z}_a \right). \quad (6.123)
\end{aligned}
$$

In the functional measure the integration in the M dimensional space are defined as

$$
\int d^2 \vec{z} \equiv \prod_{j=1}^N \int \frac{dz_j^* dz_j}{2\pi i}. \quad\quad (6.124)
$$

The propagator (6.121) is the basis for the analytic calculation of any experimentally relevant quantity. As a specific example, we can consider the time-evolution of the elements of the SPDM

$$
\begin{aligned}
\langle \hat{\alpha}_i^\dagger \hat{\alpha}_j \rangle &= \left(\prod_{k=1}^4 \int d^2 \vec{z}^{\,(k)} \right) e^{-\frac{1}{2}(|\vec{z}^{\,(1)}|^2 + |\vec{z}^{\,(2)}|^2) - 2\vec{z}^{\,(1)*} \cdot \vec{z}^{\,(2)}} \times \\
&\quad \times \langle \psi_0 | \vec{z}^{\,(3)} \rangle (K^{M\dagger})_{31} z_i^{(1)*} z_j^{(2)} (K^M)_{24} \langle \vec{z}^{\,(4)} | \psi_0 \rangle. \quad (6.125)
\end{aligned}
$$

In this expression $|\psi_0\rangle$ is the initial state while the propagators are defined in equation (6.121).

It is apparent that expressions like the full propagator (6.121) or the correlation function (6.125) cannot be evaluated exactly. However these expressions can serve as the basis for applying approximations techniques that can systematically go beyond the semiclassical or the mean-field approximation.

As a first try, we can use expression (6.121) to analyze the region of weak tunneling strength. The road is known. It begins with the cluster expansion [158] that enables us to write the propagator (6.121) in the form

$$
\begin{aligned}
K_{ba}^M(J) &= K_{ba}^M(0) \left\langle e^{-iJ \sum_{\langle i,j \rangle} \int_0^T (z_i^* z_j + z_j^* z_i)} \right\rangle_z \quad\quad (6.126) \\
&= K_{ba}^M(0) e^{-iJ \sum_{\langle i,j \rangle} \int_0^T \langle z_i^* z_j + z_j^* z_i \rangle_z + \mathcal{O}(J^2)}
\end{aligned}
$$

with

$$
\langle (...) \rangle_z \equiv K_{ba}^{M-1}(0) \int_{\substack{\vec{z}^*(T)=\vec{z}_b^* \\ \vec{z}(0)=\vec{z}_a}} \mathcal{D}^2 \vec{z}\, e^{-\Gamma_{ba}} (...) e^{i\int_0^T dt \left[\frac{i}{2}(\vec{z}^* \cdot \dot{\vec{z}} - \dot{\vec{z}}^* \cdot \vec{z}) - H_{MBH}^F(J=0) \right]}. \quad (6.127)
$$

The next step is the introduction of the generating functional

$$K_{ba}^\ell(I, I^*) = K_{ba}^\ell(0,0) \int_{\substack{z^*(T)=z_{\ell b}^* \\ z(0)=z_{\ell a}}} \mathcal{D}^2 z \; e^{-\Gamma_{\ell ba}} \tag{6.128}$$

$$\times e^{i \int_0^T dt \left[\frac{i}{2}(z^*\dot{z} - \dot{z}^* z) - H_{BH}^F(z^*, z) - I_\ell z^* - I_\ell^* z \right]}.$$

The Hamiltonian in this expression is the one-site Bose-Hubbard Hamiltonian (6.95) while the weight in the measure has the form

$$\Gamma_{\ell ba} = \frac{1}{2}\left(|z_{\ell b}|^2 + |z_{\ell a}|^2\right) - \frac{1}{2}\left(z_{\ell b}^* z(t_b) + z^*(t_a) z_{\ell a}\right). \tag{6.129}$$

In terms of the generating functional the first order correlation function appearing in eq. (6.126) is read from the following expression

$$\langle z_i^* z_j + z_j^* z_i \rangle_z = -\left[\frac{\delta^2}{\delta I_i \delta I_j^*} + (i \leftrightarrow j)\right] \prod_{\ell=1}^M K_{ba}^\ell(I, I^*)\Bigg|_{I=I^*=0}. \tag{6.130}$$

From the technical point of view the integral (6.128) is a one-site Bose-Hubbard model coupled linearly to external sources. We can calculate it by using the rules established in the first part of our discussion. We perform the Hubbard-Stratonovich transformation and we solve the classical equations of motion with the appropriate boundary conditions. The result has the form

$$K_{ba}^\ell(I, I^*) = \int \mathcal{D}\zeta \int \mathcal{D}\sigma e^{-iF(\zeta, \sigma)}$$

$$\times \exp\left\{ iz_{\ell a} \int_0^T dt I_\ell^*(t) \Delta_\sigma(t, 0) \right.$$

$$+ iz_{\ell b}^* \int_0^T dt I_\ell(t) \Delta_\sigma(T, t) \tag{6.131}$$

$$\left. - \int_0^T dt \int_0^T dt' I_\ell^*(t) \Delta_\sigma(t, t') I_\ell(t') \right\}.$$

In this integral we have written

$$\Delta_\sigma(t, t') = \theta(t - t') e^{-i \int_{t'}^t d\tau \sigma} \tag{6.132}$$

and

$$F = T\left(\frac{3U}{8} - \frac{E}{2}\right) - \frac{i}{2}\left(|z_{\ell b}|^2 + |z_{\ell a}|^2\right)$$

$$+ \int_0^T dt \left(\frac{U}{2}\zeta^2 + \zeta\sigma - (U - E)\zeta\right). \tag{6.133}$$

Now, the calculation of the correlation function (6.130) is straightforward

$$\langle z_i^* z_j + z_j^* z_i \rangle_z = \sum_{\langle i,j \rangle} z_{ia} z_{jb}^* \frac{\Lambda_i(t) \Lambda_j(T-t)}{\Lambda_i(0) \Lambda_j(0)} + (i \leftrightarrow j), \qquad (6.134)$$

where we have defined the functions

$$\Lambda_i(t) = \int_{-\infty}^{\infty} d\omega \, \mathrm{e}^{z_{ia} z_{ib}^*} \mathrm{e}^{i(\omega-E)T} \, \mathrm{e}^{i \frac{\omega^2 T}{2U} - i\omega T \left(\frac{1}{2} - \frac{t}{T} \right)}. \qquad (6.135)$$

6.2.5 Conclusions

In this chapter we have introduced a method for defining and using time-continuous coherent state path integrals without facing inconsistencies. The Hamiltonian that weights the paths in the complexified phase space is produced through three simple steps. In the first step, one rewrites the second quantized Hamiltonian $\hat{H}(\hat{\alpha}^\dagger, \hat{\alpha})$ in terms of "position" and "momentum" operators. he second step consists of taking the classical form of this Hamiltonian, that is, the form entering into the phase-space Feynman path integral, $H^F(p,q)$. The third step is just a canonical change of variables that produces the final form $H^F(z^*, z)$ which enters into the time-continuous form of the coherent state path integral. We have applied the method for the simple case of the one- site Bose-Hubbard model and we have derived the correct expressions for the partition function and the propagator of the system. In order to demonstrate the abilities of the proposed formulation we have also derived an approximate expression for the propagator of an interacting M-site Bose-Hubbard chain at the limit of small tunneling strength.

Conclusions and Outlook

The present thesis could be divided into two parts. In the first part we have discussed the influence of localized single particle losses on the dynamics of a BEC in a one dimensional optical lattice. In the second part we present calculations and develop methods for the study of open or closed bosonic systems based on the path integral formalism. Both parts serve the same purpose: the development and application of beyond mean-field methods for open or closed bosonic systems.

Localized single particle loss can be proven a very useful tool to control the many-body dynamics. As we have shown one can use this elementary dissipation mechanism to engineer stable nonlinear structures in one dimensional optical lattices. Discrete breathers can be emerge if we properly combine strong interparticle interactions and boundary particle losses. Also, stable coherent dark solitons can be created if in addition of particle losses we use phase engineering. Although, solitons can be predicted already by the mean-field approximation, beyond mean-field calculations can reveal very important characteristics of the evolution of such systems. For example, the BBR method we have used predicts the formation of discrete breathers for weaker losses, than the mean-field approximation, in agreement with the exact results. Another striking effect we have predicted is that strong losses can actually suppress the decay of the condensate. This is consequence of the inhibition of quantum tunneling due to the losses, an effect related to the quantum Zeno effect.

Furthermore, we have proven that the localized losses together with strong interactions and a dynamically unstable initial BEC state deterministically lead to the formation of a macroscopically entangled breather state. These states show remarkable statistical properties, since the atoms relax to a coherent superposition of bunches localized at different lattice positions. Using a semiclassical interpretation we have revealed the connection of the breather state formation with a classical bifurcation of the associated mean-field dynamics. The breather states generalize the so-called NOON states, enabling interferometry beyond the standard quantum limit.

The formation and the properties of the nonlinear structures we discussed here (discrete breathers, dark solitons and entangled breather states), could be readily observed in ongoing experiments with ultracold atoms in quasi one dimensional optical lattices. As we have already discussed, a very promising candidate is the experimental setup used by the group of Prof. Dr. Herwing Ott.

Non-equilibrium transport is another topic related with what we have discussed. Here the environment is used not to engineer the dynamics but to bring the system out of equilibrium. We have introduced a simple theoretical model which based on the Bose-Hubbard model and we have studied the steady state properties in the absence and presence of interactions. Our analysis shows that the observed differences between the two cases are related with the mean-field self-trapping effect.

The second part of the thesis begins with an alternative and original investigation of the Bose-Einstein phenomenon. The phenomenon is studied in the framework of relativistic quantum field theory, by using functional integral methods. Our goal is to probe the implications on the spatial correlations of an ideal bosonic system. The system, which is in a thermal state, is spatially divided into two regions and the von Neumann entropy is calculated if we integrate out one of the regions. Since, the system is in a thermal state there are both statistical and quantum contributions in the entropy, which however can be easily identified in the analytical result. By subtract the statistical part one defines the so-called mutual information. We show that the Bose-Einstein condensation and the relevant phase transition are reflected in a discontinuity of the derivative with respect to the temperature of the mutual information. In this way the correct critical temperature is predicted in the relativistic and nonrelativistic case. Except of the technical importance of the the analytical calculation, this study helps the reader to see the BEC from the perspective of quantum information theory, since geometric entropy and mutual information are purely quantum informational quantities.

Finally, at the end of the thesis we develop a formalism which allows the use of coherent state path integrals directly in the continuum for second quantized models, like the Bose-Hubbard. It has been shown that coherent states path integrals present inconsistencies when they are used in the continuum. So here we propose a method consisting of a few simple steps that producing the right expression for the continuous form of the coherent state path integral. The method has been applied to the one-site Bose-Hubbard model -where the result is known- giving the right expression for the partition function. The advantage of a continuous-time path integral is that one can use well-established perturbative and non-perturbative methods from the

realm of quantum field theories. Indeed, we calculate the correlation functions of an M-site Bose-Hubbard chain in the strong interparticle regime by keeping in the cluster expansion the first order in the tunneling strength.

The significant progress of the experiments with ultracold atoms of the last years are pressing for a deeper understanding of the systems under consideration. Thus, theoretical works which can give predictions beyond the usual mean-field approximations are of great importance. The present work indicates that indeed there is a lot of interesting physics that should be studied. For example, it would be interesting to study the stability of moving and colliding solitons with beyond mean-field methods. Also, nonlinear structures that exhibit purely quantum properties, such as entanglement, are an exciting subject for further investigation. The methods used and developed in this thesis can help towards this direction. In particular the proposed coherent state path integral formalism can open new possibilities for the study of second quantized systems, since the derived expressions can serve as the basis for applying approximation techniques that can systematically go beyond the semi-classical or mean-field limit. The method can be easily extended for open quantum systems with the help of the Feynman-Vernon theory, allowing the analytical and numerical investigation of open systems like the dissipative Bose-Hubbard model we have discussed here. Another interesting field of growing interest, due to its possible applications, is non-equilibrium bosonic transport. Here also better approximations are needed. In [78] we have used approximate methods based on non-equilibrium Green's function method, however there is enough room for improvement of this approach.

Appendix A

The Quantum Jump Method

The quantum jump or Monte Carlo wave-function method [93] is a useful numerical method which allows exact solution for Master equations of the form (1.59), the. The advantage of this method is that instead of evolving the initial density matrix $\hat{\sigma} = |\psi_{\text{in.}}\rangle\langle\psi_{\text{in.}}|$, we evolve the state vector $|\psi_{\text{in.}}\rangle$ using a stochastic procedure and averaging over the possible outcomes.

The method consists of a continuous evolution using an effective non-Hermitian Hamiltonian of the form

$$\hat{H}_{\text{eff.}} = \hat{H}_{\text{s}} - i \sum_j \frac{\gamma_j}{2} \hat{L}_j^\dagger \hat{L}_j \tag{A.1}$$

which is interrupted by stochastic quantum jumps. The jumps happen with probability

$$\delta p = \gamma_j \langle\psi|\hat{L}_j^\dagger \hat{L}_j|\psi\rangle \delta t \tag{A.2}$$

during a short time interval δt and leads to the state

$$|\psi\rangle \to \frac{\hat{L}_j|\psi\rangle}{||\hat{L}_j|\psi\rangle||}. \tag{A.3}$$

We must note that after every time step one should renormalize the state vector $|\psi\rangle$, since $\hat{H}_{\text{eff.}}$ is non-Hermitian. Now one can prove [93] that the solution of the Master equation (1.59) can be obtained if we average over many of these random trajectories.

The calculation of an arbitrary observable $\hat{O}$ is straight forward. One takes the mean value of the quantum average $\langle\psi^{(k)}(t)|\hat{O}|\psi^{(k)}(t)\rangle$ over the various outcomes $|\psi^{(k)}(t)\rangle$ of the above process

$$\langle O\rangle(t) \xrightarrow[N_{\text{t}}\gg 1]{} \frac{1}{N_{\text{t}}} \sum_{j=1}^{N_{\text{t}}} \langle\psi^{(k)}(t)|\hat{O}|\psi^{(k)}(t)\rangle, \tag{A.4}$$
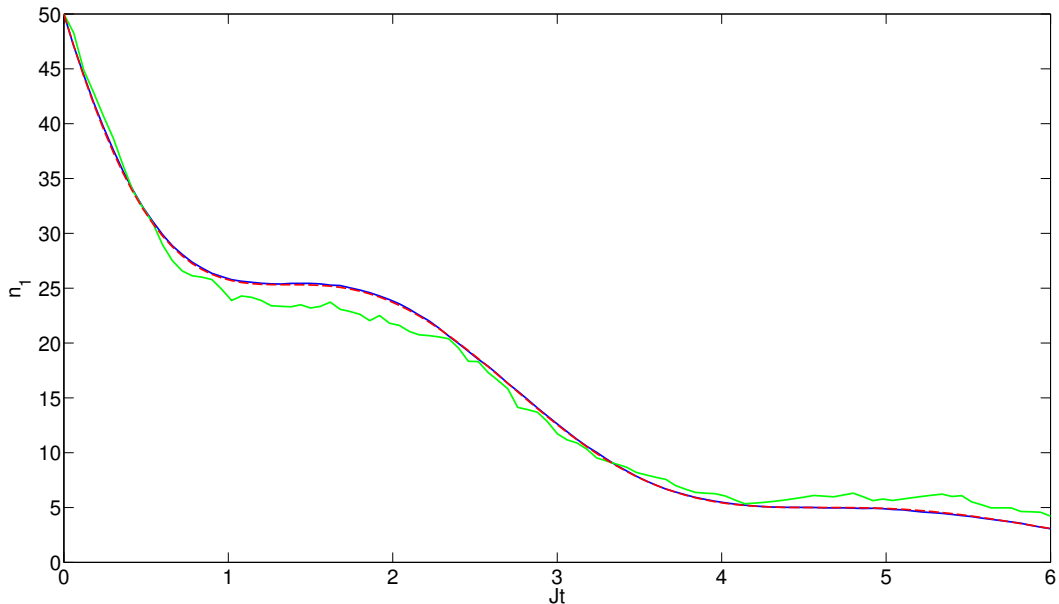
127

Figure A.1: *A comparison of a quantum jump simulation for 2 (solid green line) and 200 (solid blue line) trajectories and the analytical results (dashed red lines) for a double well. Shown is the time evolution of the population in the first well n_1. The parameters are: $U = 0$, $\gamma_1 = J$ and $\gamma_2 = 0$. The initial states is a pure BEC with $n_1(0) = n_2(0) = 30$ and phase difference of π between wells.*

where N_t is the number of trajectories.

In figure A.1 we have solved Master equation (2.1) for a double well without interactions using the quantum jump method and compare the result with the analytical one for the population in the first site

$$n_1(t) = n_\mathrm{tot}(0)\mathrm{e}^{-\frac{\gamma_1}{2}t}\left[\frac{J^2}{2\omega^2} - \frac{\gamma_1^2}{32\omega^2}\cos(2\omega t) - \frac{\gamma_1}{8\omega}\sin(2\omega t)\right], \qquad \text{(A.5)}$$

with the frequency $\omega = \sqrt{J^2 - \gamma_1^2/16}$. One can see that there is an excellent agreement between the analytical result and the quantum jump method for 200 trajectories.

Appendix B

The Truncated Wigner method

In this appendix, we explicitly derive the evolution equation for the Wigner function which corresponds to the Master equation (2.1). Furthermore, we introduce the so-called truncated Wigner approximation, a useful semi-classical approximation for the Wigner function evolution equation. In order to translate the Master equation (2.1) to an equation for the Wigner function we use the following operator correspondences [96]:

$$\hat{\alpha}_j \hat{\rho} \;\leftrightarrow\; \left(\alpha_j + \frac{1}{2} \frac{\partial}{\partial \alpha_j^*} \right) \mathcal{W}, \tag{B.1}$$

$$\hat{\rho} \hat{\alpha}_j \;\leftrightarrow\; \left(\alpha_j - \frac{1}{2} \frac{\partial}{\partial \alpha_j^*} \right) \mathcal{W}, \tag{B.2}$$

$$\hat{\alpha}_j^\dagger \hat{\rho} \;\leftrightarrow\; \left(\alpha_j^* - \frac{1}{2} \frac{\partial}{\partial \alpha_j} \right) \mathcal{W}, \tag{B.3}$$

$$\hat{\rho} \hat{\alpha}_j^\dagger \;\leftrightarrow\; \left(\alpha_j^* + \frac{1}{2} \frac{\partial}{\partial \alpha_j} \right) \mathcal{W}, \tag{B.4}$$

where α_j is the eigenvalues of the destruction operator:

$$\hat{\alpha}_j |\alpha_j\rangle = \alpha_j |\alpha_j\rangle, \;\; \langle \alpha_j | \hat{\alpha}_j^\dagger = \alpha_j^* \langle \alpha_j |. \tag{B.5}$$

Substituting these correspondences in the Master equation (2.1), we obtain

the following evolution equation for the Wigner function:

$$
\begin{aligned}
\partial_t \mathcal{W} \;=\; & 2J \sum_{j=1}^{M-1} \Im\left[\left(\alpha_j - \frac{1}{2}\frac{\partial}{\partial \alpha_j^*}\right)\left(\alpha_{j+1}^* + \frac{1}{2}\frac{\partial}{\partial \alpha_{j+1}}\right) \right. \\
& \left. - \left(\alpha_{j+1}^* - \frac{1}{2}\frac{\partial}{\partial \alpha_{j+1}}\right)\left(\alpha_j + \frac{1}{2}\frac{\partial}{\partial \alpha_j^*}\right) \right]\mathcal{W} \\
& + U\sum_{j=1}^{M} \Im\left(\alpha_j - \frac{1}{2}\frac{\partial}{\partial \alpha_j^*}\right)^2 \left(\alpha_j^* + \frac{1}{2}\frac{\partial}{\partial \alpha_j}\right)^2 \mathcal{W} \qquad \text{(B.6)} \\
& - \sum_{j=1}^{M} \frac{\gamma_j}{2}\left[\left(\alpha_j^* - \frac{1}{2}\frac{\partial}{\partial \alpha_j}\right)\left(\alpha_j + \frac{1}{2}\frac{\partial}{\partial \alpha_j^*}\right) \right. \\
& + \left(\alpha_j - \frac{1}{2}\frac{\partial}{\partial \alpha_j^*}\right)\left(\alpha_j^* + \frac{1}{2}\frac{\partial}{\partial \alpha_j}\right) \\
& \left. - 2\left(\alpha_j + \frac{1}{2}\frac{\partial}{\partial \alpha_j^*}\right)\left(\alpha_j^* + \frac{1}{2}\frac{\partial}{\partial \alpha_j}\right) \right]\mathcal{W}.
\end{aligned}
$$

As one can easily see the above equation includes not only first and second order derivatives, but also third order ones arising from the interaction term (the U-dependent term in the second line of equation (B.7)). These third order derivatives makes the equation quickly unstable, so an approximate method is needed. One technique that is widely used in optical systems is the truncated Wigner method [94, 95], which is a good approximation as far as the mode occupation numbers are large. In this approximation one neglects all the terms that include third order derivatives, thus we have the equation

$$
\begin{aligned}
\partial_t \mathcal{W} \;=\; & \sum_j \frac{\partial}{\partial x_j}\left[J(y_{j+1} + y_{j-1}) + U(y_j - x_j^2 y_j - y_j^3) + \frac{\gamma_j}{2}x_j \right]\mathcal{W} \\
& + \sum_j \frac{\partial}{\partial y_j}\left[-J(x_{j+1} + x_{j-1}) - U(x_j - x_j y_j^2 - x_j^3) + \frac{\gamma_j}{2}y_j \right]\mathcal{W} \\
& + \frac{1}{2}\sum_j \frac{\gamma_j}{4}\left(\frac{\partial^2}{\partial x_j^2} + \frac{\partial^2}{\partial y_j^2}\right)\mathcal{W}, \qquad \text{(B.7)}
\end{aligned}
$$

where x_j, y_j are the real and imaginary part of α_j respectively.

Equation (B.7) is a Fokker-Planck equation, thus it can be rewritten in the language of stochastic differential or Langevin equations. To be more

precise, consider the Fokker-Planck equation of the form [99]:

$$\partial_t \mathcal{W} = -\sum_j \frac{\partial}{\partial z_j} A_j(\mathbf{z}, t) \mathcal{W}$$

$$+ \frac{1}{2} \sum_{j,k} \frac{\partial}{\partial z_j} \frac{\partial}{\partial z_k} \left[\mathbf{B}(\mathbf{z}, t)\mathbf{B}^T(\mathbf{z}, t)\right]_{jk} \mathcal{W}, \tag{B.8}$$

where the diffusion matrix $D = \mathbf{B}\mathbf{B}^T$ is positive definite. Now, we can write equation (B.8) as a system of stochastic equations:

$$\frac{d\mathbf{z}}{dt} = A(\mathbf{z}, t) + \mathbf{B}(\mathbf{z}, t)\mathbf{E}(t), \tag{B.9}$$

where the real noise sources $E_j(t)$ have zero mean and satisfy $\langle E_j(t)E_k(t')\rangle = \delta_{jk}\delta(t - t')$. In our case, equation (B.7) can be rewritten:

$$\frac{dx_j}{dt} = -J(y_{j+1} + y_{j-1}) - U(y_j - x_j^2 y_j - y_j^3)$$

$$- \frac{\gamma_j}{2}x_j + \frac{\sqrt{\gamma_j}}{2}\xi_j(t), \tag{B.10}$$

$$\frac{dy_j}{dt} = J(x_{j+1} + x_{j-1}) + U(x_j - x_j y_j^2 - x_j^3)$$

$$- \frac{\gamma_j}{2}y_j + \frac{\sqrt{\gamma_j}}{2}\eta_j(t), \tag{B.11}$$

where $\xi_j(t), \eta_j(t)$ for $j = 1, ..., M$ are δ-correlated in time with zero mean. Here it must be noted that $\xi_j(t), \eta_j(t)$ are not real noise sources, but are included only to recapture the commutation relations of the operators.

As initial state one uses a product state of the form

$$|\Psi(t = 0)\rangle = |\psi_1\rangle|\psi_2\rangle...|\psi_M\rangle, \tag{B.12}$$

where $|\psi_j\rangle$ is a Glauber coherent state in the jth well. This state represents a pure BEC in a grand-canonical framework. The Wigner function of a Glauber coherent state $|\psi_j\rangle$ is a Gaussian,

$$\mathcal{W}(\alpha_j, \alpha_j^*) = \frac{2}{\pi}\exp\{-|\alpha_j - \psi_j|^2\}. \tag{B.13}$$

Thus we can take the initial values for $\alpha_j = x_j + iy_j$ to be Gaussian random numbers with mean ψ_j.

For a BEC in a Bloch state with quasi momentum k, we have

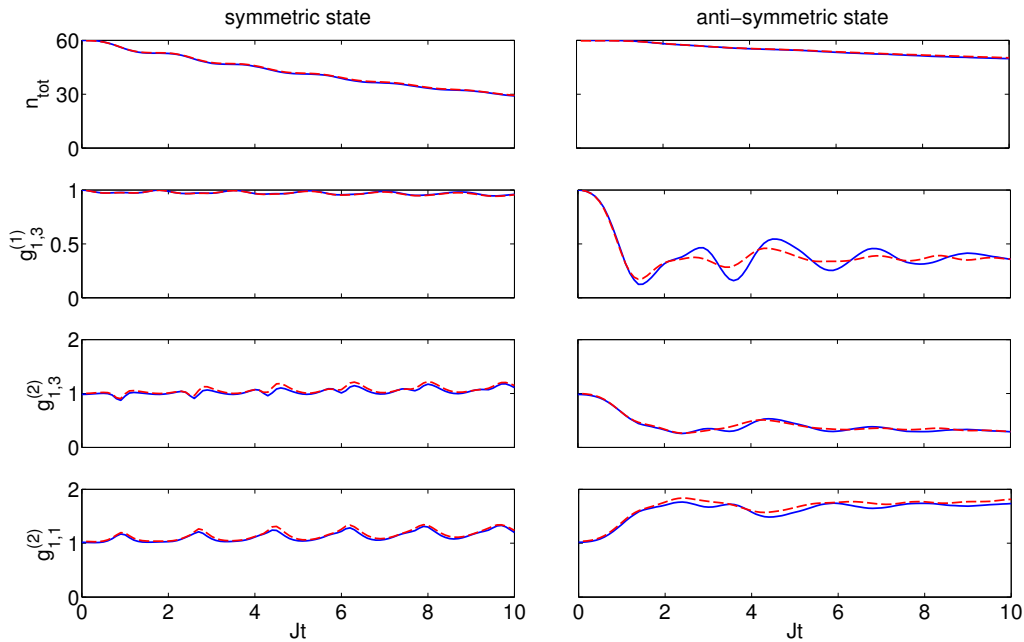$$\psi_j = e^{ikj}\sqrt{\frac{N}{M}}. \tag{B.14}$$

Figure B.1: *A comparison of a truncated Wigner simulation (dashed red lines) and a quantum jump simulation (solid blue lines) shows a very good agreement. Shown is the time evolution of the total atom number $\langle \hat{n}_{\mathrm{tot}} \rangle$, the phase coherence $g_{1,3}^{(1)}$, the density-density correlations $g_{1,3}^{(2)}$ and the density fluctuations $g_{1,1}^{(2)}$. The parameters are: $U = 0.1J$, $\gamma_2 = 0.2J$. The initial states are a pure BEC with a symmetric (left) and antisymmetric (right) wavefunction with $n_1(0) = n_3(0) = 30$ and $n_2(0) = 0$.*

In the text we consider a pure BEC accelerated to the edge of the Brillouin zone such that $k = \pi$.

The truncated Wigner method is used to calculate the evolution of expectation of symmetrized observables as follows. The Wigner function is treated as a probability distribution in phase space. An ensemble of trajectories is sampled according to the Wigner function of the initial state and the propagated according to Eqs. (B.10) and (B.11). Then one takes the stochastic average over this ensemble:,

$$
\begin{aligned}
\langle O_j ... O_k \rangle_{\mathrm{sym}} &= \int \prod_{i=1}^{M} d^2\alpha_i \, O_j ... O_k \, \mathcal{W}(\alpha_1, \alpha_1^*, ...) \\
&= \frac{1}{N_T} \sum_{\ell=1}^{N_T} O_j ... O_k
\end{aligned}
\tag{B.15}
$$

where O_j stands for α_j or α_j^*, N_T is the number of trajectories and the subscript sym reminds us that only expectations values of symmetrized observables can be calculated.

In figure B.1 we compare the results of the truncated Wigner approximation with the results of the exact quantum jump method for a triple-well trap. The simulations show a very good agreement also in the regime of strong interactions. The only small discrepancy is that oscillations of the correlation functions are slightly less pronounced. As the truncated phase space approximations become more accurate with increasing filling factors [97, 98].

Appendix C

Entanglement Criterion

In this appendix we provide a detailed derivation of the entanglement criterion based on (4.9) which is adapted to the NOON states discussed in the present paper. This result generalizes established entanglement criteria in terms of spin squeezing [45] and is derived in a similar way. In contrast to spin squeezing inequalities, it shows that a state is entangled if the variance defined below in (C.2) is *larger* than a certain threshold value.

We assume that the many-body quantum state $\hat{\rho}$ is decomposed into a mixture of pure states

$$
\begin{aligned}
\hat{\rho} &= \sum_a p_a \hat{\rho}_a \\
&= \sum_a p_a |\psi_a\rangle\langle\psi_a|,
\end{aligned} \tag{C.1}
$$

where every pure state $\hat{\rho}_a = |\psi_a\rangle\langle\psi_a|$ has a fixed particle number N_a. Note that the quantum jump simulation of the dynamics directly provides such a decomposition. We define the entanglement parameter

$$
\begin{aligned}
E_{r,q} \;\; := \;\; & \langle(\hat{n}_r - \hat{n}_q)^2\rangle - \langle\hat{n}_r - \hat{n}_q\rangle^2 - \langle\hat{n}_r + \hat{n}_q\rangle \\
& -\frac{1}{2}\sum_{a,b} p_a p_b \left[\langle(\hat{n}_r - \hat{n}_q)\rangle_a - \langle(\hat{n}_r - \hat{n}_q)\rangle_b\right]^2
\end{aligned} \tag{C.2}
$$

for the sites r and q. In this expression $\langle\cdot\rangle_{a,b}$ denotes the expectation value in the pure state $|\psi_{a,b}\rangle$. Now we can proof that $E_{r,q} < 0$ for every separable state such that a value $E_{r,q} > 0$ unambiguously reveals the presence of many-particle entanglement. Note that $E_{r,q}$ provides and entanglement criterion, it is not a quantitative entanglement measure in the strict sense.

To proof this statement we consider an arbitrary separable state and show that $E_{r,q} < 0$ for this class of states. If a pure state $\hat{\rho}_a$ is separable, it can be

written as a tensor product of single particle states

$$\hat{\rho}_a = \hat{\rho}_a^{(1)} \otimes \hat{\rho}_a^{(2)} \otimes \cdots \otimes \hat{\rho}_a^{(N_a)}, \tag{C.3}$$

We furthermore introduce the abbreviation

$$\hat{S}_\pm := \hat{n}_r \pm \hat{n}_q. \tag{C.4}$$

This operator is also written as a symmetrized tensor product of single-particle operators

$$\hat{S}_\pm = \sum_{k=1}^{N_a} \mathbb{1} \otimes \cdots \otimes \mathbb{1} \otimes \hat{s}_\pm^{(k)} \otimes \mathbb{1} \otimes \cdots \otimes \mathbb{1} , \tag{C.5}$$

where the superscript (k) denotes that the single-particle operator $\hat{s}_\pm^{(k)}$ acts on the kth atom. The single-particle operators are given by

$$\hat{s}_\pm = |r\rangle\langle r| \pm |q\rangle\langle q|, \tag{C.6}$$

where $|r\rangle$ is the quantum state where the particle is localized in site r.

For a separable pure state $\hat{\rho}_a$, the expectation values of the population imbalance $\langle \hat{S}_- \rangle_a = \mathrm{Tr}\{\hat{\rho}_a \hat{S}_-\}$ and its square can be expressed as (dropping the subscript a for notational clarity)

$$
\begin{aligned}
\langle \hat{S}_- \rangle &= \sum_{k=1}^{N} \mathrm{Tr}\left[\rho^{(k)} \hat{s}_-^{(k)} \right] \\
\langle \hat{S}_-^2 \rangle &= \sum_{j\neq k}^{N} \mathrm{Tr}\left[(\rho^{(j)} \otimes \rho^{(k)})(\hat{s}_-^{(j)} \otimes \hat{s}_-^{(k)}) \right] \\
&\quad + \sum_{j=1}^{N} \mathrm{Tr}\left[\rho^{(j)} \hat{s}_-^{(j)2} \right] \\
&= \sum_{j,k=1}^{N} \mathrm{Tr}\left[\rho^{(j)} \hat{s}_-^{(j)} \right] \mathrm{Tr}\left[\rho^{(k)} \hat{s}_-^{(k)} \right] \\
&\quad - \sum_{j=1}^{N} \mathrm{Tr}\left[\rho^{(j)} \hat{s}_-^{(j)} \right] \mathrm{Tr}\left[\rho^{(j)} \hat{s}_-^{(j)} \right] + \sum_{j=1}^{N} \mathrm{Tr}\left[\rho^{(j)} \hat{s}_-^{(j)2} \right] \\
&= \langle \hat{S}_- \rangle^2 + \sum_{j=1}^{N} \mathrm{Tr}\left[\rho^{(j)} \hat{s}_-^{(j)2} \right] - \left\{ \mathrm{Tr}\left[\rho^{(j)} \hat{s}_-^{(j)} \right] \right\}^2 .
\end{aligned}
$$

Using $\text{Tr}[\rho^{(j)}\hat{s}_-^{(j)2}] = \text{Tr}[\rho^{(j)}\hat{s}_+^{(j)}]$ we thus find that every pure products state $\hat{\rho}_a$ satisfies the condition

$$\langle \hat{S}_-^2 \rangle_a - \langle \hat{S}_- \rangle_a^2 \leq \langle \hat{S}_+ \rangle_a \, . \tag{C.7}$$

If the total quantum state $\hat{\rho}$ is separable, such that it can be written as a mixture of separable pure states (C.1), the expectation values are given by

$$\langle \hat{S}_-^2 \rangle = \sum_a p_a \langle \hat{S}_-^2 \rangle_a \tag{C.8}$$

$$\leq \langle \hat{S}_+ \rangle + \sum_a p_a \langle \hat{S}_- \rangle_a^2$$

$$\langle \hat{S}_- \rangle^2 = \sum_{a,b} p_a p_b \langle \hat{S}_- \rangle_a \langle \hat{S}_- \rangle_b \tag{C.9}$$

$$= \sum_a p_a \langle \hat{S}_- \rangle_a^2 - \frac{1}{2} \sum_{a,b} p_a p_b \left[\langle \hat{S}_- \rangle_a - \langle \hat{S}_- \rangle_b \right]^2 \, .$$

We thus find that every separable quantum state satisfies the following inequality for the variance of the population imbalance $\hat{S}_-$:

$$\langle \hat{S}_-^2 \rangle - \langle \hat{S}_- \rangle^2 \leq \langle \hat{S}_+ \rangle + \frac{1}{2} \sum_{a,b} p_a p_b \left[\langle \hat{S}_- \rangle_a - \langle \hat{S}_- \rangle_b \right]^2 \, . \tag{C.10}$$

This inequality for separable quantum states can be rewritten as

$$E_{r,q} < 0 \tag{C.11}$$

in terms of the entanglement parameter (C.2).

Appendix D

Calculations for Section 6.1

In this Appendix we shall prove those of the formulas appearing in subsection 6.1.4 for which summations over m or ν must be performed. To begin with, let us discuss (6.53). The relevant integral diverges and calls for the introduction of a cutoff:

$$
\frac{1}{2it} \sum_m \int_0^\infty d\rho \rho \mathrm{e}^{-\frac{\rho^2}{2it}} i^{-\frac{|m|}{n}} J_{\frac{|m|}{n}}\left(\frac{\rho^2}{2t}\right)
$$

$$
\underset{it \to T}{\longrightarrow} \frac{1}{2T} \sum_m \int_0^R d\rho \rho \mathrm{e}^{-\frac{\rho^2}{2T}} I_{\frac{|m|}{n}}\left(\frac{\rho^2}{2T}\right). \tag{D.1}
$$

To handle the last integral we make an intermediate step by introducing the following expression:

$$
\begin{aligned}
F_n(\alpha) &= \frac{1}{2} \sum_{m=-\infty}^\infty \int_0^\infty dq \mathrm{e}^{-\alpha q} I_{\frac{|m|}{n}}(q) \\
&= \frac{1}{2\sqrt{\alpha^2 - 1}} \coth\left(\frac{\alpha + \sqrt{\alpha^2 - 1}}{2}\right) \tag{D.2}
\end{aligned}
$$

which is also a regularized version (for $\alpha \to 1^+$) of the integral entering (6.53). Taking the limit $\alpha = 1 + \epsilon$, $\epsilon \to 0^+$ one easily finds that:

$$
F_n(\alpha) = \frac{n}{2\epsilon} + \frac{1}{12}\left(\frac{1}{n} - n\right) + \mathcal{O}(\epsilon). \tag{D.3}
$$

We immediately see that the diverged part of the integral appears for $n = 1$. In this case the integration in (D.1) is trivial and we are led to the conclusion:

$$
\frac{1}{\epsilon} \to \frac{\pi R^2}{4\pi T} = \frac{V_2}{4\pi T}. \tag{D.4}
$$

Combining this identification with the finite part appearing in (D.3) we get the confirmation of (6.53).

Our next concern is (6.55). Using the identities:

$$\mathrm{e}^{-\frac{(\nu\beta)^2}{4T}} = (4\pi T)^{\frac{D+1}{2}} \int \frac{d^{D+1}p}{(2\pi)^{D+1}} \mathrm{e}^{-Tp^2+ip_0\nu\beta},$$

$$\sum_{\nu=-\infty}^{\infty} \mathrm{e}^{ip_0\nu\beta} = \frac{2\pi}{\beta} \sum_{k=-\infty}^{\infty} \delta(p_0 - \omega_k), \ \omega_k = \frac{2\pi k}{\beta} \tag{D.5}$$

we recast the integral appearing in (6.55) into the form:

$$\frac{1}{2} \frac{V_{D-1}V_2}{(4\pi)^{\frac{D+1}{2}}} \int_{0^+}^{\infty} \frac{dT}{T^{\frac{D+3}{2}}} \mathrm{e}^{-Tm^2} \sum_{\nu} \mathrm{e}^{-\frac{(\nu\beta)^2}{4T}}$$

$$= \frac{V_D}{4} \int \frac{d^D p}{(2\pi)^D} \sum_k \int_{0^+}^{\infty} \frac{dT}{T} \mathrm{e}^{-T\left[(\beta\omega)^2+(2\pi k)^2\right]}. \tag{D.6}$$

To obtain the last result we wrote $V_2 = \int_0^\beta d\tau \int_{-\infty}^{\infty} dx_1 \to \beta L$, we rescaled $T \to T\beta^2$ and we used the abbreviation $\omega^2 = p^2 + m^2$.

Performing the integral over T and neglecting an irrelevant (infinite) constant we get:

$$\int_{0^+}^{\infty} \frac{dT}{T} \mathrm{e}^{-T\left[(\beta\omega)^2+(2\pi k)^2\right]} = -\ln\left((\beta\omega)^2 + (2\pi k)^2\right). \tag{D.7}$$

The summation over k is standard [137]:

$$\frac{1}{2} \sum_k \ln\left((\beta\omega)^2 + (2\pi k)^2\right) = \frac{1}{2}\beta\omega + \ln(1 - \mathrm{e}^{-\beta\omega}). \tag{D.8}$$

The last result proves (6.55).

Following the same line of reasoning we can prove (6.57). Using, once again, the identities (D.5) we rewrite the relevant integral in the form:

$$\frac{1}{12} \frac{V_{D-1}}{(4\pi)^{\frac{D-1}{2}}} \int_0^{\infty} \frac{dT}{T^{\frac{D+1}{2}}} \mathrm{e}^{-Tm^2} \sum_{\nu} \mathrm{e}^{-\frac{(\nu\beta)^2}{4T}}$$

$$= \frac{\pi}{3\beta} V_{D-1} \int \frac{d^D p}{(2\pi)^D} \sum_k \frac{1}{\omega^2 + \omega_k^2}. \tag{D.9}$$

The summation is easily performed:

$$\sum_k \frac{1}{\omega^2 + \omega_k^2} = \frac{\beta}{2\omega} \frac{1}{\tanh(\beta\omega)}. \tag{D.10}$$

Combining (D.9) and (D.10) we immediately obtain (6.57) of the text.

Our next concern is Eq. (6.54). The relevant integral diverges and the introduction of a cutoff is necessary. To this end let us discuss the integral:

$$\sum_m \int_0^\infty d\rho \rho e^{-\frac{\rho^2}{R^2}} J_{\frac{|m|}{n}}^2 \left(\frac{\nu\beta_n}{2t}\rho\right)$$

$$= \frac{R^2}{2} e^{-\frac{(\nu\beta R)^2}{8t^2}} \sum_m I_{\frac{|m|}{n}} \left(\frac{(\nu\beta R)^2}{8t^2}\right) = \frac{R^2}{2} \tag{D.11}$$

which can be considered (at the limit $R \to \infty$) as a regularized version of the integral appearing in (6.54). Note that the divergence in (D.11) is independent of n and, contrary to (D.3), there is no finite part for $n \neq 1$. This completes the proof of (6.54).

To prove (17) it is enough to follow the road we followed to arrive at (D.8). Beginning from the relation:

$$\frac{1}{2} \frac{V_{D-1}V_2}{(4\pi)^{\frac{D+1}{2}}} \int_{0^+}^\infty \frac{dT}{T^{\frac{D+3}{2}}} e^{-Tm^2} \sum_\nu e^{-\frac{(\nu\beta_n)^2}{4T}}$$

$$= \frac{V_D}{4n} \int \frac{d^D p}{(2\pi)^D} \sum_k \int_{0^+}^\infty \frac{dT}{T} e^{-T[(\beta_n\omega)^2 + (2\pi k)^2]} \tag{D.12}$$

we only have to perform a differentiation with respect to n to arrive at the result indicated in (6.56):

$$\partial_n \left\{ \frac{1}{n} \int \frac{d^D p}{(2\pi)^D} \left[-\frac{1}{2}\beta\omega n - \ln\left(1 - e^{-\beta\omega n}\right) \right] \right\}\bigg|_{n=1}$$

$$= \int \frac{d^D p}{(2\pi)^D} \left[\ln\left(1 - e^{-\beta\omega}\right) - \frac{\beta\omega}{e^{\beta\omega} - 1} \right]. \tag{D.13}$$

The last relation we have to prove is (6.68) of the text. We begin by using the Poisson summation formula to find that:

$$\sum_\nu e^{-\frac{(\nu\beta)^2}{4T} - \mu\nu\beta} = \sum_k \int_{-\infty}^\infty dx e^{2\pi ikx} e^{-\frac{(x\beta)^2}{4T} - \mu x\beta}$$

$$= \frac{\sqrt{4\pi T}}{\beta} \sum_k e^{-T(\omega_k + i\mu)^2}. \tag{D.14}$$

With the help of this result we get the mutual information:

$$I_m = \frac{2\pi}{3\beta} V_{D-1} \int \frac{d^D p}{(2\pi)^D} \sum_k \frac{1}{(\omega_k + i\mu)^2 + \omega^2}. \tag{D.15}$$

The sum in the last expression can be easily performed if we rewrite it in the form:

$$\sum_k \frac{1}{(\omega_k + i\mu)^2 + \omega^2} = \frac{1}{2}\frac{\omega - \mu}{\omega} \sum_k \frac{1}{\omega_k^2 + (\omega - \mu)^2} +$$
$$+ \frac{1}{2}\frac{\omega + \mu}{\omega} \sum_k \frac{1}{\omega_k^2 + (\omega + \mu)^2}. \tag{D.16}$$

Using for each term the formula (D.10) we get the result indicated in (6.68).

It would be useful to compare our result indicated in (6.58) with the corresponding result derived in the framework of a two dimensional conformal scalar field theory [116] with central charge $c = 1/2$. This can be done by identifying the ultraviolet cutoff Λ with the inverse lattice spacing $1/\alpha$ and the mass m with the inverse finite size of excluded interval $1/l$ (that is, the infrared cutoff). Given that our result is valid at the limit $L^2 m^2 \to \infty$, the comparison is meaningful only for $\beta/\alpha \to \infty$ or $l/\beta \to \infty$. Applying (6.58) for $D = 1$ we get the result:

$$S_g = \begin{cases} \frac{1}{6}\ln\left(\frac{\Lambda}{m}\right) \to \frac{1}{6}\ln\left(\frac{l}{\alpha}\right) & \text{if } \beta \to \infty \\ \frac{\pi}{6}\frac{1}{m\beta} \to \frac{\pi}{6}\frac{l}{\beta} & \text{if } \beta \to 0 \end{cases}. \tag{D.17}$$

Appendix E

Publications

Publications of the author related to the topics covered in this thesis:

- *Coherent state path integrals in the continuum.*
  G. Kordas, S. Mistakidis and A. I. Karanikas
  Europhysics Letters submitted (2013).

- *Bosonic Transport Through a Chain of Quantum Dots.*
  A. Ivanov, G. Kordas, A. Komnik and S. Wimberger
  European Physical Journal B, **86** (2013) 345. EPJ B Highlight. arXiv:1304.5503

- *Decay and fragmentation in an open Bose-Hubbard chain.*
  G. Kordas, S. Wimberger and D. Witthaut
  Physical Review A, **87** (2013) 043618. arXiv:1307.1538

- *Non-hermitian approach to decaying ultracold bosonic systems.*
  S. Wimberger, C. A. Parra-Murillo and G. Kordas
  Journal of Physics: Conference Series, **442** (2013) 012029.

- *Mutual information and Bose-Einstein condensation.*
  C. N. Gagatsos, A. I. Karanikas and G. Kordas
  Open Systems and Information Dynamics, **20** (2013) 1350008. arXiv:1207.0303

- *Dissipation induced macroscopic entanglement in an open optical lattice.*
  G. Kordas, S. Wimberger and D. Witthaut
  Europhysics Letters, **100** (2012) 30007. arXiv:1307.0828

- *Decay of a Bose-Einstein condensate in a dissipative lattice - the mean-field approximation and beyond.*
  F. Trimborn, D. Witthaut, H. Hennig, G. Kordas, T. Geisel

and S. Wimberger
European Physical Journal D, **63** (2011) 63.

- *Beyond mean-field dynamics in open Bose-Hubbard chains.*
  D. Witthaut, F. Trimborn, H. Hennig, G. Kordas, T. Geisel
  and S. Wimberger
  Physical Review A, **83** (2011) 063608. arXiv:1203.3657.

Bibliography

[1] S. N. Bose, *Plancks Gesetz und Die Lichtquantenhypothese*, Z. Phys. **26** (1924) 178

[2] A. Einstein, *Quantetheorie Des Einatomigen Idealen Gazes. Zweite Abhandlung*, Sitzungsber. preuss. Akad. Wiss. **1** (1925) 3

[3] O. Penrose and L. Onsager, *Bose-Einstein condensation and liquid Helium*, Phys. Rev. **104** (1956) 576

[4] A. J. Legget, *Bose-Einstein condensation in the alkali gases: Some fundamental concepts*, Rev. Mod. Phys. **73** (2001) 307

[5] I. Bloch, J. Dalibard and W. Zwerger, *Many-body physics with ultracold gases*, Rev. Mod. Phys. **80** (2008) 885

[6] I. S. Gradshteyn and I. M. Ryzhic, *Table of Integrals, Series and Products*, Academic Press, New York, 5. edition, (1994)

[7] W. Ketterle, *Nobel Lecture: When atoms behave as waves: Bose-Einstein condensation and atom laser*, Rev. Mod. Phys. **74** (2002) 1131

[8] M. H. Anderson, J. R. Ensher, M. R. Matthews, C. E. Wieman and W. E. Cornell, *Observation of Bose-Einstein condensation in a dilute atomic vapor*, Science **269** (1995) 198

[9] K. B. Davis, M.-O. Mewes, M. R. Andrews, N. J. van Druten, D. S. Durfee, D. M. Kurn, and W. Ketterle, *Bose-Einstein Condensation in a Gas of Sodium Atoms*, Phys. Rev. Lett. **75** (1995) 3969

[10] E. A. Cornell, *Very Cold Indeed: The Nanokelvin Physics of Bose-Einstein Condensation*, J. Res. Nat. Inst. Stand. Technol. **101** (1996) 419

[11] W. H. Wing, *On neutral particle trapping in quasistatic electromagnetic fields*, Prog. Quant. Elec. **8** (1984) 181

[12] Y. Castin, *Bose-Einstein condensates in atomic gases*, in R. Kaiser, editor, *Les Houches Session LXXII, Coherent Atomic Matter Waves.* Springer, (2000)

[13] P. Meystre, *Atom optics*, Springer (2001)

[14] D. Jaksch, C. Bruder, J. I. Cirac, C. W. Gardiner and P. Zoller, *Cold Bosonic Atoms in Optical Lattices*, Phys. Rev. Lett. **81** (1998) 3108

[15] M. P. A. Fisher, P. B. Weichman, G. Grinstein and D. S. Fisher, *Boson localization and the superfluid-insulator transition*, Phys. Rev. B **40** (1989) 546

[16] M. Greiner, O. Mandel, T. Esslinger, T. W. Hänsch and I. Bloch, *Quantum phase transition from a superfluid to a Mott insulator in a gas of ultracold atoms* , Nature **415** (2002) 39

[17] L. Pitaevskii and S. Stringari, *Bose-Einstein Condensation*, Oxford University Press (2003)

[18] C. Patric and H. Smith, *Bose-Einstein Condensation in Dilute Gases*, 2nd ed. Cambridge University Press (2008)

[19] A. Griffin, I. Nikumi and E. Zaremba, *Bose-Condensed Gases at Finite Temperature*, Cambridge University Press (2009)

[20] M. Naraschewski and R. J. Glauber, *Spatial coherence and density correlations of trapped Bose gases*, Phys. Rev. A **59** (1999) 4595

[21] I. Abramowitz and I. A. Stegun, *Handbook of Mathematical Functions*, National Bureau of Standards (1964)

[22] H. Breuer and F. Petruccione, *The Theory of Open Quantum Systems*, Oxford University Press (2002)

[23] S. Kryszewski and J. Czechowska-Kryszk, *Master Equation - Tutorial Approach*, arXiv:0801.1757

[24] C. Gross, T. Zibold, E. Nicklas, J. Estève and M. K. Oberthaler, *Nonlinear atom interferometer surpasses classical precision limit*, Nature **464** (2010) 1165

[25] M. Albiez, R. Gati, J. Fölling, S. Hunsmann, M. Cristiani and M. K. Oberthaler, *Direct observation of tunneling and nonlinear self-trapping in single bosonic Josephson junction*, Phys. Rev. Lett. **95** (2005) 010402

[26] T. Gericke, P. Würtz, D. Reitz, C. Utfeld and H. Ott, *All-optical forma-tion of a Bose–Einstein condensate for applications in scanning elec-tron microscopy*, Appl. Phys. B **89** (2007) 447

[27] T. Gericke, P. Würtz, D. Reitz, T. Langen and H. Ott, *High-resolution scanning electron microscopy of an ultracold quantum gas*, Nature Phys. **4** (2008) 949

[28] T. Gericke, *A scanning electron microscope for ultracold quantum gases*, Doktorarbeit, Johannes Gutenberg-Universität Mainz (2010)

[29] V. Guarrera, P. Würtz, A. Ewerbeck, A. Vogler, G. Barontini and H. Ott, *Observation of Local Temporal Correlations in Trapped Quantum Gase*, Phys. Rev. Lett. **107** (2011) 160403

[30] C. Weitenberg, M. Endres, J. F. Sherson, M. Cheneau, P. Schauß, T. Fukuhara, I. Bloch and S. Kuhr, *Single-spin addressing in an atomic Mott insulator*, Nature **471** (2011) 319

[31] W. S. Bakr, J. I. Gillen, A. Peng, Foelling and M. Greiner, *A quantum gas microscope for detecting single atoms in a Hubbard-regime optical lattice*, Nature **462** (2009) 74

[32] J. F. Sherson, C. Weitenberg, M. Endres, M. Cheneau, I. Bloch and S. Kuhr, *Single-atom-resolved fluorescence imaging of an atomic Mott insulator* Nature **467** (2010) 68

[33] I. Afek, O. Ambar and Y. Silberberg, *High-NOON states by mixing quantum and classical light* , Science **328** (2010) 879

[34] C. Sias, A. Zenesini, H. Lignier, S. Wimberger, D. Ciampini, O. orsch and E. Arimondo, *Resonantly enhanced tunneling of Bose-Einstein con-densates in periodic potentials*, Phys. Rev. Lett. **98** (2007) 120403

[35] E. Peik, M. B. Dahan, I. Bouchoule, Castin and C. Salomon, *Bloch oscillations of atoms, adiabatic rapid passage, and monokinetic atomic beams* Phys. Rev. A **55** (1997) 2989

[36] G. Barontini, R. Labouvie, F. Stubenrauch, A. Vogler, V. Guarrera and H. Ott, *Controlling the dynamics of an open many-body quantum system with localized dissipation*, Phys. Rev. Lett. **110** (2013) 035302

[37] G. J. Milburn, J. Corney, E. M. Wright and D. F. Walls, *Quantum dynamics of an atomic Bose-Einstein condensate in a double-well po-tential*, Phys. Rev. A **55** (1997) 4318

[38] A. Smerzi, S. Fantoni, S. Giovanazzi and S. R. Shenoy, *Quantum coherent atomic tunneling between two trapped Bose-Einstein condensates*, Phys. Rev. Lett. **79** (1997) 4950

[39] I. Tikhonenkov, J. R. Anglin and A. Vardi, *Quantum dynamics of Bose-Hubbard Hamiltonians beyond the Hartree-Fock-Bogoliubov approximation: The Bogoliubov back-reaction approximation*, Phys. Rev. A **75** (2007) 013613

[40] A. Vardi, J. R. Anglin, *Bose-Einstein condensates beyond mean field theory: Quantum backreaction as decoherence*, Phys. Rev. Let. **86** (2001) 568

[41] J. R. Anglin and A. Vardi, *Dynamics of a two-mode Bose-Einstein condensate beyond mean-field theory*, Phys. Rev. A **64** (2001) 013605

[42] D. Leibfried, E. Knill, S. Seidelin, J.Britton, R. B. Blakestad, J. Chiaverini, D. B. Hume, W. M. Itano, J. D.Jost, C. Langer, R. Ozeri, R. Reichle and D. J. Wineland, *Creation of a six-atom "Schrödinger cat" state*, Nature **438** (2005) 639.

[43] V. Giovannetti, S. Lloyd and L. Maccone, *Quantum-Enhanced Measurements: Beating the Standard Quantum Limit*, Science **306** (2004) 1330

[44] J. J. Bollinger, W. M. Itano, D. J. Wineland and D. J. Heinzen, *Optimal frequency measurements with maximally correlated states*, Phys. Rev. A **54** (1996) R4649

[45] A. S Sørensen, L.-M. Duan, J. I. Cirac and P. Zoller, *Many-particle entanglement with Bose–Einstein condensates*, Nature **409** (2001) 63

[46] D. K. Campbell, S. Flach, and Y. S.Kivshar, *Localizing energy through nonlinearity and discreteness*, Phys. Today **467** (2004) 57

[47] S. Flach and A. V. Gorbach, *Discrete breathers — Advances in theory and applications*, Phys. Rep. **467** (2008) 1

[48] H. Henning, J. Dorignac and D. K. Campbell, *Transfer of Bose-Einstein condensates through discrete breathers in an optical lattice*, Phys. Rev. A **82** (2010) 053604

[49] J. Anglin, *Cold, dilute, trapped bosons as an open quantum system*, Phys. Rev. Lett. **79** (1996) 6

[50] M. Trujillo-Martinez, A Posazhennikova and J. Kroha, *Nonequilibrium Josephson oscillations in Bose-Einstein condensates without dissipation*, Phys. Rev. Lett. **103** (2009) 105302

[51] D. Poletti, J.-S. Bernier, A. Georges and C. Kollath, *Interaction-Induced Impeding of Decoherence and Anomalous Diffusion*, Phys. Rev. Lett. **109** (2012) 045302

[52] H. Pichler, A. J. Daley and P. Zoller, *Nonequilibrium dynamics of bosonic atoms in optical lattices: Decoherence of many-body states due to spontaneous emission*, Phys. Rev. A **82** (2010) 063605

[53] Yun Li, Y. Castin and A. Sinatra, *Optimum spin squeezing in Bose-Einstein condensates with particle losses*, Phys. Rev. Lett. **100** (2008) 210401

[54] V. A. Brazhnyi, V. V. Konotop, V. M. Pérez-García and H. Ott, *Dissipation-induced coherent structures in Bose-Einstein condensates*, **102** (2009) 144101

[55] R. Livi, R. Franzosi and G.-L. Oppo, *Self-localization of Bose-Einstein condensates in optical lattices via boundary dissipation*, Phys. Rev. Lett. **97** (2006) 060401

[56] G. S. Ng, H. Hennig, R. Fleischmann, T. Kottos and T. Geisel, *Avalanches of Bose-Einstein condensates in leaking optical lattices*, New J. Phys. **11** (2009) 073045

[57] F. Trimborn, D. Witthaut and S. Wimberger, *Mean-field dynamics of a two-mode Bose–Einstein condensate subject to noise and dissipation*, J. Phys. B: At. Mol. Opt. Phys. **41** (2008) 171001

[58] D. Witthaut, F. Trimborn and S. Wimberger, *Dissipation induced coherence of a two-mode Bose-Einstein condensate*, Phys. Rev. Lett. **101** (2008) 200402

[59] D. Witthaut, F. Trimborn and S. Wimberger, *Dissipation-induced coherence and stochastic resonance of an open two-mode Bose-Einstein condensate*, Phys. Rev. A **79** (2009) 033621

[60] J. J. García-Ripoll, S. Dürr, N. Syassen, D. M. Bauer, M. Lettner, G. Rempe and J. I. Cirac, *Dissipation-induced hard-core boson gas in an optical lattice*, New J. Phys. **11** (2009) 013053

[61] V. S. Shchesnovich and D. S. Mogilevtsev, *Three-site Bose-Hubbard model subject to atom losses: Boson-pair dissipation channel and failure of the mean-field approach*, Phys. Rev. A **82** (2010) 043621

[62] K. V. Kepesidis and M. J. Hartmann, *Bose-Hubbard model with localized particle losses*, Phys. Rev. A **85** (2012) 063620

[63] P. Barmettler and C. Kollath, *Controllable manipulation and detection of local densities and bipartite entanglementin a quantum gas by a dissipative defect*, Phys. Rev. A **84** (2011) 041606R

[64] D. Witthaut, F. Trimborn, H. Hennig, G. Kordas, T. Geisel and S. Wimberger, *Beyond mean-field dynamics in open Bose-Hubbard chains*, Phys. Rev. A **83** (2011) 063608

[65] F. Trimborn, D. Witthaut, H. Hennig, G. Kordas, T. Geisel and S. Wimberger, *Decay of a Bose-Einstein condensate in a dissipative lattice – the mean-field approximation and beyond*, Eur. Phys. J. D **63** (2011) 63

[66] G. Kordas, S. Wimberger and D. Witthaut, *Dissipation-induced macroscopic entanglement in an open optical lattice*, Europhys. Lett. **100** (2012) 30007

[67] G. Kordas, S. Wimberger and D. Witthaut, *Decay and fragmentation in an open Bose-Hubbard chain*, Phys. Rev. A **87** (2013) 043618

[68] S. Wimberger, C. Parra-Murillo and G. Kordas, *Non-hermitian approach to decaying ultracold bosonic systems*, J. Phys.: Conf. Ser. **442** (2013) 012029

[69] C. Kohstall, M. Zaccanti, M. Jag, A. Trenkwalder, P. Massignan, G. M. Bruun, F. Schreck and R. Grimm, *Metastability and coherence of repulsive polarons in a strongly interacting Fermi mixture*, Nature **485**, (2012) 615

[70] H. Hennig and R. Fleischmann, *Nature of self-localization of Bose-Einstein condensates in optical lattices*, Phys. Rev. A **87** (2013) 033605

[71] J. I. Cirac, A. Schenzle, P. Zoller, *Inhibition of quantum tunneling of an atom due to the continuous observation of light scattering*, Europhys. Lett. **27** (1994) 123

[72] D. A. Zezyulin, V. V. Konotop, G. Barontini and H. Ott, *Macroscopic Zeno effect and stationary flows in nonlinear waveguides with localized dissipation*, Phys. Rev. Lett. **109** (2012) 020405

[73] S. Burger, K. Bongs, S. Dettmer, W. Ertmer and K. Sengstock, *Dark solitons in Bose-Einstein condensates*, Phys. Rev. Lett. **83** (1999) 5198

[74] J. Denschlag, J. E. Simsarian, D. L. Feder, C. W. Clark, L. A. Collins, J. Cubizolles, L. Deng, E. W. Hagley, K. Helmerson, W. P. Reinhardt, S. L. Rolston, B. I. Schneider, W. D. Phillips, *Generating Solitons by Phase Engineering of a Bose-Einstein Condensate*, Science **287** (2000) 97

[75] L. D. Carr, J. Brand, S. Burger and A. Sanpera, *Dark-soliton creation in Bose-Einstein condensates*, Phys. Rev. A **63** (2001) 051601R

[76] B. Wu, J. Liu, and Q. Niu, *Controlled generation of dark solitons with phase imprinting*, Phys. Rev. Lett. **88** (2002) 034101

[77] Y. Zheng and J. Javanainen, *Classical and quantum models for phase imprinting*, Phys. Rev. A **67** (2003) 035602

[78] A. Ivanov, G. Kordas, A. Komnik and S. Wimberger, *Bosonic transport through a chain of quantum dots*, Eur. Phys. J. B**86** (2013) 345

[79] D. P. E. Smith, *Quantum point contact switches*, Science **269** (1995) 371

[80] F.-Q. Xie, L. Nittler, C. Obermair and T. Schimmel, *Gate-Controlled Atomic Quantum Switch*, Phys. Rev. Lett **93** (2004) 128303

[81] K. Terabe, T. Hasegawa, T. Nakayama and M. Aono, *Quantized conductance atomic switch*, Nature **433** (2005) 47

[82] M. Fuechsle, J. A. Miwa, S. Mahapatra, H. Rya, S. Lee, O. Warschkolow, L. C. L. Hollenberg, G. Klimeck and M. Y. Simmons, *A single-atom transistor*, Nat. Nanotechnol. **7** (2012) 242

[83] D. B. Gutman, Y. Gefen and A. D. Mirlin, *Cold bosons in the Landauer setup*, Phys. Rev. B **85** (2012) 125102

[84] P. Schlagheck, F. Malet, J. C. Cremons, S. M. Reimann, *Transport and interaction blockade of cold bosonic atoms in a triple-well potential*, New J. Phys. *12* (2010) 065020

[85] L. H. Kristindóttir, O. Karlström, J. Bjerlin, J. C. Cremon, P. Schlagheck, A. Wacker, and S. M. Reimann, *Total current blockade in an ultracold dipolar quantum wire*, Phys. Rev. Lett. **110** (2013) 085303

[86] C. Chien, M. Zwolak and M. Ventra, *Bosonic and fermionic transport phenomena of ultracold atoms in one-dimensional optical lattices*, Phys. Rev. A **85** (2012) 041601

[87] M. Bruderer and W. Belzig, *Mesoscopic transport of fermions through an engineered optical lattice connecting two reservoirs*, Phys. Rev. A **85** (2012) 013623

[88] C. Chien, M. Zwolak and M. Ventra, *Controlling transport of ultracold atoms in one-dimensional optical lattices with artificial gauge fields*, Phys. Rev. A **87** (2013) 023609

[89] R. A. Pepino, J. Cooper, D. Meiser, D. Z. Anderson, and M. J. Holland, *Open quantum systems approach to atomtronics*, Phys. Rev. A **82** (2010) 013640

[90] S. C. Caliga, C. J. E. Straatsma, A. A. Zozulya and D. Z. Anderson, *A matterwave transistor oscillator*, arXiv:1208.3109 (2012)

[91] M. Gajdacz, T.Opatrnýand K. K. Das, *An atomtronics transistor for quantum gates*, arXiv:1207.3108, (2012)

[92] J. Brantut, J. Meineke, D. Stadler, S. Krinner and T. Esslinger, *Conduction of ultracold fermions through a mesoscopic channel*, Science **337** (2012) 1069

[93] K. Mølmer, Y. Castin and J. Dalibard, *Monte Carlo wave-function method in quantum optics*, J. Opt. Soc. Am. B **10** (1993) 524

[94] M. J. Werner and P. D. Drummond, *Robust algorithms for solving stochastic partial differential equations*, J. Comput. Phys. **132** (1997) 312

[95] A. Sinatra, C. Lobo and Y. Castin, *The truncated Wigner method for Bose-condensed gases: limits of validity and applications*, J. Phys. B **35** (2002) 3599

[96] C. W. Gardiner and P. Zoller, *Quantum Noise*, Springer Series in Synergetics, Berlin Heidelberg New York (2004)

[97] F. Trimborn, D. Witthaut and H. J. Korsch, *Exact number-conserving phase-space dynamics of the M-site Bose-Hubbard model*, Phys. Rev. A **77** (2008) 043631

[98] F. Trimborn, D. Witthaut and H. J. Korsch, *Beyond mean-field dynamics of small Bose-Hubbard systems based on the number-conserving phase-space approach*, Phys. Rev. A **79** (2009) 013608

[99] C. W. Gardiner, *Stochastic Methods: A Handbook for the Natural and Social Sciences*, Springer Series in Synergetics, Berlin Heidelberg New York (2009)

[100] M. V. Berry, *interview by Nina Hall: 'Caustics, catastrophes and quantum chaos'*, Nexus News (1997) 4

[101] P. Schlagheck and S. Wimberger, *Nonexponential decay of Bose-Einstein condensates: a numerical study based on the complex scaling method*, Appl. Phys. B **86** (2007) 385

[102] A. Regensburger, C. Bersch, B. Hinrichs, G. Onishchukov, A. Schreiber, C. Silberhorn and U. Peschel, *Photon propagation in a discrete fiber network: An interplay of coherence and losses*, Phys. Rev. Lett. **107** (2011) 233902

[103] A. Tomadin, S. Diehl, M. D. Lukin, P. Rabl and P. Zoller, *Reservoir engineering and dynamical phase transitions in optomechanical arrays*, Phys .Rev. A **86** (2012) 033821

[104] M. Schmidt, M. Ludwig and F. Marquardt, *Optomechanical circuits for nanomechanical continuous variable quantum state processing*, New J. Phys. **14** (2012) 125005

[105] C. N. Gagatsos, A. I. Karanikas, G. Kordas, *Mutual Information and Bose-Einstein Condensation*, Open Syst. Inf. Dyn. **20** (2013) 1350008

[106] J. I. Kapusta and C. Gale, *Finite-temperature field theory principles and applications*, Cambridge Monographs on Mathematical Physics (2006)

[107] J. K. Pachos, *Introduction to Topological Quantum Computation*, Cambridge University press (2012)

[108] L. Bombelli, R. K. Koul, J. Lee and R. D. Sorkin, *Quantum source of entropy for black holes*, Phys. Rev. D **34** (1986) 373

[109] M. Srednicki, *Entropy and area*, Phys. Rev. Lett. **71**, 666 (1993)

[110] D. Kabat and M. J. Srassler, *A comment on entropy and area*, Phys. Lett. B **329** (1994) 46

[111] C. Callan and F. Wilzeck, *On geometric entropy*, Phys. Lett. B **333** (1994) 55

[112] C. Holzey, F. Larsen and F. Wilczeck, *Geometric and renormalized entropy in conformal field theory*, Nucl. Phys. B **424** (1994) 443

[113] F. Larsen and F. Wilczeck, *Geometric Entropy, Wave Functionals, and Fermions*, Annals Phys. **243** (1995) 280

[114] D. Kabat, *Black hole entropy and entropy of entanglement*, Nucl. Phys. B **453** (1995) 281

[115] F. Larsen and F. Wilczeck, *Renormalization of black hole entropy and of the gravitational coupling constant*, Nucl. Phys. B **458** (1996) 249

[116] P. Calabrese and J. Cardy, *Entanglement entropy and quantum field theory* , J. Stat. Mech. P06002 (2004)

[117] P. Calabrese and J. Cardy, *Entanglement entropy and quantum field theory: a non-technical introduction* , Int. J. Quant. Inf. **4** (2006) 429

[118] J. Cardy, O. A. Castro-Alvaredo and B. Doyon, *Form factors of branch-point twist fields in quantum integrable models and entanglement entropy*, J. Stat. Phys. **130** (2008) 129

[119] P. Calabrese and J. Cardy, *Entanglement entropy and conformal field theory*, J. Phys. A: Math. Th. **42** (2009) 504005

[120] J. D. Bekenstein, *Black Holes and Entropy*, Phys. Rev. D **7** (1973) 2333

[121] S. W. Hawking, *Black hole explosions?*, Nature **248** (1974) 30

[122] M. B Plenio and V. Vedral, *Teleportation, entanglement and thermo-dynamics in the quantum world*, Contemp. Phys. **39** (1998) 431

[123] K. M. R. Audenaert, J. Eisert, M. B. Plenio and R. F. Werner, *Entanglement properties of the harmonic chain*, Phys. Rev. A **66** (2002) 042327

[124] T. J. Osborne and M. A. Nielsen, *Entanglement in a simple quantum phase transition*, Phys. Rev. A **66** (2002) 032110

[125] A. L. Osterloh, A. L. Amico, G. Falsi and R. Fazio, *Scaling of entanglement close to a quantum phase transition*, Nature **416** (2002) 608

[126] G. Vidal, J. L. Latorre, E. Rico and A. Kitaev, *Entanglement in Quantum Critical Phenomena*, Phys. Rev. Lett. **90** (2003) 227902

[127] M. M. Wolf, F. Verstract, M. B. Hastings and J. I. Cirac, *Area Laws in Quantum Systems: Mutual Information and Correlations*, Phys. Rev. Lett. **100** (2008) 070502

[128] W. K. Wootters, *Entanglement of formation and concurrence*, Quantum Inf. Comput. **1** (2001) 27

[129] L. Heaney, J. Anders, D. Kaszlikowski and V. Vedral, *Spatial entanglement from off-diagonal long-range order in a Bose-Einstein condensate*, Phys. Rev. A **76** (2007) 053605

[130] C. Adami and N. J. Cerf, *von Neumann capacity of noisy quantum channels*, Phys. Rev. A **56** (1997) 3470

[131] L. Henderson and V. Vedral, *Classical, quantum and total correlations*, J. Phys. A: Math. Gen. **34** (2001) 6899

[132] B. Groisman, S. Popescu and A. Winter, *Quantum, classical, and total amount of correlations in a quantum state*, Phys. Rev. A **72** (2005) 032317

[133] W. Ding and K. Yang, *Entanglement entropy and mutual information in Bose-Einstein condensates*, Phys. Rev. A **80** (2009) 012329

[134] M. Fujita, T. Nishioka and T. Takayanagi, *Geometric entropy and hagedorn/deconfinement transition*, JHEP **0809** (2008) 016

[135] M. Fujita and H. Ohki, *Geometric entropy and third order phase transition in d=4 N=2 SYM with flavor*, JHEP **1008** (2010) 056

[136] P. T. Landsberg and J. Dunning-Davies, *Ideal relativistic Bose condensation*, Phys. Rev. **138** (1965) A1049

[137] J. I. Kapusta, *Bose-Einstein condensation, spontaneous symmetry breaking, and gauge theories*, Phys. Rev. D **24** (1981) 426

[138] H. E. Haber and H. Arthur Weldon, *Thermodynamics of an ultrarelativistic ideal Bose gas*, Phys. Rev. Lett. **46** (1981) 1497

[139] H. E. Haber and H. Arthur Weldon, *Finite-temperature symmetry breaking as Bose-Einstein condensation*, Phys. Rev. D **25** (1982) 502

[140] Yu. A. Simonov, Phys. Atom. Nucl. **58** (1995) 309

[141] S. Deser and R. Jackiw, *Classical and quantum scattering on a cone*, Commun. Math. Phys. **118** (1988) 495

[142] R. P. Feynman, *Space-time approach to non-relativistic quantum mechanics*, Rev. Mod. Phys. **20** (1948) 367

[143] R. P. Feynman, *An operator calculus having applications in quantum electrodynamics*, Phys. Rev. **84** (1951) 108

[144] H. Kleinert, *Path integrals in quantum mechanics, statistics, polymer physics and financial markets*, World Scientific Publishing Co. (2006)

[145] J. R. Klauder and B. S. Skagerstam, *Coherent States, Applications in Physics and Mathematical Physics,* World Scientific, Singapore (1985)

[146] J. R. Klauder, *Path integrals and stationary-phase approximations*, Phys. Rev. D **19** (1979) 2349

[147] J. R. Klauder, *"Some recent results on wave equations, path integrals and semiclassical approximations"*, ed. Papanicolaou, *Random Media*, Springer, Berlin (1985)

[148] J. R. Klauder, *"Continuous Representations and Path Integrals, Revisited"*, eds. Papadopoulos G. J. and Devreese J. T., pp. 5-38, Plenum Pub. Corp. (1978)

[149] J. R. Klauder, *"The Feynman Path Integral: A Historical Slice"*, in *A Garden of Quanta*, Eds. Arafune J., et al, World Scientific, Singapore (2003)

[150] Y. Weissman, *Semiclassical approximation in the coherent states representation*, J. Chem. Phys. **76** (1982) 4067

[151] M. Baranger, M. A. M. de Aguiar, F. Keck, H. J. Korsch and B. Schellhaab, *Semiclassical approximations in phase space with coherent states*, J. Phys. A: Math. Gen. **34** (2001) 7227

[152] J. H. Wilson and V. Galitski, *Breakdown of the coherent state path integral: two simple examples*, Phys. Rev. Lett. **106** (2011) 110401

[153] R. Stratonovich, Sov. Phys. Docl. **2** (1958) 416

[154] J. Hubbard, *Calculation of Partition Functions*, Phys. Rev. Lett. **3** (1959) 77

[155] B. Mühlschlegel, *Asymptotic expansion of the Bardeen-Cooper-Schrieffer partition function by means of the functional method*, J. Math. Phys. **3** (1962) 522

[156] M. B. Halpern, *Large N saddle formulation of quadratic building block theories*, Nucl. Phys. B 173 (1980) 504

[157] A. Jevicki and B. Sakita, *Collective field approach to the large-N limit: Euclidean field theories*, Nucl. Phys. B **185** (1981) 89

[158] H. G. Dosch, *Gluon condensate and effective linear potential*, Phys. Lett. B **190** (1987) 177